Molecular Design, Synthesis, and Properties of Highly Efficient Thermally Activated Delayed Fluorescence Materials for Organic Light-Emitting Diodes

李, ジヨン

2017

Doctoral Dissertation

Molecular Design, Synthesis, and Properties of Highly Efficient Thermally Activated Delayed Fluorescence Materials for Organic Light-Emitting Diodes

Jiyoung Lee

Department of Automotive Science

Graduate School of Integrated Frontier Sciences

Kyushu University

Table of Contents

Chapter 4. Isobenzofuranone- and Chromone-Based Thermally Activated Delayed Fluorescence Materials for Reduced Efficiency Roll-Off in Blue Organic Light-Emitting Diodes

Chapter 5. Oxadiazole- and Triazole-Based Thermally Activated Delayed Fluorescence Materials for Efficient Blue and Green Organic Light-Emitting Diodes

Chapter 6. Phenazine-Based Thermally Activated Delayed Fluorescence Materials for Emission Color Tuning in Organic Light-Emitting Diodes

Chapter 1

General Introduction

1. 1 Organic Light-Emitting Diodes (OLEDs)

Organic light-emitting diodes (OLEDs) have been drawing considerable attention for their practical applications in flexible displays and solid-state lighting sources as architectural or automotive lighting because of their unique advantages in flexibility, high contrast, light weight, and improved brightness.[1] In OLEDs, physical processes are charge injection and transport, charge recombination and excitons energy transfer, and light emission (Figure 1-1).[2] In operation of OLEDs, holes are injected from anode, and hole injection and transporting layers (HIL and HTL, respectively) in adjacent to the anode allow for holes transport into the emitting layer (EML). At the opposite side, electrons are injected from cathode into an electron transporting layer (EIL). The injected electrons transport through an electron transporting layer (ETL) into the EML. In the EML, excitons generated by recombination of holes and electrons can be used for light emission.[3] According to spin statics, recombination of holes and electrons produces singlet (antiparallel spins) and triplet (parallel spins) excitons in a 1:3 ratio.[4] Each of these processes plays an important role in electroluminescence (EL) performance such as external EL quantum efficiency (η_{ext}), luminance, and turn-on voltage.

The first observations of EL by applying a high alternating current voltage in organic materials, was reported by Bernanose and co-workers in the 1950s.[5] In 1965, the EL in anthracene crystals was confirmed by the recombination of electrons and holes by an external electric field.[6]
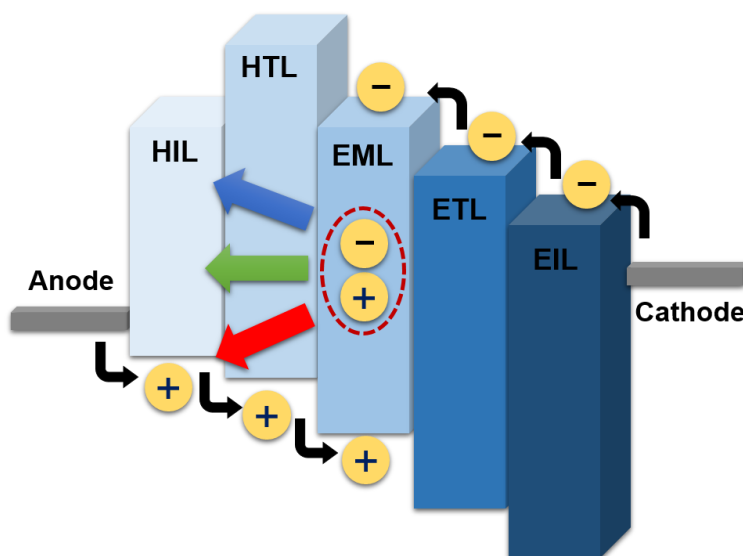
Figure 1-1. Schematic illustration of OLEDs (HIL: hole injection layer, HTL: hole transporting layer, EML: emitting layer, ETL: electron transporting layer, and EIL: electron injection layer).

In 1987, Tang and VanSlyke reported that the first bilayer structured OLEDs containing tris(8-hydroxyquinolinato)aluminum (Alq$_3$) as the ETL (EML), as shown in Figure 1-2. This device exhibited an η_{ext} of nearly 1% and luminance of 1000 cd A^{-1} at a voltage of 10V.[7]
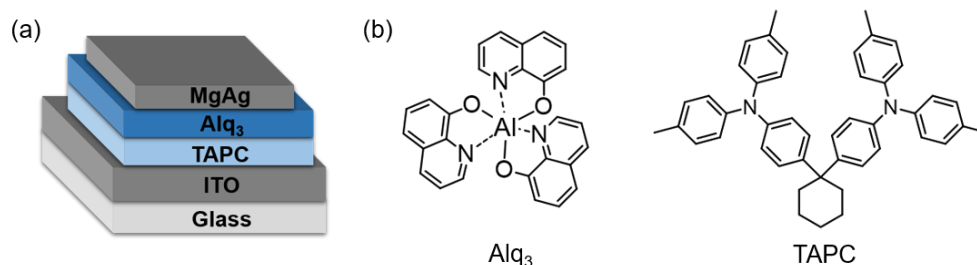
Figure 1-2. (a) Bilayer structured OLED and (b) molecular structures of Alq$_3$ and TAPC.

1. 2 Photophysical Processes of Organic Materials

After an organic molecule is excited by photon absorption, it can return to the ground state (S$_0$) through radiative transitions (fluorescence, phosphorescence, or delayed fluorescence), but it can also undergo intramolecular energy transfer such as long-range dipole–dipole transition or exchange energy transfer (Figure 1-2).[8]
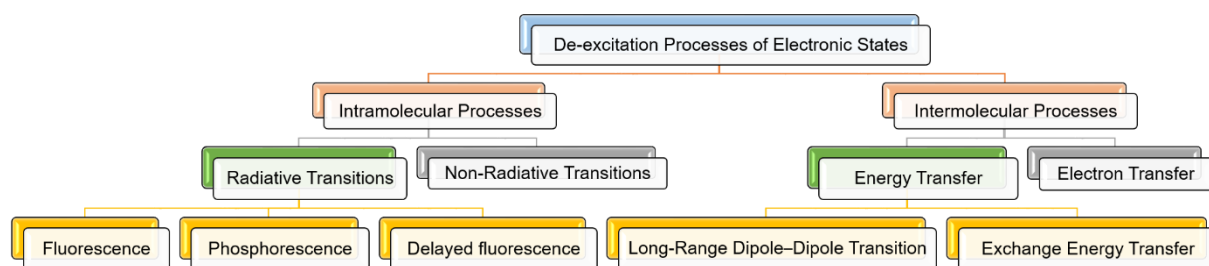
Figure 1-2. Possible de-excitation process of excited molecules.

1. 2. 1 Fluorescence and Phosphorescence

The possible processes such as fluorescence, phosphorescence, delayed fluorescence, and internal conversion of organic molecules can be visualized by the Perrin-Jablonski diagram,[8] as shown in Figure 1-3. The electronic singlet and triplet states are denoted by S$_n$ and T$_n$, respectively. Absorption of a photon with transient time of 10^{-15} s which is faster than the all other processes, can bring a molecule to one of the vibrational levels of the lowest excited singlet state (S$_1$) or higher singlet state (S$_2$, S$_3$. etc). Then excited photon degrades to the lowest

vibrational levels of excitd electronic states having the same electronic energy, beacuse of the vibration energy loss (so-called vibrational relaxation). Consequently, the most organic molecules exhibit broad absorption and emission spectra, which consist of continuous vibrational levels of the ground and excited electronic states.
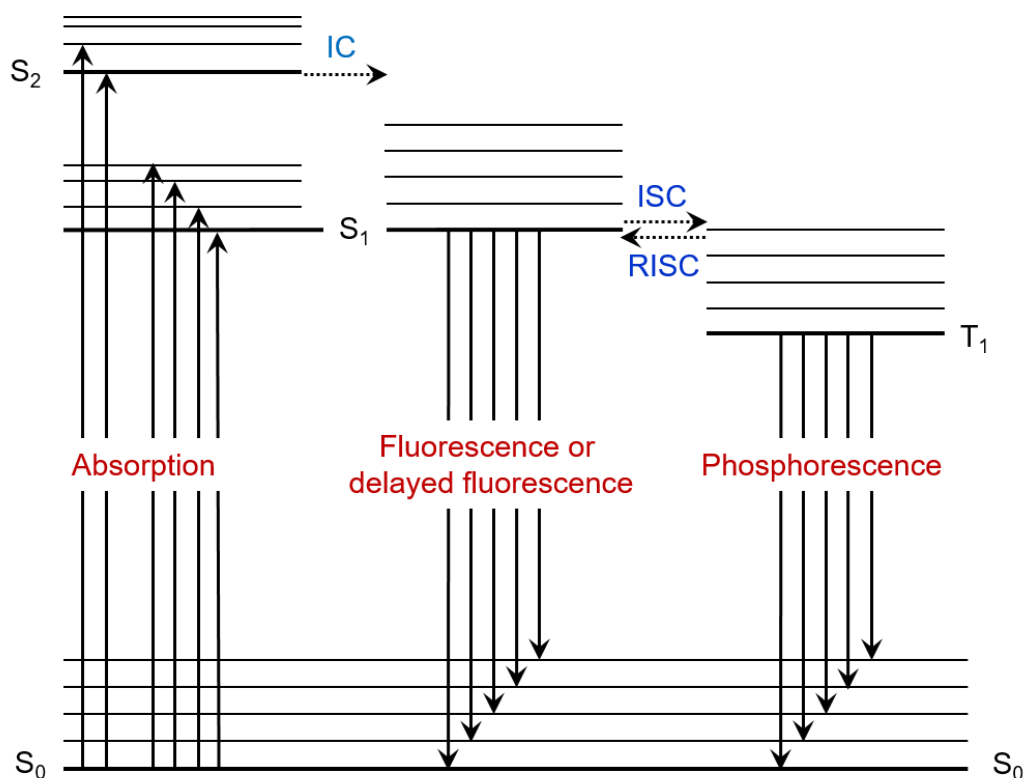
Figure 1-3. Perrin–Jablonski diagram (Radiative processes: fluorescence, phosphorescence, and delayed fluorescence; nonradiative processes: internal conversion (IC), intersystem crossing (ISC), and reverse intersystem crossing (RISC)).

Fluorescence is light emission of photons accompanying the relaxation from the S_1 to S_0 states (Equ. 1-1). Although emission of a photon is as fast as absorption of a photon, excited molecules stay in the S_1 state with a transition time of 10^{-10}–10^{-7} s before emitting a photon or undergoing other processes such as internal conversion (IC) and intersystem crossing (ISC).

$$S_0 + h\nu_{ex} \rightarrow S_1 \rightarrow S_0 + h\nu_{em} \tag{1-1}$$

At room temperature, nonradiative transition from the lowest excited triplet (T_1) to S_0 states is forbidden, but it can be observed as radiative transition called phosphorescence with a transition time of 10^{-6}–10 s owing to strong spin–orbit coupling (Equ. 1-2). On the contrary,

phosphorescence can be observed because of a long enough lifetime of the triplet state at low temperatures.

$$S_0 + h\nu_{ex} \rightarrow S_1 \rightarrow T_1 \rightarrow S_0 + h\nu_{em} \tag{1-2}$$

As shown in Figure 1-4, under electrical-excitation, organic materials show difference EL processes. From spin statistics of carrier recombination in OLEDs, singlet and triplet excitons are generated in 25% and 75%, respectively. For conventional fluorescence-based OLEDs, S_1 excitons of 25% can be utilized for light emission, because T_1 excitons undergo nonradiative deactivation processes.[9] Phosphorescent emitters containing rare metals can effectively convert both singlet and triplet excitons into light.[10] An internal EL quantum efficiency (η_{int}) of nearly 100% has been achieved for an OLED using an iridium complex as an emitter.[10c] In general, because strong spin-orbit coupling is necessary to effectively induce intersystem crossing and generate triplet excitons, the heavy-atom effect has been used to develop phosphorescent materials. As a result, transition metal complexes such as iridium, platinum, and osmium have been used as electrophosphorescent dopants in OLEDs.[10b]
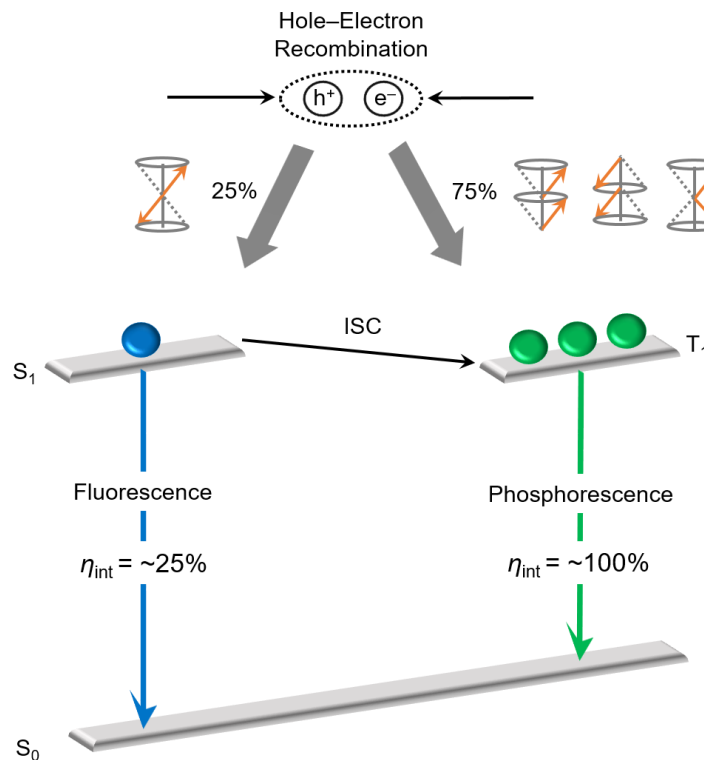
Figure 1-4. Schematic representation for fluorescence and phosphorescence mechanism under electrical-excitation. (η_{int}: internal EL quantum efficiency)

1. 2. 2 Thermally Activated Delayed Fluorescence (TADF)

Thermally activated delayed fluorescence (TADF) is a promising alternative to phosphorescence to convert triplet excitons into light as shown in Figure 1-5.[11] TADF emitters can realize highly efficient OLEDs without heavy metals, which is an advantage of TADF materials over phosphorescent ones. Using TADF emitters composed of dicyanobenzene and carbazole moieties, OLEDs showing maximum η_{ext} comparable to those obtained with phosphorescent dopants have been developed.[11a] In a TADF emitter, triplet states are converted into singlet states to emit delayed fluorescence.
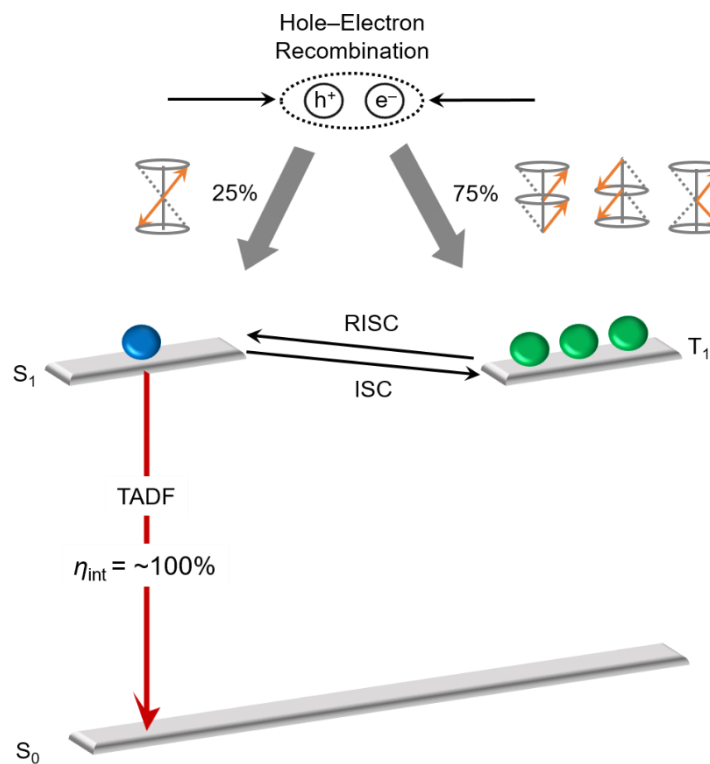
Figure 1-5. Schematic representation for thermally activated delayed fluorescence (TADF) mechanism under electrical-excitation. (η_{int}: internal EL quantum efficiency)

To promote delayed fluorescence via thermal energy ($k_{BT} \approx 25.6$ meV), a small energy gap (ΔE_{ST}) between the S_1 and T_1 states, is required, because the rate of $T_1 \rightarrow S_1$ reverse intersystem crossing (RISC) is inversely proportional to the exponential of ΔE_{ST} in accordance with Fermi's Golden rule (Equ. 1-3).[12]

$$k_{\mathrm{RISC}} = \frac{2\pi}{\hbar} < \Psi^1 |H_{\mathrm{SO}}| \Psi^2 >^2 \frac{1}{\sqrt{4\pi\lambda k_{\mathrm{B}}T}} \exp\left(-\frac{(\Delta E_{\mathrm{ST}} + \lambda)^2}{4\pi\lambda k_{\mathrm{B}}T} \right) \qquad (1\text{-}3)$$

where $\hbar$ is the Planck constant, H_{SO} is spin–orbit coupling between two states ($\Psi^1 \to \Psi^2$), λ is the mixing coefficient between two states ($\Psi^1 \to \Psi^2$), and k_B is the Boltzmann constant. Because ΔE_{ST} depends largely on the exchange interaction between electrons in molecular orbitals involved in an electronic excitation, it is necessary to control the spatial overlap between the highest occupied molecular orbital (HOMO) and the lowest unoccupied molecular orbital (LUMO). From assuming that S_0 energy is zero, the ΔE_{ST} is equal to twice of the electron exchange energy (J) as following equation.[13]

$$\Delta E_{ST} = |E_S - E_T| = 2J \tag{1-4}$$

where E_S and E_T are the energies of the S_1 and T_1 states, respectively.

J associated with the Pauli principle can be expressed by the following equation including the wavefunction of the HOMO and LUMO (Φ_H and Φ_L).

$$J = \iint \Phi_H(1)\Phi_L(2)\left(\frac{e^2}{r_{12}}\right)\Phi_L(2)\Phi_H(1)dr_1 dr_2 \tag{1-5}$$

where r_{12} is the distance separating the electrons. Thus, the ΔE_{ST} and RISC process can be controlled by separating the wavefunctions of the HOMO and LUMO in organic molecules.

Until a recent date, it is commonly believed that only the T_1 excitons up-converted to the S_1 state via the efficient RISC process because very fast internal conversion. However, Gibson et al.[14] reported that the stronger spin-vibronic coupling (H_{vib}) between the ^{3}CT and local excited (^{3}LE) triplet states than other coupling such as spin-orbit coupling leads to RISC from both ^{3}CT and ^{3}LE states. Therefore, considering spin-vibronic coupling, k_{risc} can be rewritten by following equation in accordance with second order perturbation theory[15]

$$k_{RISC} = \frac{2\pi}{\hbar}\left|\frac{\langle\Psi^1_{CT}|H_{SO}|\Psi^3_{LE}\rangle\langle\Psi^3_{LE}|H_{vib}|\Psi^3_{CT}\rangle}{\delta(E^3_{LE} - E^3_{CT})}\right|^2 \delta(E^3_{LE} - E^1_{CT}) \tag{1-6}$$

Photoluminescence (PL) and EL processes including two obvious unimolecular mechanisms (prompt and delayed fluorescence) for TADF are shown in the Figure1-6. Under the photo excitation, prompt and delayed fluorescence can be observed with different lifetimes although they exhibit similar spectral distributions.

The Φ_{PL} of the prompt component (Φ_{PF}) and delayed component (Φ_{DF}) are experimentally obtained from the emission intensity proportions of their components in the transient PL. The lifetimes of the prompt component (τ_{PF}) and delayed component (τ_{DF}) are determined by fitting a transient PL decay curve. In the presence of ISC and RISC between the S_1 and T_1 states, the rate constants of the prompt component (k_{PF}) and delayed component (k_{DF}) can be expressed by the following formulas:
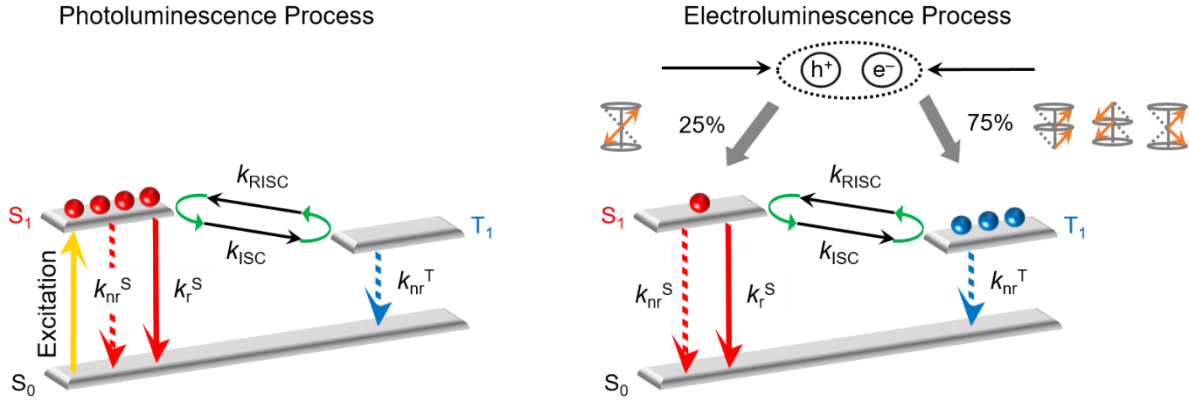
Figure 1-6. Photoluminescence (left) and electroluminescence (right) processes in TADF molecules. (k_r^s and k_{nr}^s are the rate constants of radiative and nonradiative decay (S$_1$→S$_0$), k_{nr}^T is the rate constant of nonradiative decay (T$_1$→S$_0$), k_{ISC} is the rate constant of ISC (S$_1$→T$_1$), and k_{RISC} is the rate constant of RISC (T$_1$→S$_1$)).

$$k_{PF} = \frac{1}{\tau_{PF}} = k_r^S + k_{nr}^S + k_{ISC} \tag{1-7}$$

$$k_{DF} = \frac{1}{\tau_{DF}} = k_{nr}^T + \left(1 - \frac{k_{ISC}}{k_r^S + k_{nr}^S + k_{ISC}}\right) k_{RISC} \tag{1-8}$$

where k_r^S and k_{nr}^S are the radiative and nonradiative decay rate constants of the S$_1$ state, respectively, and k_{ISC} and k_{RISC} are the ISC (S$_1$→T$_1$) and RISC (T$_1$→S$_1$) rate constants, respectively. k_r^S and k_{ISC} are assumed to be much faster than k_{nr}^T and k_{RISC}. The Φ_{PF}, Φ_{DF}, and Φ_{ISC} are given by the following formulas:[16]

$$\Phi_{PF} = \frac{k_r^S}{k_r^S + k_{nr}^S + k_{ISC}} = \frac{k_r^S}{k_{PF}} \tag{1-9}$$

$$\Phi_{DF} = \sum_{k=1}^{\infty} (\Phi_{ISC} \Phi_{RISC})^k \Phi_{PF} = \frac{\Phi_{ISC} \Phi_{RISC}}{1 - \Phi_{ISC} \Phi_{RISC}} \cdot \Phi_{PF} \tag{1-10}$$

$$\Phi_{ISC} = \frac{k_{ISC}}{k_r^S + k_{nr}^S + k_{ISC}} = \frac{k_{ISC}}{k_{PF}} \tag{1-11}$$

From Eqs. 1–11, the following equation can be obtained.

$$k_{RISC} = \frac{k_{PF} k_{DF}}{k_{ISC}} \frac{\Phi_{DF}}{\Phi_{PF}} \tag{1-12}$$

Since the Φ_{PF} exhibits almost negligible temperature dependence, we assume that $k_{nr}^S \approx 0$ at 300 K. Based on Eqs. 1–12, k_r^S, k_{ISC}, and k_{RISC} can be estimated.

In OLEDs, the η_{ext}, which describes the ratio of the number of emitted photons per the injected charge carriers can be calculated by the following equation.[17]

$$\eta_{\text{ext}} = \gamma \cdot \eta_{\text{S/T}} \cdot \Phi_{\text{PL}} \cdot \eta_{\text{out}} \tag{1-13}$$

where γ is the charge carrier balance factor or exciton formation fraction, η_{ST} is the exciton fraction resulting in the radiative transition according to the spin statistics, Φ_{PL} is the PL quantum efficiency, and η_{out} is the light out-coupling efficiency which is the fraction of the generated photons from the device to the outside. In TADF-OLEDs, γ and Φ_{PL} of 100% can be realized by optimizing the device architectures and suppressed energy loss through nonradiative deactivation processes with suitable molelcular design, respectively. The $\eta_{\text{S/T}}$ for TADF can reach 100% due to the efficient RISC from triplet to singlet states. Assuming η_{out} of 0.2, η_{ext} of TADF-OLEDs can be achieved high maximum η_{ext} of up to 20%.[11a] In TADF materials, the fraction of the singlet and triplet exciton (η_{S} and η_{T}) are 0.25 and 0.75, respectively. Therefore, the theoretical η_{ext} for TADF-OLEDs can be estimated by the following equation under the electrical excitation.

$$\eta_{\text{ext}} = \left[0.25\Phi_{\text{PF}} + \{0.75 + 0.25(1 - \Phi_{\text{PF}})\} \frac{\Phi_{\text{DF}}}{1 - \Phi_{\text{PF}}} \right] \gamma\eta_{\text{out}} \tag{1-14}$$

1. 2. 3 Energy Transfer Processes

Charge transfer excitons composed of seperated charges and singlet or triplet polaron pairs decay into the lower singlet or triplet excited states.[2] The electronic coupling between spin-singlet electrons is induced by dipole-dipole interactions (so-called Förster-type transfer).[18] However, the electronic coupling of triplet and singlet transfer is dominated by the exchange coupling (so-called Dexter-type transfer)[19] as shown in Figure 1-7.

I.   Long-Range Dipole–Dipole Transfer

Energy transfer can occur through a dipole–dipole interaction (Coulombic) known as Förster energy transfer, which requires the overlap of an emission spectrum of a donor and an absorption spectrum of an acceptor. The energy of the excited donor molecule is released and transferred to the ground state of the acceptor molecule. At this mechanism without the direct overlap, the energy transfer via dipole–dipole interactions can overcome distances up to 10 nm and is only allowed singlet–singlet energy transfer, without a change of spin multiplicity. The rate constant of Förster energy transfer is described as following expression.[8]

$$k_{\text{T}}^{\text{dd}} = k_{\text{D}} \left[\frac{R_{\text{o}}}{r} \right]^6 = \frac{1}{\tau_{\text{D}}^{\text{o}}} \left[\frac{R_0}{r} \right]^6 \tag{1-15}$$
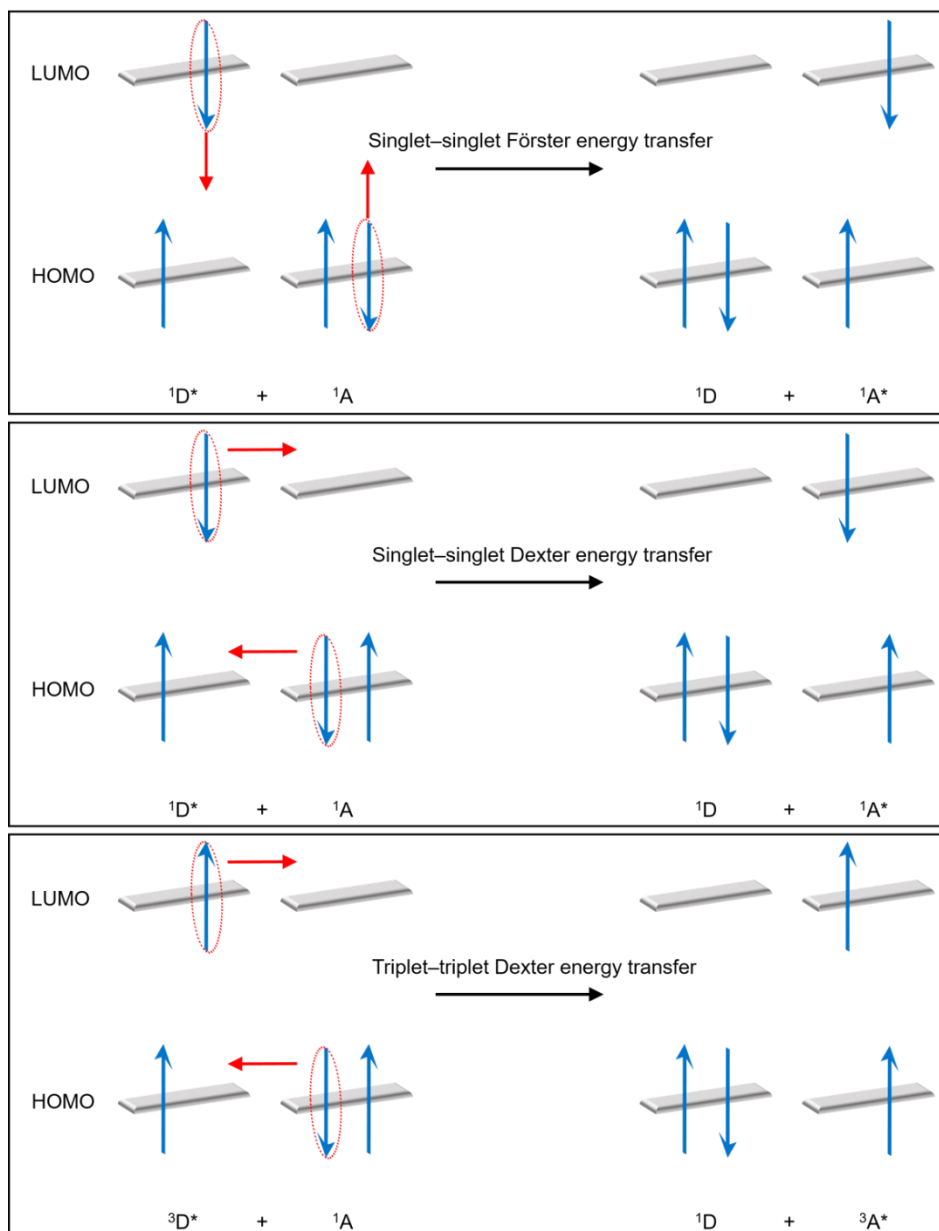
Figure 1-7. Schematic representation for singlet–singlet Förster energy transfer, singlet–singlet Dexter energy transfer, and triplet–triplet Dexter energy transfer.

where k_D is the emission rate constant of the donor, $\tau_D{}^0$ is lifetime in the absence of transfer, r is the distance between the donor and acceptor, and R_0 is the critical distance or Förster radius (the distance when transfer and decay of the excited donor are equal). The Förster radius is expressed by the following equation.

$$R_0^6 = \frac{9(\ln 10)\kappa^2 \Phi_D^0}{128\pi^5 N_A n^4} J \tag{1-16}$$

where κ^2 is the dipole orientation factor, Φ_D is the PL quantum efficiency of the donor in the absence of transfer, N_A is the Avogadro's number, n is the refractive index of the medium, and J is the spectral integral can be expressed by

$$J = \int F_\lambda(\lambda)\varepsilon(\lambda)\lambda^4 d\lambda \tag{1-17}$$

F_λ is the normalized emission spectrum of the donor and ε is molar extinction coefficient from the absorption of the acceptor.

II. Exchange Energy Transfer

Energy transfer based on exchange interactions known as Dexter energy transfer requires the strong spatial overlap of the wavefunctions of the donor and acceptor molecules. The electronic wavefunction overlap decays exponential dependence with the distance between the donor and acceptor, and this mechamism, which is allowed both singlet–singlet and triplet–triplet energy transfer, occurs over short distances in the range of up to 1 nm. The rate constant of Dexter energy transfer can be written as[8]

$$k_T^{ex} = k_0 \exp\left[-\frac{2(1-R_c)}{L}\right] \tag{1-18}$$

where R_c is the collisional radius and L is the Bohr radius, respectively.

1. 2. 4 Annihilation Processes

Energy transfer between one excited state and another which is termed annihilation, results in the loss of excitons. The annihilation processes, which are caused by either two excitons or an exciton with a polaron and hence lead to decrease of the EL quantum efficiency with increasing current density, paly crucial roles in the performance of OLEDs. Under electrical-excitation, both excitons and polarons of excited molecules undergo several annihilation processes as shown in Figure 1-8.[20]

I. Singlet–Singlet Annihilation (SSA)

SSA occurred between two excited singlet states is primarily relevant to efficiency roll-off in fluorescent OLEDs. Singlet excitons undergo annihilation themselves owing to Förster energy transfer, results from dipole–dipole interactions.[21] Therefore, this annihilation usually pronounced in crystaline and it was firstly observed in anthracene crystals.[21,22] SSA can be described as the following processes.

$$S_1 + S_1 \xrightarrow{k_{SSA}} S_0 + S_n^* \xrightarrow{IC} S_0 + S_1 + \text{heat} \tag{1-19}$$

where k_{SSA} is the rate constant of SSA.

II. Singlet–Triplet Annihilation (STA)

A further annihilation proccess can occur by interactions between the singlet and triplet excited states.While this STA is observed in conventional fluorescent[23] and TADF[24]-based OLEDs, it is negligible in phosphorescent OLEDs becuase singlet excitons undergo fast ISC from the S_1 to T_1 states. Singlet–triplet quenching through the energy transfer which are attributable to long-range dipole–dipole interactions,[22,25] was confirmed by modeling the singlet and triplet population dynamics.[26]

$$S_1 + T_1 \xrightarrow{k_{STA}} S_0 + T_n^* \xrightarrow{IC} S_0 + T_1 + heat \qquad (1\text{-}20)$$

where k_{STA} is the rate constant of STA.
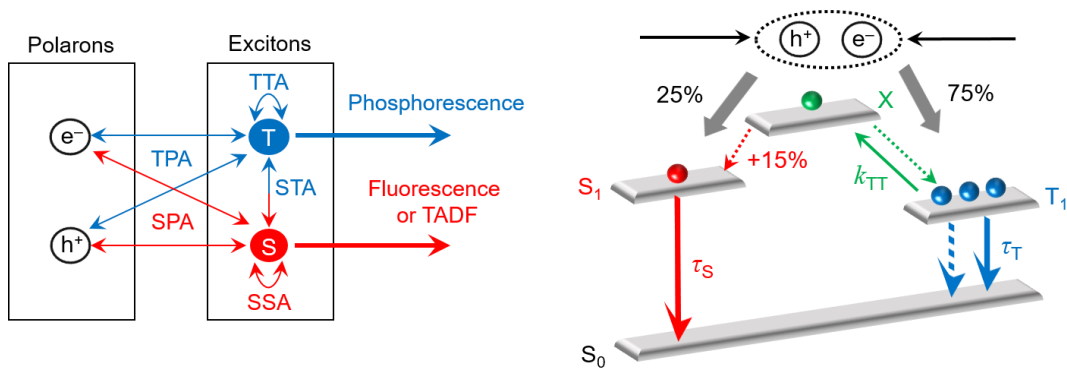
Figure 1-8. Schematic illustration of efficiency roll-off mechanisms in OLEDs. The mechanisms involve several broad categories of bimolecular annihilation processes (SSA: singlet–singlet annihilation, STA: singlet–triplet annihilation, TTA: triplet–triplet annihilation, SPA: singlet–polaron annihilation, and TPA: triplet–polaron annihilation)

III. Triplet–Triplet Annihilation (TTA)

TTA occurred between two excited triplet states is mostly relevant to efficiency roll-off in phosphorescent[27] and TADF[11a,24,28]-based OLEDs. Singlet exciton annihilation tend to based on Förster energy transfer; on the contrary, TTA proceeds via Dexter energy transfer. In this TTA processes by exchange energy transfer, two triplet excitons react to produce singlet states. Whereas the conventional fluorescent OLEDs have radiative lifetimes of a nanosecond scale, the long lifetimes of excited triplet excitons of a microsecond scale are observed in the phosphorescent[27,29] and TADF[11a,28]-OLEDs. As a consquence, although the high η_{int} of nearly 100% has been achieved, severe efficiency roll-off at high brightness are observed in phosphorescent and TADF-based OLEDs owing to relatively long excited-state lifetimes of triplet excitons.

Moreover, in a host–guest system, the emitting molecules are doped into a host material which has a higher triplet energy level than that of the guest molecules to avoid concentration quenching.[30] In this system, various forms[31] (guest–guest, host–guest,[29a] and host–host[32]) of TTA can occur between the excited guest and host materials. TTA can be described as the following processes.

$$T_1 + T_1 \xrightarrow{k_{TTA}} \begin{cases} S_0 + S_n^* \\ S_0 + T_n^* \end{cases} \tag{1-21}$$

where k_{TTA} is the rate constant of TTA.

IV. Exciton–Polaron Annihilation

In contrast to the interactions between two excitons, the annihilation processes of excitons by polarons such as singlet–polaron annihilation (SPA)[33] and triplet–polaron annihilation (TPA)[28a,31,34] occur in the excited singlet or triplet states with free or trapped charge carriers.

STA and TPA are possible via the following processes, respectively.

$$S_1 + D_0 \xrightarrow{k_{SPA}} S_0 + D_n^* \xrightarrow{IC} S_0 + D_0 + heat \tag{1-22}$$

$$T_1 + D_0 \xrightarrow{k_{TPA}} S_0 + D_n^* \xrightarrow{IC} S_0 + D_0 + heat \tag{1-23}$$
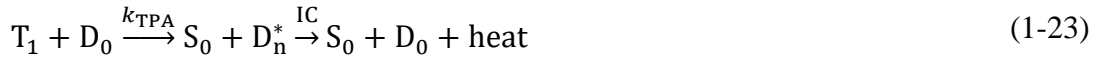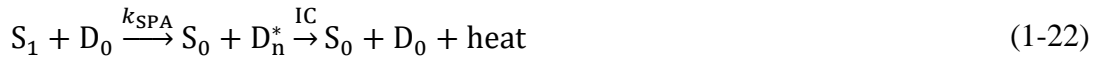
where D is the spin state of polaron, k_{SPA} is the rate constant of SPA, and k_{TPA} is the rate constant of TPA.

To realize OLEDs for high-brightness applications, several concepts have been introduced by decreasing the exciton lifetime,[35] reducing molecular aggregation,[36] and broadening of the recombination zone.[37]

1. 3 Motivation and Outline of This Dissertation

Inorganic light-emitting diodes (ILEDs), which enable form displays with performance advantages in brightness, lifetime, and efficiency that can exceed those of organic light-emitting diodes (OLEDs), have made great progress in application of general illumination and full-color displays. However, these ILED displays have only been applied in ultralarge-area such as billboard displays limited by assembly procedures that do not require small and thin light source and high-pixel count arrays.[38] OLEDs as potential alternatives to conventional inorganic devices owing to their ability to be deposited onto large-area flexible substrates, have been drawing considerable attention for their practical applications in flexible displays and solid-state lighting sources for architectural or automotive lighting because of their unique advantages such as high electroluminescence (EL) efficiency, flexibility, high contrast, light

weight, and low manufacturing costs. In OLEDs, electrically injected holes and electrons recombine to form singlet and triplet excitons in the ratio of 25% and 75%, respectively, according to spin statistics. Therefore, in conventional fluorescent OLEDs, only the lowest singlet (S_1) excitons can be utilized for light emission because the lowest triplet (T_1) excitons undergo a spin forbidden transition, resulting in nonradiative deactivation processes. Meanwhile, organometallic phosphorescent materials containing rare metals can effectively convert both S_1 and T_1 excitons into light emission. Despite their desirable EL characteristics, phosphorescent materials still have some drawbacks such as the rarity, toxicity, and high cost of the used rare metals. As an alternative, thermally activated delayed fluorescence (TADF) materials have recently emerged as a promising class of organic luminophores for the production of high-efficiency OLEDs without using rare metals. TADF emitters, which have a small energy difference (ΔE_{ST}) between the S_1 and T_1 states, enable efficient reverse intersystem crossing (RISC) from their T_1 to S_1 states via thermal activation, and hence lead to the high internal EL quantum efficiency close to unity. The basic design strategy for achieving such a small ΔE_{ST} in donor–acceptor (D–A) molecules is to minimize the spatial overlap between the highest occupied molecular orbital (HOMO) and the lowest unoccupied molecular orbital (LUMO), in accordance with reduced electron-exchange interactions, by localizing these orbitals on the donor and acceptor constituents, respectively. This dissertation focuses on molecular design, synthesis, and properties of highly efficient TADF materials for OLEDs.

In general, inevitable concentration quenching of TADF emitters in the solid state leads to the reduction in photoluminescence and EL efficiencies; however, the mechanism remains to be elucidated. Therefore, **Chapter 2** deals with a design strategy of xanthone-based TADF materials for inhibiting concentration quenching in OLEDs. In **Chapter 3**, regioisomeric xanthone-based TADF materials were investigated their twisted intramolecular charge transfer and completely applied to blue OLEDs. Up to date, previous reported blue TADF-based OLEDs suffer from the exciton annihilation processes, which are caused by their relatively long excited state lifetimes at high current density. Therefore, **Chapter 4** suggests a molecular design concept for reduced efficiency roll-off in blue TADF-OLEDs by introducing isobenzofuranone and chromone as new acceptors. **Chapter 5** provides a design way of oxadiazole- and triazole-based TADF materials by employing D–A–D and D–A molecular architectures, and their structure-property relationship was investigated. **Chapter 6** describes photophysical properties such as emission color and singlet–triplet energy gaps of phenazine-based TADF materials. Finally, **Chapter 7** summarizes this dissertation.

References

[1]   a) J. Kido, M. Kimura, K. Nagai, *Science* **1995**, *267*, 1332; b) S. Reineke, F. Lindner, G. Schwartz, N. Seidler, K. Walzer, B. Lüssem, K. Leo, *Nature* **2009**, *459*, 234; c) M. A. McCarthy, B. Liu, E. P. Donghue, I. Kravchenko, D. Y. Kim, F. So, A. G. Rinzler, *Science* **2011**, *332*, 570.

[2]   A. Buckley, *Organic Light-Emitting Diodes (OLEDs): Materials, Devices and Applications*, Woodhead Publishing Limited, Philadelphia, **2013**.

[3]   H. Yersin, *Highly Efficient OLEDs with Phosphorescent Materials*, WILEY-VCH, Weinheim, **2008**.

[4]   M. A. Baldo, D. F. O'Brien, Y. You, A. Shoustikov, S. Sibley, M. E. Thompson, S. R. Forrest, *Nature* **1998**, *395*, 151.

[5]   a) A. Bernanose, M. Comte, P, Vouaux, *J. Chim. Phys.* **1953**, *50*, 64; b) A. Bernanose, P. Vouaux, *J. Chim. Phys.* **1953**, *50*, 261; c) A. Bernanose, *J. Chim. Phys.* **1955**, *52*, 396; d) A. Bernanose, P. Vouaux, *J. Chim. Phys.* **1955**, *52*, 509.

[6]   W. Helfrich, W. G. Schneider, *Phys. Rev. Lett.* **1965**, *14*, 229.

[7]   C. W. Tang, S. A. VanSlyke, *Appl. Phys. Lett.* **1987**, *51*, 913.

[8]   B. Valeur, M. N. Berberan-Santos, *Molecular Fluorescence*, WILEY-VCH, Weinheim, **2012**.

[9]   L. J. Rothberg, A. J. Lovinger, *J. Mater. Res.* **1996**, *11*, 3174.

[10]   a) M. A. Baldo, S. Lamansky, P. E. Burrows, M. E. Thompson and S. R. Forrest, *Appl. Phys. Lett.* **1999**, *75*, 4; b) M. A. Baldo, M. E. Thompson and S. R. Forrest, *Pure Appl. Chem.* **1999**, *71*, 2095; c) C. Adachi, M. A. Baldo, M. E. Thompson and S. R. Forrest, *J. Appl. Phys.* **2001**, *90*, 5048.

[11]   a) H. Uoyama, K. Goushi, H. Nomura, C. Adachi, *Nature* **2012**, *492*, 234; b) T. Nishimoto, T. Yasuda, S. Y. Lee, R. Kondo, C. Adachi, *Mater. Horiz.* **2014**, *1*, 264; c) Y. J. Cho, B. D. Chin, S. K. Jeon, J. Y. Lee, *Adv. Mater.* **2015**, *25*, 6786; d) Y. J. Cho, S. K. Jeon, B. D. Chin, E. Yu, J. Y. Lee, *Angew. Chem. Int. Ed.* **2015**, *54*, 5201; e) S. Wang, X. Yan, Z. Cheng, H. Zhang, Y. Liu, Y. Wang, *Angew. Chem. Int. Ed.* **2015**, *54*, 13068; f) S. Hirata, Y. Sakai, K. Masui, H. Tanaka, S. Y. Lee, H. Nomura, N. Nakamura, M. Yasumatsu, H. Nakanotani, Q. Zhang, K. Shizu, H. Miyazaki, C. Adachi, *Nat. Mater.* **2015**, *14*, 330; g) M. Kim, S. K. Jeon, S.-H. Hwang, J. Y. Lee, *Adv. Mater.* **2015**, *27*, 2515; h) D. Y. Lee, M. Kim, S. K. Jeon, S.-H. Hwang, C. W. Lee, J. Y. Lee, *Adv. Mater.* **2015**, *27*, 5861; i) J. W. Sun, J. Y. Baek, K.-H. Kim, C.-K. Moon, J.-H. Lee, S.-K. Kwon,

Y.-H. Kim, J.-J. Kim, *Chem. Mater.* **2015**, *27*, 6675; j) Q. Zhang, J. Li, K. Shizu, S. Huang, S. Hirata, H. Miyazaki, C. Adachi, *J. Am. Chem. Soc.* **2012**, *134*, 14706; k) Q. Zhang, B. Li, S. Huang, H. Nomura, H. Tanaka, C. Adachi, *Nat. Photon.* **2014**, *8*, 326; l) F. B. Dias, K. N. Bourdakos, V. Jankus, K. C. Moss, K. T. Kamtekar, V. Bhalla, J. Santos, M. R. Bryce, A. P. Monkman, *Adv. Mater.* **2013**, *25*, 3707; m) H. Wang, L. Xie, Q. Peng, L. Meng, Y. Wang, Y. Yi, P. Wang, *Adv. Mater.* **2014**, *26*, 5198; n) Z. Xie, C. Chen, S. Xu, J. Li, Y. Zhang, S. Liu, J. Xu, Z. Chi, *Angew. Chem. Int. Ed.* **2015**, *54*, 7181; o) S. Y. Lee, T. Yasuda, Y. S. Yang, Q. Zhang, C. Adachi, *Angew. Chem. Int. Ed.* **2014**, *126*, 6520; p) Q. Zhang, D. Tsang, H. Kuwabara, Y. Hatae, B. Li, T. Takahashi, S. Y. Lee, T. Yasuda, C. Adachi, *Adv. Mater.* **2015**, *27*, 2096; q) G. Méhes, H. Nomura, Q. Zhang, T. Nakagawa, C. Adachi, *Angew. Chem. Int. Ed.* **2012**, *51*, 11311; r) M. Numata, T. Yasuda, C. Adachi, *Chem. Commun.* **2015**, *51*, 9443.

[12]   a) N. J. Turro, V. Ramamurthy, J. C. Scaiano, *Modern Molecular Photochemistry of Organic Molecules,* University Science Books, Sausalito, **2010**; b) Y. Tao, K. Tuan, T. Chen, P. Xu, H. Li, R. Chen, C. Zheng, L. Zhang, W. Huang, *Adv. Mater.* **2014**, *26*, 7931.

[13]   N. Aizawa, I. S. Park, T. Yasuda, *AAPPS Bull.* **2016**, *26*, 9.

[14]   J. Gibson, A. P. Monkman, T. J. Penfold, *ChemPhysChem* **2016**, *17*, 2956.

[15]   M. K. Etherington, J. Gibson, H. F. Higginbotham, T. J. Penfold, A. P. Monkman, *Nat. Commun.* **2016**, *7*, 13680.

[16]   K. Goushi, K. Yoshida, K. Sato, C. Adachi, *Nat. Photon.* **2012**, *6*, 253.

[17]   W. Brütting, C. Adachi, *Physics of Organic Semiconductors*, Wiley-VCH, Weinheim, **2012**.

[18]   T, Forster, *Annalender Physik*, **1948**, *2*, 55.

[19]   D. L. Dexter, *J. Chem. Phys.* **1953**, *21*, 836.

[20]   C. Murawski, K. Leo, M. C. Gather, *Adv. Mater.* **2013**, *25*, 6801.

[21]   S. D. Babenko, V. A. Benderskii, V. I. Gol'Danskii, A. G. Lavrushko, V. P. Tychinskii, *Chem. Phys. Lett.* **1971**, *8*, 598.

[22]   M. Pope, C. E. Swenberg, *Electric Processes in Organic Crystals, Clarendon Press*, Oxford University Press, **1982**.

[23]   a) J. Fourny, G. Delacote, *Phys. Rev. Lett.* **1968**, *21*, 1085; b) Y. Zhang, M. Whited, M. E. Thompson, S. R. Forrest, *Chem. Phys. Lett.* **2010**, *495*, 161; c) D. Kasemann, R. Brückner, H. Fröb, K. Leo, *Phys. Rev. B* **2011**, *84*, 115208.

[24]   K. Masui, H. Nakanotani, C. Adachi, *Org. Electron.* **2013**, *14*, 2721.

[25]   N. Giebink, S. R. Forrest, *Phys. Rev. B* **2009**, *79*, 073302.

[26]   Y. Zhang, M. Whited, M. E. Thompson, S. R. Forrest, *Chem. Phys. Lett.* **2010**, *495*, 161.

[27]   M. A. Baldo, D. F O'Brien, Y. You, A. Shoustikov, S. Sibley, M. E. Thompson, S. R. Forrest, *Nature* **1998**, *395*, 151.

[28]   S. Y. Lee, T. Yasuda, H. Nomura, C. Adachi, *Appl*. *Phys*. *Lett*. **2012**, *101*, 093306.

[29]   a) M. A. Baldo, C. Adachi, S. R. Forrest, *Phys. Rev. B* **2000**, *62*, 10967; b) N. C. Giebink, S. R. Forrest, *Phys. Rev. B* **2008**, *77*, 235215; c) C. Murawski, K. Leo, M. C. Gather, *Adv. Mater.* **2013**, *25*, 6801.

[30]   Y. Kawamura, J. Brooks, J. J. Brown, H. Sasabe, C. Adachi, *Phys. Rev. Lett.* **2006**, *96*, 17404.

[31]   S. Reineke, K. Walzer, K. Leo, *Phys. Rev. B* **2007**, *75*, 125328.

[32]   a) Y. Sun, N. C. Giebink, H. Kanno, B. Ma, M. E. Thompson, S. R. Forrest, *Nature* **2006**, *440*, 908; b) G. Schwartz, S. Reineke, T. C. Rosenow, K. Walzer, K. Leo, *Adv. Funct. Mater.* **2009**, *19*, 1319; c) T. C. Rosenow, M. Furno, S. Reineke, S. Olthof, B. Lüssem, K. Leo, *J. Appl. Phys.* **2010**, *108*, 11331133.

[33]   M. A. Baldo, R. J. Homes, S. R. Forrest, *Phys. Rev. B* **2002**, *66*, 035321.

[34]   J. Kalinowski, W. Stampor, J. Mezyk, M. Cocchi. D. Virgili, V. Fattori. P. Di Marco, *Phys. Rev. B* **2002**, *66*, 235321.

[35]   a) H. Yersin, A. F. Rausch, R. Czerwieniec, T. Hofbeck, T. Fischer, *Coord. Chem. Rev.* **2011**, *255*, 2622; b) L. Han, D. Yang, W. Li, B. Chu, Y. Chen, Z. Su, D. Zhang, F. Yan, Z. Hu, Z. Zhang, *Appl. Phys. Lett.* **2008**, *93*, 153303.

[36]   a) Y. Kawamura, L. Brooks, J. J. Brown, H. Sasabe, C. Adachi. *Phys. Rev. Lett.* **2006**, *96*, 17404; b) S. Reineke, T. C. Rosenow, B. Lussem, K. Leo, *Adv. Mater.* **2010**, *22*, 3189.

[37]   a) J. Lee, J.-I. Lee, J. Y. Lee, H. Y. Chu, *Org. Electron.* **2009**, *10*, 1529; b) G. He, M. Pfeiffer, K. Leo, M. Hofmann, J. Birnstock, R. Pudzich, J. Salbeck, *Appl. Phys. Lett.* **2004**, *85*, 3911; c) M.-T. Lee, J.-S. Lin, M-T. Chu, M.-R. Tseng, *Appl. Phys. Lett.* **2009**, *94*, 083506; d) J.-W. Kang, S.-H. Lee, H.-D. Park, W.-I. Jeong, K.-M. Yoo, Y.-S. Park, J.-J. Kim, *Appl. Phys. Lett.* **2007**, *90*, 223508.

[38]   S.-I. Park, Y. Xiong, R.-H. Kim, P. Elvikis, M. Meitl, D.-H. Kim, J. Wu, J. Yoon, C.-J. Yu,Z. Liu,Y. Huang, K. Hwang, P. Ferreira, X. Li, K. Choquette, J. A.Rogers, *Science* **2009**, 325, 977.

Chapter 2

Xanthone-Based Thermally Activated Delayed Fluorescence Materials for Inhibiting Concentration Quenching in Organic Light-Emitting Diodes
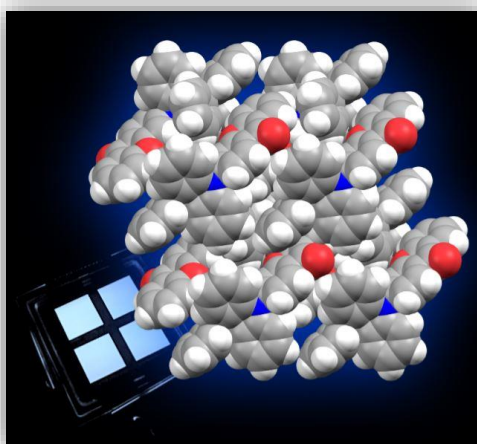
2. 1 Introduction

Recent developments in organic semiconductors have led to considerable improvements in the performance of OLEDs.[1] The use of TADF based on intramolecular donor–acceptor (D–A) molecules allows for internal electroluminescence (EL) quantum efficiencies (η_{int}) of OLEDs that approach ~100% by means of up-conversion of non-radiative triplet excitons to radiative singlet excitons through reverse intersystem crossing (RISC).[2] However, owing to their long-lasting excited states, such TADF molecules generally have a strong tendency to undergo aggregation-caused emission quenching (so-called concentration quenching) in condensed states or solid thin films, which causes significant energy loss through non-radiative deactivation processes. To circumvent this fundamental problem, host–guest systems have been adopted for the fabrication of TADF OLEDs by dispersing the emissive TADF molecules as a guest in a wide-bandgap solid host matrix;[2a–2f] however, this approach requires complex manufacturing techniques and involves a high cost associated with precise co-evaporation processes.

In conventional fluorescent emitters, Förster energy transfer based on long-range dipole–dipole interactions often accounts for concentration quenching, which dampens the radiative excitons through multiple energy-transfer events.[3] Likewise, such concentration quenching phenomenon is observed in phosphorescent iridium complexes, such as *fac*-tris(2-phenylpyridinato)iridium(III) (Ir(ppy)$_3$), as a result of their reasonably large spectral overlap between the lowest-energy absorption and the corresponding phosphorescence emission originating from the triplet metal-to-ligand charge transfer.[4] In phosphorescent OLEDs, single-step Förster energy transfer at high exciton densities leads to bimolecular exciton quenching such as triplet–triplet annihilation.[5] For TADF emitters, the factors affecting concentration quenching have yet to be clarified. Unlike conventional fluorescent and phosphorescent emitters, Förster energy transfer does not appear to be a feasible mechanism for TADF emitters with D–A electronic structures because of their much larger Stokes shift and hence smaller spectral overlap between their absorptions and corresponding emissions for the lowest-energy intramolecular charge-transfer (ICT) transitions.

In this chapter, the author demonstrates that even a small modulation in molecular geometric structures greatly affects concentration quenching of TADF, and hence can drastically enhance the quantum efficiencies of solid-state photoluminescence (PL) and EL. The exciton-quenching rates of TADF emitters show an exponential dependence on their intermolecular distance in thin films, revealing that electron-exchange interactions of triplet excitons, as described by the

Dexter energy-transfer model, dominate the concentration quenching of TADF. This mechanism stands in marked contrast to those of conventional fluorescent and phosphorescent emitters involving Förster energy transfer.

2. 2 Molecular Design and Quantum Chemical Calculations

To clarify the actual mechanism of concentration quenching of TADF, a new series of D–A molecules consisting of a xanthone (XT) acceptor unit coupled with different donor units (Figure 2-1), namely, 1,3,6,8-tetramethylcarbazole (MCz); 9,9-diphenylacridan (PAc); spiro[acridan-9,9′-xanthene] (XAc); and spiro[acridan-9,9′-fluorene] (FAc) was designed. In previous papers,[2g,2i] benzophenone was employed as an acceptor for efficient TADF, which exhibited efficient full-color TADF emission as well as high EL efficiencies in benzophenone-based TADF-OLEDs. However, benzophenone itself has strong electron withdrawing ability, which lead to difficulty to design for blue TADF molecules. For example, previous reported benzophenone-based TADF molecules, Cz2BP (4,4'-bis(9*H*-carbazol-9-yl)methanone) and CC2BP (4,4'-bis{3-(9*H*-carbazol-9-yl)-9*H*-carbazol-9-yl}methanone), displayed efficient TADF properties.[2i] Unfortunately, these materials have very long emission lifetimes of over 460 μs as well as relatively low Φ_{PL} of 55% and 73%, respectively, which are because their low RISC efficiencies of less than 69%, results from their large ΔE_{ST} of 0.21 and 0.14 eV, respectively. As another exemplar, DMAC-BP (bis[4-(9,9-dimethyl-9,10-dihydroacridine)phenyl]methanone) comprising benzophenone as an acceptor with dimethylacridan as a donor unit was reported.[2g] Although this material demonstrated efficient TADF properties and a high Φ_{PL} owing its short emission lifetime, green emission was observed because the dimethylacridan donor unit possesses stronger electron-donating ability than carbazole and bicarbazole donor units. To realize efficient blue TADF utilizing the aromatic ketone acceptor and acridan donor units with both high Φ_{PL} and short emission lifetime, xanthone was employed as an acceptor because its weaker electron-withdrawing ability than benzophenone caused by the electron-donating oxygen atom in the xanthone molecule.
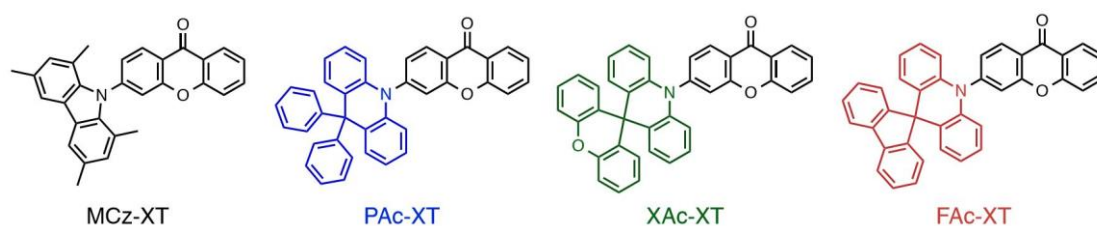
Figure 2-1. Molecular structures of xanthone (XT)-based TADF emitters.

To gain insights into the geometrical and electronic properties of MCz-XT, PAc-XT, XAc-XT, and FAc-XT at the molecular level, natural transition orbitals (NTOs) for the singlet state of the compounds were calculated by time-dependent density functional theory (TD-DFT) method. As displayed in Figure 2-2, all of these molecules adopt nearly orthogonal D–A conformation in their optimized structures, with dihedral angles of 87–90°, between the XT units and the acridan (or carbazole) unit. Because of such highly twisted geometry between the donor and acceptor constituents, the highest occupied NTOs are thoroughly localized on the electron-donating donor moiety, whereas the lowest unoccupied NTOs are predominantly distributed over the electron-accepting xanthone units. Therefore, this clear separation of the NTOs leads to small calculated the energy difference between the lowest-excited singlet and triplet states (ΔE_{ST}) values of 0.01–0.03 eV for these molecules, allowing for efficient RISC.

Geometry   Highest occupied NTO   Lowest occupied NTO
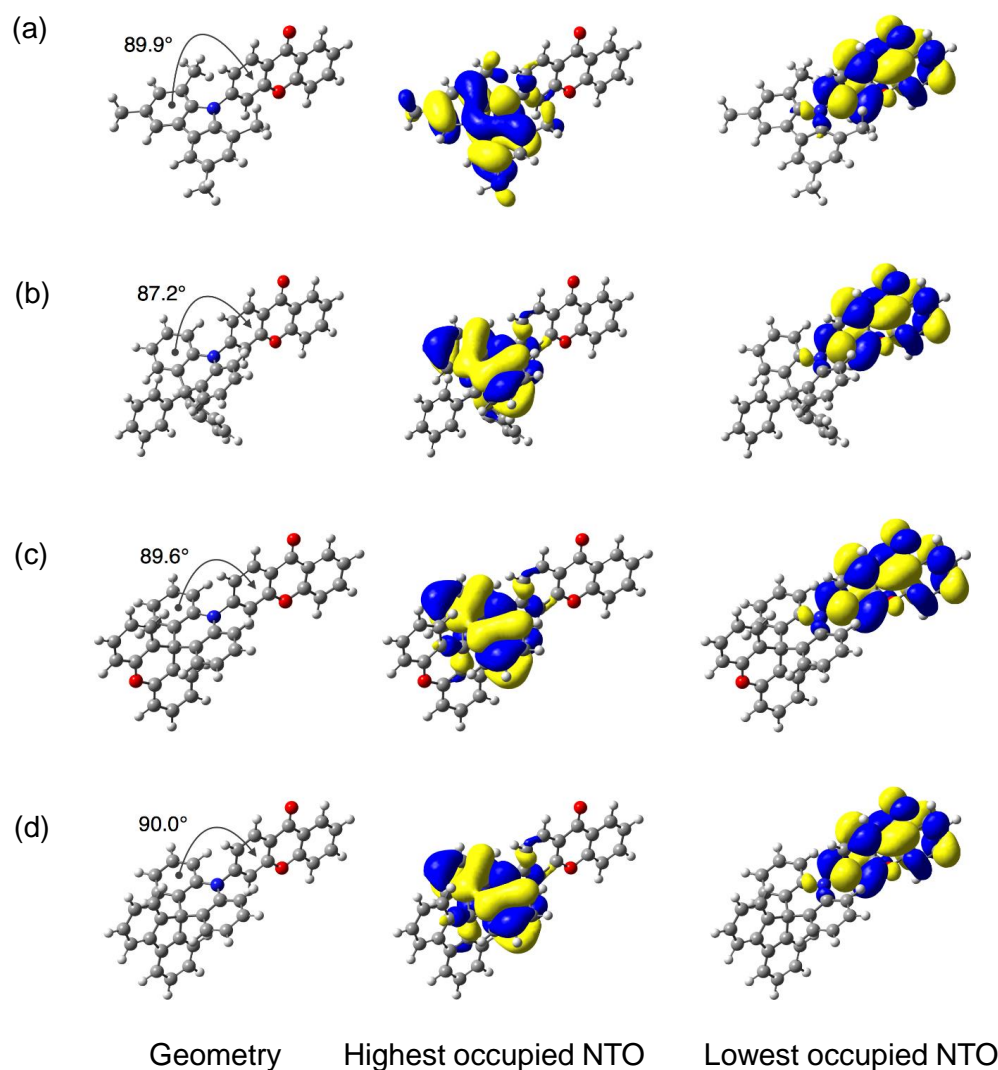
Figure 2-2. Calculated configurations and natural transition orbitals of the lowest excited singlet states of (a) MCz-XT, (b) PAc-XT, (c) XAc-XT, and (d) FAc-XT calculated. The isovalue is 0.02.

2. 3 Photophysical and TADF Properties

Similar to previously reported TADF emitters with D–A structures,[2c–2h] these four XT-based molecules exhibited two exponential PL decay components for light-blue emissions centered around 480 nm upon photo-excitation (Figure 2-3), which consisted of prompt fluorescence with a transient lifetime (τ_{PF}) of 32–39 ns, followed by delayed fluorescence (TADF) with a lifetime (τ_{DF}) of 1.2–3.3 µs in oxygen-free toluene solutions. Moreover, the emission spectra of the prompt fluorescence and the delayed fluorescence coincide with each other, indicating that the delayed fluorescence originated from the same lowest-excited singlet state populated via thermally assisted up-conversion. The PL quantum efficiencies (Φ_{PL}) of the XT-based TADF molecules were drastically enhanced by removing triplet oxygen (Table 2-1) because of acceleration of the RISC processes.

(a)   (b)
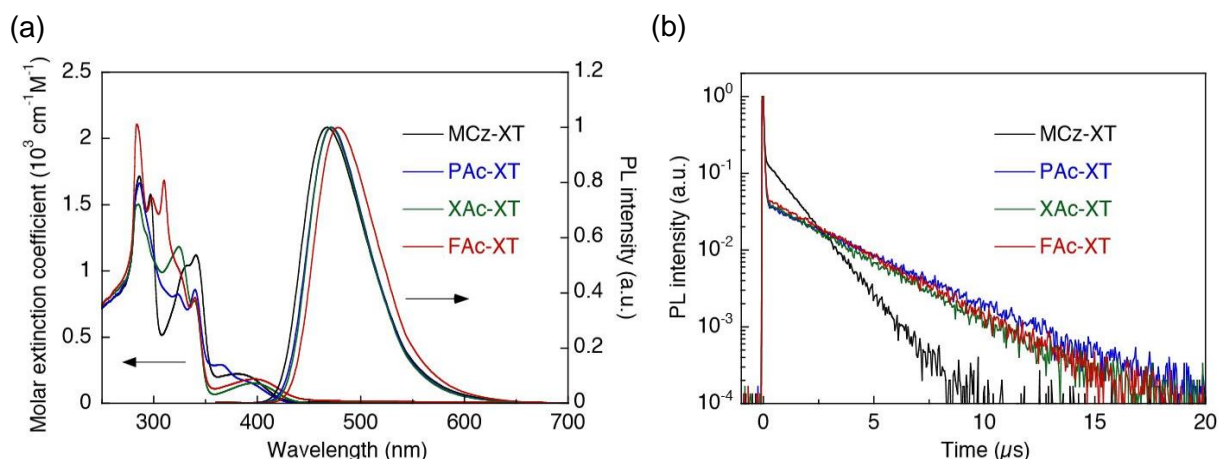
Figure 2-3. (a) Steady-state ultraviolet-visible (UV-vis) absorption and photoluminescence (PL) spectra. (b) Transient PL decay characteristics of the four XT-based TADF molecules in oxygen-free toluene solutions (1.0×10^{-5} M).

Table 2-1. PL properties of the XT-based TADF emitters in 1.0×10^{-5} M toluene solutions

Emitter	In aerated solution			After N$_2$ bubbling		
	Φ_{PL} (%)	τ_{PF} (ns)	τ_{DF} (µs)	Φ_{PL} (%)	τ_{PF} (ns)	τ_{DF} (µs)
MCz-XT	13.8	15.0	n.d.	83.0	32.8	1.23
PAc-XT	16.9	16.3	n.d.	75.6	36.8	3.23
XAc-XT	16.0	15.7	n.d.	77.3	36.7	2.70
FAc-XT	16.4	16.1	n.d.	82.2	38.7	2.81

To evaluate ΔE_{ST} of the XT-based TADF molecules (MCz-XT, PAc-XT, XAc-XT, and FAc-XT), the temperature dependence of the rate constants of RISC (k_{RISC}) was analyzed (Figure 2-

4). To confine the triplet excitons within the TADF molecules, 2,8-bis(diphenylphosphoryl)dibenzo[*b,d*]furan (PPF),[6] which possesses a high excited triplet energy of 3.1 eV, was selected as the solid host matrix. Assuming that RISC is much slower than intersystem crossing (ISC),[2f,7] k_{RISC} can be experimentally determined using equation (2-1):

$$k_{RISC} = \frac{k_{PF}k_{DF}}{k_{PF} - k_{ISC}} \tag{2-1}$$

where k_{PF} and k_{DF} are the measurable rate constants of prompt and delayed fluorescence, respectively, and k_{ISC} is the rate constant of ISC. From the Arrhenius plots of k_{RISC} (Figure 2-4), the activation energies, which correspond to the ΔE_{ST} values of the XT-based TADF molecules were estimated to be 11–25 meV (Table 2-2). These ΔE_{ST} values are sufficiently lower than the thermal energy of 25.9 meV at 300 K, indicating that RISC occurred efficiently in these XT-based molecules. Similar small ΔE_{ST} values were obtained experimentally[8] and computationally[9] in 3-(9,9-dimethylacridin-10(9*H*)-yl)-9*H*-xanthen-9-one (ACRXTN).
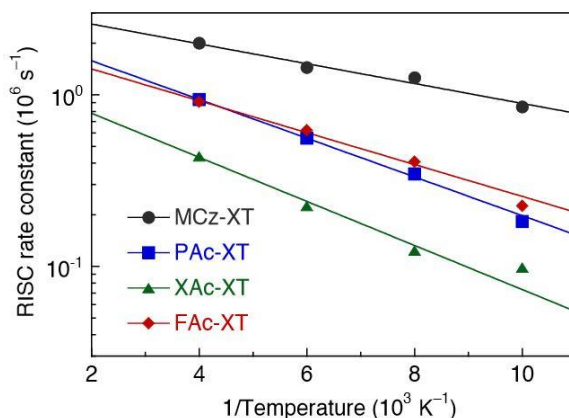
Figure 2-4. Arrhenius plots of the rate constants (k_{RISC}) of reverse intersystem crossing (RISC) for XT-based TADF molecules in a 2,8-bis(diphenylphosphoryl)dibenzo[*b,d*]furan (PPF) solid host matrix at a doping concentration of 5 wt%.

Intriguingly, despite the similar photophysical properties of these XT-based molecules in terms of PL emission wavelength (λ_{PL}), prompt-fluorescence and delayed-fluorescence lifetimes (τ_{PF} and τ_{DF}), Φ_{PL}, and ΔE_{ST}, only a small variation in the peripheral substitution pattern of the donor unit had a noticeable effect on the concentration quenching behavior of TADF (Figure 2-5). Similar to most reported TADF emitters,[1a,1b,2c–2f] MCz-XT, which contained a planar MCz donor unit, suffered from severe concentration quenching. In this case, Φ_{PL} of MCz-XT was as high as 98.0% at a doping concentration of 5 wt% in a PPF solid host

matrix; however, it decreased to 49.8% in a 100 wt% neat film (Figure 2-5). In contrast, PAc-XT, XAc-XT, and FAc-XT, which had non-planar spiro-acridan-based donor units, exhibited minimal concentration quenching and remarkable insensitivity of Φ_{PL} to doping concentrations in the range of 5–100 wt% in the thin films. The values of Φ_{PL} of PAc-XT, XAc-XT, and FAc-XT decreased by 6.8–15% as the doping concentration was increased from 5 to 100 wt%, retaining high Φ_{PL} values of 92.0%, 83.5%, and 81.5%, respectively, even in the 100 wt% neat film.

Table 2-2. Photophysical properties of TADF molecules embedded in a solid host matrix

Emitter	$\lambda_{PL}{}^a$ (nm)	$\tau_{PF}{}^b$ (ns)	$\tau_{DF}{}^c$ (µs)	$\Phi_{PL}{}^d$ (%)	$\Phi_{PF}{}^e$ (%)	$\Phi_{DF}{}^f$ (%)	$\Delta E_{ST}{}^g$ (meV)
MCz-XT	478	33.3	1.20	98.0	41.5	56.6	11
PAc-XT	482	35.0	2.25	98.8	44.5	54.3	22
XAc-XT	481	22.7	5.31	95.0	43.2	51.8	25
FAc-XT	488	23.0	1.98	97.0	47.6	49.4	18

[a]Maximum wavelength of PL spectra measured in a PPF solid host matrix at a doping concentration of 5 wt% [b]Lifetime of prompt fluorescence. [c] Lifetime of delayed fluorescence. [d]Overall PL quantum efficiency. [e]Fractional contribution of prompt fluorescence to Φ_{PL}. [f]Fractional contribution of delayed fluorescence to Φ_{PL}. [g]Singlet–triplet energy splitting determined from Arrhenius plot of the rate constants of RISC in Figure 2-4.
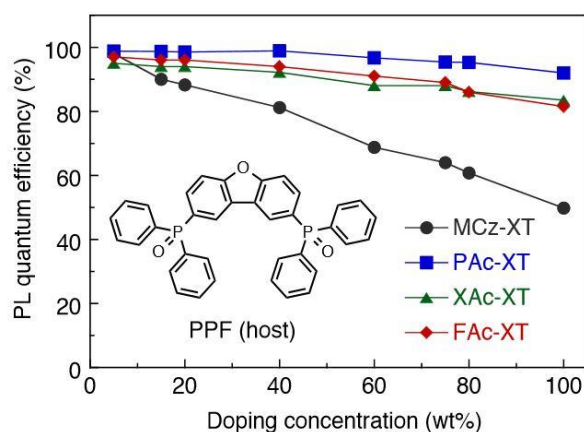
Figure 2-5. PL quantum efficiencies of the XT-based TADF molecules in a PPF solid host matrix with different doping concentrations (5−100 wt%); the inset shows the molecular structure of PPF.

2. 4 Electroluminescence Performance

The impact of concentration quenching on EL performance is evident in a comparison of TADF OLEDs with heavily doped emission layers (Figure 2-6). The OLEDs were composed of the following multiple layers: indium tin oxide (ITO, 100 nm)/4,4′-bis[*N*-(1-naphthyl)-*N*-

phenylamino]-1,1′-biphenyl (α-NPD, 40 nm)/1,3-bis(9-carbazolyl)benzene (mCP, 10 nm)/75 wt% TADF emitter in PPF (20 nm)/PPF (10 nm)/1,3,5-tris(*N*-phenylbenzimidazol-2-yl)benzene (TPBi, 30 nm)/LiF (0.8 nm)/Al (80 nm). The EL spectra of all devices with XT-based TADF emitters coincided with the corresponding PL spectra (Figure 2-6a), and the devices showed similar current density–voltage (*J–V*) characteristics with turn-on voltages of 3.3–3.6 V (Figure 2-6b). These results indicate that the electro-generated excitons were well confined within the emission layer to generate EL from the XT-based TADF emitters. It is noteworthy that the devices using PAc-XT, XAc-XT, and FAc-XT at a high doping concentration (75 wt%) exhibited significantly enhanced maximum external EL quantum efficiencies (η_{ext}) of 16.5%, 18.8%, and 17.3%, respectively, without special light-outcoupling enhancements (Figure 2-6c and Table 2-3). In contrast, a relatively low η_{ext} of 7.6% was obtained for the MCz-XT-based device. In addition, the considerably short lifetimes of TADF (τ_{DF}) contributed to the improvement of η_{ext} and efficiency roll-off characteristics of the devices at high luminance. For the TADF OLEDs incorporating PAc-XT, XAc-XT, and FAc-XT at a doping concentration of 75 wt%, the η_{ext} values remained as high as 16.3–18.8% at 100 cd m^{-2} for displays and 12.9–17.4% at 1000 cd m^{-2} for lighting applications (Table 2-3). Owing to their high Φ_{PL} at high doping concentrations and the short excited-state lifetimes, PAc-XT, XAc-XT, and FAc-XT could also be applied to construct non-doped TADF OLEDs without using an additional host material, demonstrating η_{ext} values of up to 11.2%, 14.1% and 12.6%, respectively (Figure 2-7).

Table 2-3. Device performances of TADF OLEDs

Emitter	Doping conc. (wt%)	$\lambda_{EL}{}^a$ (nm)	$V_{on}{}^b$ (V)	η_{ext} (%)		
				Maximum	at 100 cd m^{-2}	at 1000 cd m^{-2}
MCz-XT	15	485	3.7	11.1	10.2	8.5
	75	494	3.6	7.6	7.1	5.1
	100	488	3.9	5.2	4.6	2.2
PAc-XT	15	488	3.6	18.3	15.5	11.5
	75	488	3.3	16.5	16.3	12.9
	100	488	3.5	11.2	9.4	5.9
XAc-XT	15	484	3.8	20.1	18.2	15.7
	75	492	3.5	18.8	18.8	17.4
	100	488	3.8	14.1	12.7	10.5
FAc-XT	15	493	3.6	19.6	16.9	14.4
	75	500	3.3	17.3	17.3	15.9
	100	497	3.6	12.6	11.9	9.5

^{a} Maximum EL wavelength. ^{b} Turn-on voltage at 1 cd m^{-2}.

(a)

(b)

(c)
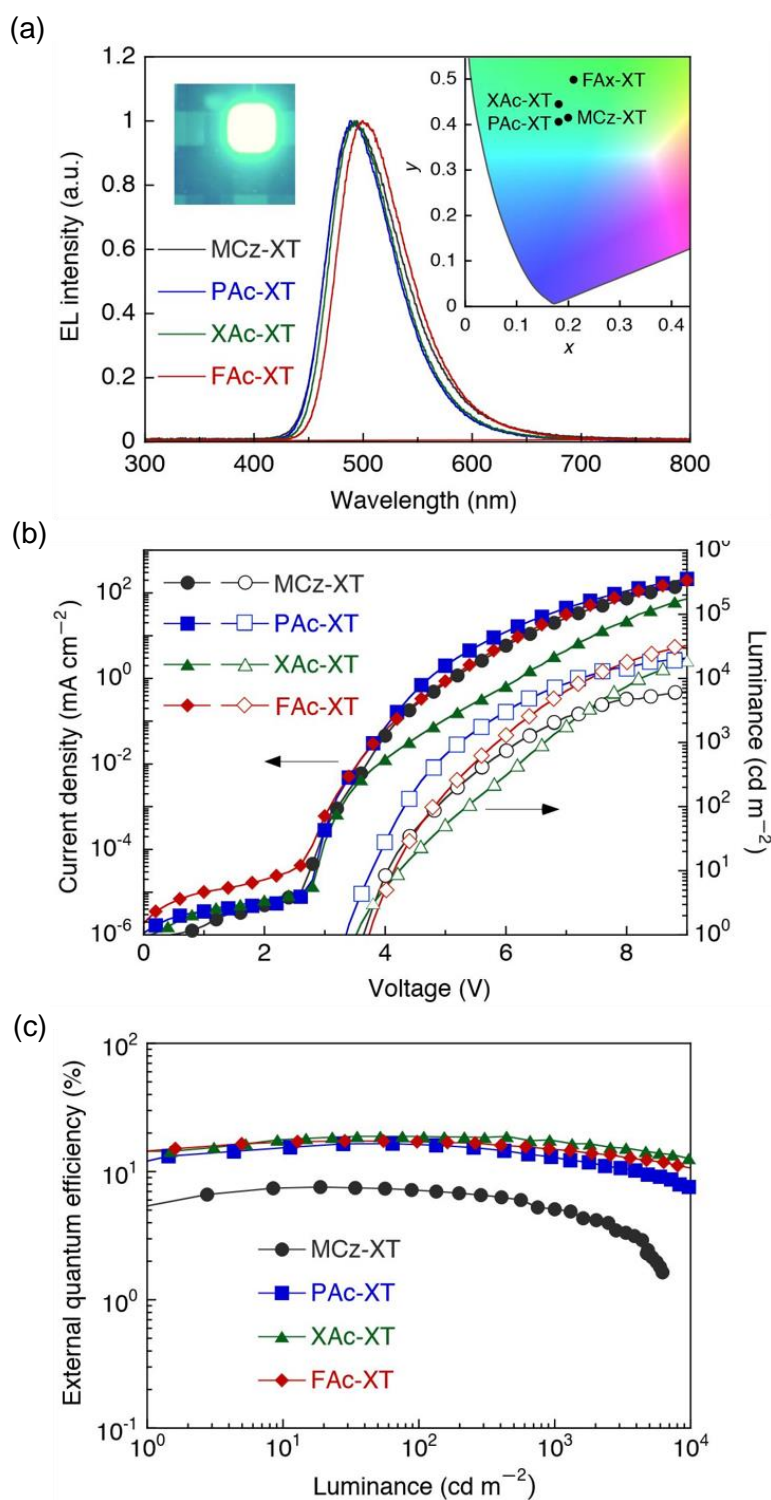
Figure 2-6. (a) EL spectra of TADF OLEDs based on heavily doped (75 wt%) emission layers, measured at 10 mA cm^{-2}; the insets show a photograph of light-blue EL emission from an MCz-XT-based device and EL colour coordinates on the Commission Internationale de l´Eclairage (CIE) 1931 chromaticity diagram. (b) Current-density–voltage–luminance (*J–V–L*) characteristics and (c) external-quantum-efficiency–luminance (η_{ext}–*L*) characteristics of the TADF OLEDs.
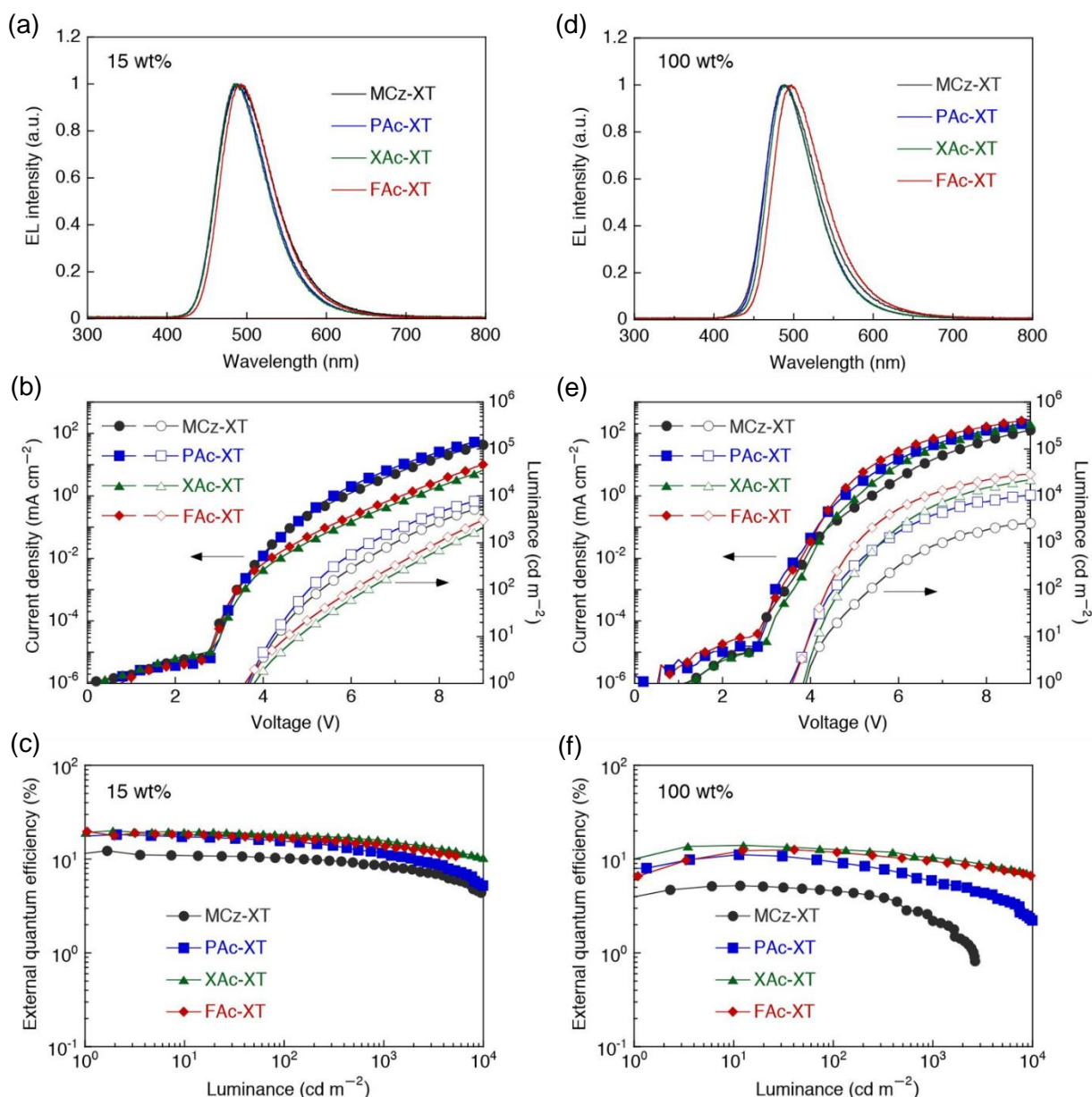
Figure 2-7. (a–c) Performance of TADF OLEDs based on 15 wt%-doped emission layers and (d–f) non-doped neat (100 wt%) emission layers measured at 10 mA cm^{-2}, including (a, d) EL spectra, (b, e) current density–voltage–luminance (*J–V–L*) characteristics, and (c, f) η_{ext}–*L* characteristics.

2. 5 Mechanistic Study on Concentration Quenching of TADF

It is worth noting that the concentration quenching of both PL and EL was effectively inhibited in PAc-XT, XAc-XT, and FAc-XT, despite minor structural differences in the molecules compared to MCz-XT in the terminal substituents appended via an sp3-hybridised carbon atom in the acridan donor units. Reflecting their ICT characteristics, these four XT-based TADF molecules showed large Stokes shifts of 3960–4890 cm^{-1} and small spectral

overlap integrals of 1.6×10^8 to 9.8×10^9 nm^4 M^{-1} cm^{-1} between the lowest-energy absorption and the corresponding emission (Table 2-4). Thus, the corresponding Förster radii (that is, critical intermolecular distances, within which the Förster resonance energy transfer and spontaneous fluorescence were equally probable) were calculated to be 0.4–0.9 nm, which are one order of magnitude smaller than those observed in typical fluorescent and phosphorescent molecules (approximately 2−10 nm).[4a] This observation indicates that the Förster resonance energy transfer of the singlet excitons was not feasible, and hence played a negligible role in the concentration quenching in these TADF systems.

As evidenced by the transient PL decay measurements (Figure 2-8a and Table 2-5), τ_{PF} of MCz-XT remained unchanged at 33 ns as the doping concentration was varied in the range of 5–100 wt%. However, τ_{DF} decreased monotonically with increasing doping concentration of MCz-XT, suggesting that non-radiative quenching pathways for the triplet excitons, which competed with RISC, were formed in the heavily doped or neat films of MCz-XT.

Table 2-4. Spectral overlap integrals and Förster radii of the XT-based TADF emitters and Ir(ppy)₃ in 1.0×10^{-5} M toluene solutions

Emitter	J^a (nm^4 M^{-1} cm^{-1})	$R_F{}^b$ (nm)
MCz-XT	1.6×10^8	0.46
PAc-XT	1.6×10^9	0.67
XAc-XT	5.3×10^9	0.82
FAc-XT	9.8×10^9	0.90
Ir(ppy)₃	6.4×10^{12}	2.7

^{a} Spectral overlap integral between the lowest-energy absorption and the corresponding emission. ^{b} Förster radius estimated from J by assuming that the orientation factor (κ^2) is 2/3 and the refractive index is 1.8.

To gain further insight into the quenching mechanism of triplet excitons, we examined the rate constant of concentration quenching (k_{CQ}) as a function of average intermolecular distance (R) in the thin films. Assuming that k_{RISC} was independent of the concentration of the TADF emitters, k_{CQ} could be experimentally determined using equation (2-2):

$$k_{CQ} = \frac{1}{2}\left(k_{PF} + k_{DF} - 2k_{RISC} - \sqrt{(k_{PF} - k_{DF})^2 - 4k_{ISC}k_{RISC}}\right) \tag{2-2}$$

The values of R were estimated from the inverse cube root of the molecular film densities,[4a] which were derived from the critical angles of the total external reflection by X-ray reflectometry (XRR) measurements. As depicted in Figure 2-8e, k_{CQ} of MCz-XT showed an

exponential dependence on R, which agrees well with the Dexter energy-transfer model.[10,11] Thus, k_{CQ} can be expressed as follows:

$$k_{CQ}(R) = k_{RISC} \exp\left\{\frac{2R_0}{L_{ET}}\left(1 - \frac{R}{R_0}\right)\right\} \tag{2-3}$$

where R_0 is the critical intermolecular distance, at which the concentration quenching and RISC occurred with the same probability, and L_{ET} is the effective electron tunneling distance, which quantifies the intermolecular electron-exchange interactions. The best-fit parameters that properly describe the $k_{CQ}-R$ plots for the MCz-XT films are R_0 of 0.40 nm and L_{ET} of 0.68 nm.

Table 2-5. Photophysical properties of the XT-based TADF emitters in a PPF host matrix at doping concentrations of 5−100 wt%

Emitter	Doping conc. (wt%)	τ_{PF} (ns)	τ_{DF} (μs)	Φ_{PL} (%)	Φ_{PF} (%)	Φ_{DF} (%)	k_{PF} (10^7 s^{-1})	k_{DF} (10^5 s^{-1})	k_{ISC}[a] (10^7 s^{-1})	k_{RISC}[b] (10^3 s^{-1})	k_{CQ}[c] (10^3 s^{-1})
MCz-XT	5	33.3	1.20	98.0	41.4	56.6	3.00	8.34	1.79	22.8	~0
	20	33.3	0.991	90.4	44.3	46.1	3.00	10.1	1.67	–	108
	40	33.3	0.926	74.2	41.6	32.6	3.00	10.8	1.75	–	254
	60	33.3	0.873	61.0	39.6	21.4	3.00	11.5	1.81	–	374
	80	33.3	0.807	52.3	39.0	13.3	3.00	12.4	1.81	–	492
	100	33.3	0.700	49.8	41.8	8.0	3.00	14.3	1.75	–	618
PAc-XT	5	35.0	2.25	98.8	44.5	54.3	2.86	4.44	1.59	10.5	~0
	20	35.0	2.24	98.6	44.6	54.0	2.86	4.46	1.58	–	1.11
	40	35.0	2.23	97.6	44.5	53.1	2.86	4.48	1.59	–	4.44
	60	35.0	2.20	96.0	44.2	51.8	2.86	4.55	1.59	–	14.1
	80	35.0	2.18	93.7	43.0	50.7	2.86	4.59	1.63	–	30.6
	100	35.0	2.10	92.0	43.0	49.0	2.86	4.76	1.63	–	49.0
XAc-XT	5	22.7	5.31	95.0	43.2	51.8	4.41	1.88	2.50	4.41	~0
	20	22.7	5.11	94.0	44.4	49.6	4.41	1.96	2.45	–	2.21
	40	22.7	4.89	92.2	44.0	48.2	4.41	2.04	2.47	–	12.8
	60	22.7	4.68	88.5	41.9	46.6	4.41	2.14	2.56	–	31.4
	80	22.7	4.35	86.2	40.1	46.1	4.41	2.30	2.64	–	56.0
	100	22.7	3.80	83.5	40.9	42.6	4.41	2.63	2.60	–	85.8
FAc-XT	5	23.0	1.98	97.0	47.6	49.4	4.35	5.06	2.28	10.9	~0
	20	23.0	1.91	96.5	48.0	48.5	4.35	5.24	2.26	–	12.6
	40	23.0	1.75	94.0	48.9	45.1	4.35	5.70	2.22	–	50.4
	60	23.0	1.61	91.0	49.2	41.8	4.35	6.20	2.21	–	97.1
	80	23.0	1.50	86.0	48.0	38.0	4.35	6.66	2.26	–	157
	100	23.0	1.44	81.5	46.4	35.1	4.35	6.96	2.33	–	206

[a] Rate constant of ISC, estimated using equation (2-9). [b] Rate constant of RISC, estimated using equation (2-1). [c] Rate constant of the concentration quenching of triplet exciton, estimated using equation (2-2).
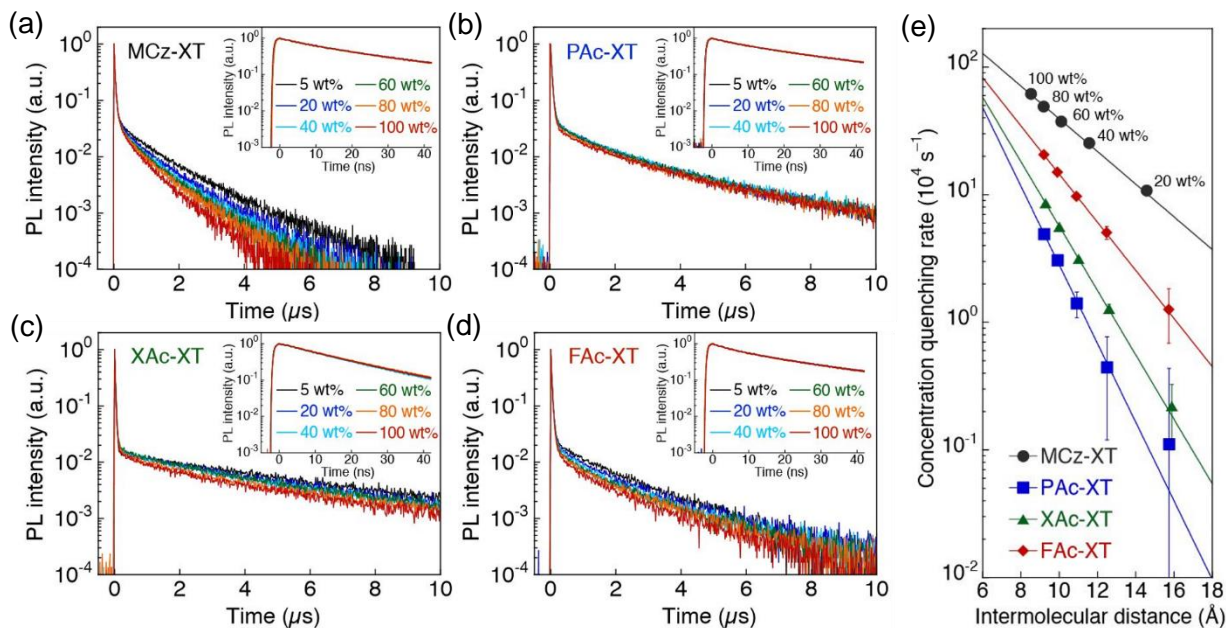
Figure 2-8. Transient PL decay curves of (a) MCz-XT, (b) PAc-XT, (c) XAc-XT, and (d) FAc-XT in a PPF solid host matrix at different doping concentrations (5−100 wt%) within a time period of micro- and nanoseconds (insets). (e) Rate constants of concentration quenching (k_{CQ}) of the XT-based TADF molecules as functions of average intermolecular distance. The solid lines are fits of the plots using the Dexter model.

This L_{ET} value is much larger than the close intermolecular distance (0.35 nm) of MCz-XT in a single crystal (Figure 2-9). The collected set of experimental results therefore demonstrated that a large fraction of the triplet excitons formed in MCz-XT diffused and were quenched through the electron-exchange interactions between the nearby MCz-XT molecules. Menke and coworkers recently reported that Dexter energy transfer is also responsible for exciton diffusion in thin films of a typical TADF emitter, 1,2,3,5-tetrakis(carbazol-9-yl)-4,6-dicyanobenzene (4CzIPN) with an attenuation coefficient b of 0.08 Å^{-1},[12] which corresponds to L_{ET} of 2.5 nm. The ability of the spiro-acridan-containing molecules, PAc-XT, XAc-XT, and FAc-XT, to yield high PL and EL quantum efficiencies is ascribed to the inhibition of the intermolecular electron-exchange interactions in their condensed solid states. In fact, significantly reduced L_{ET} values of 0.28, 0.34 and 0.46 nm were estimated from equation (3) for PAc-XT, XAc-XT, and FAc-XT, respectively. Density functional theory (DFT) calculations for the lowest excited triplet states of these XT-based TADF molecules revealed that the spin-density distributions resided on the D–A molecular structures except for the terminal substituents appended to the sp3-hybridised carbon atom of the acridan donor units (Figure 2-9b and Figure 2-10). In contrast, the triplet spin density of MCz-XT containing a planar MCz donor unit was distributed over the entire molecule. Given the major role of short-range Dexter energy transfer in these TADF

30

molecules, it is reasonable to conclude that such insulating substituents could effectively suppress the intermolecular electron-exchange interactions and thus concentration quenching.

Figure 2-9. Calculated spin-density distributions of the lowest-excited triplet states of (a) MCz-XT and (b) PAc-XT in the solid-state geometry determined by single-crystal X-ray analysis. The isovalue is 0.0004.

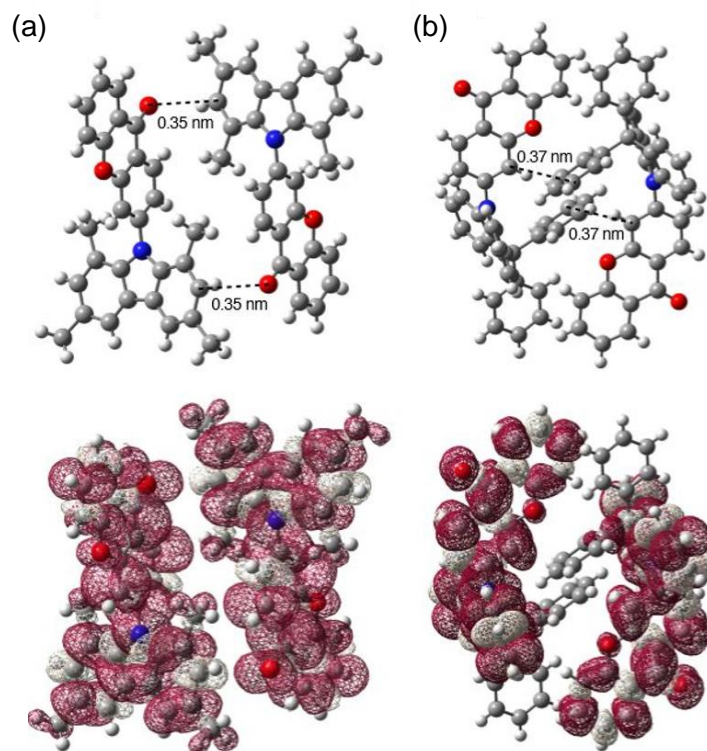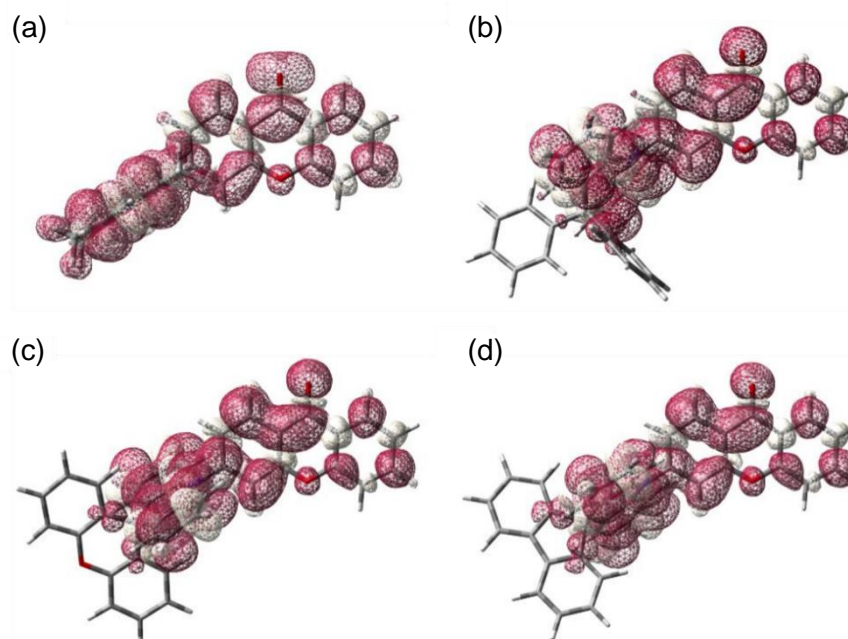**Figure 2-10.** Calculated spin density distributions of the lowest excited triplet states of (a) MCz-XT, (b) PAc-XT, (c) XAc-XT, and (d) FAc-XT. The isovalue is 0.0004.

2. 6 Conclusion

The author has revealed that concentration quenching of TADF molecules examined in this study was dominated by electron-exchange interactions for triplet excitons, as described by the Dexter energy-transfer model. This result is in marked contrast to conventional fluorescent and phosphorescent molecules involving the Förster energy-transfer mechanism. Owing to the short-range nature of electron-exchange interactions, even a small modulation in molecular geometric structure could drastically affect the concentration-quenching behavior, leading to enhanced PL and EL properties. A concept and strategy for inhibiting the concentration quenching of TADF would provide critical guidelines for the design of future high-performance purely organic TADF emitters and devices.

2. 7 Experimental Section

2. 7. 1 Materials and Synthesis

Commercially available reagents and solvents were used without further purification unless otherwise noted. All of the reactions were performed under a nitrogen atmosphere in dry solvents using standard Schlenk techniques. First, 3-bromo-9*H*-xanthen-9-one,[8] 10*H*-spiro[acridan-9,9′-fluorene],[2h] 10*H*-spiro[acridan-9,9′-xanthene][2h] and 1,3,6,8-tetramethyl-9*H*-carbazole[2h] were prepared according to procedures described in the literature; 9,9-diphenylacridan was prepared according to a procedure that was modified from the method reported in the literature[14]. High-performance liquid chromatography was performed using TSKgel ODS-120A (Tosoh). NMR spectra were recorded on an Avance III 500 spectrometer (Bruker). Chemical shifts of ^{1}H and ^{13}C NMR signals were determined relative to the signals of tetramethylsilane ($\delta = 0.00$), CDCl$_3$ ($\delta = 77.0$) and DMSO-d_6 ($\delta = 39.5$) as internal standards. Matrix-assisted laser desorption ionization time-of-flight (MALDI-TOF) mass spectra were collected on an Autoflex III spectrometer (Bruker Daltonics) using dithranol as a matrix. Elemental analysis was carried out with a MT-5 CHN Corder (Yanaco).

Synthesis of 9,9-diphenylacridan: Phenyllithium (PhLi; 148.5 mL, 237.6 mmol) was added dropwise at –78 °C to a solution of methyl-2-(phenylamino)benzene (18.0 g, 79.2 mmol) in dry tetrahydrofuran (THF; 300 mL). The mixture was stirred for 1 h at –78 °C and then left to further react for 2 h at 0 °C. The mixture was than heated to room temperature and stirred for 4 h, after which it was quenched by the addition of a large amount of water. The reaction mixture was extracted with chloroform and dried over anhydrous sodium sulfate. After filtration and

evaporation, the crude product was used in the next reaction without further purification. Methanesulfonic acid (MeSO₃H; 8.37 g, 87.1 mmol) was added at room temperature to a solution of the crude product in dry chloroform (300 mL).
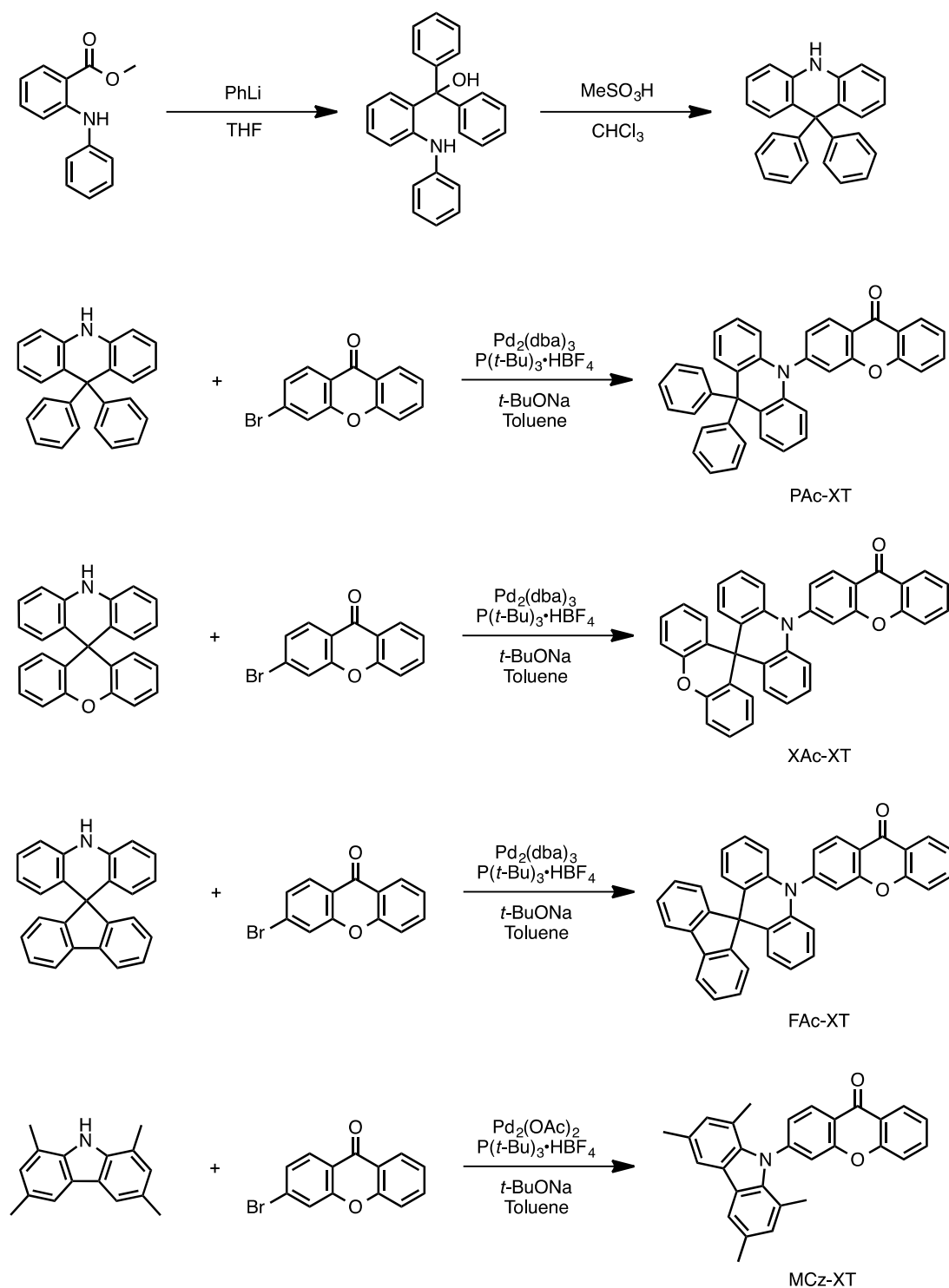
Scheme 2-1. Synthetic routes for 9,9-diphenylacridan, PAc-XT, XAc-XT, FAc-XT, and MCz-XT.

The mixture was refluxed for 1 h, and then left to further react for 12 h at room temperature. The reaction mixture was concentrated under reduced pressure. The product was purified by silica-gel column chromatography (eluent: *n*-hexane/chloroform = 3:1, v/v) to afford 9,9-diphenylacridan as a white solid (18.5 g, 70%). ^{1}H NMR (500 MHz, CDCl$_3$): δ 7.26–7.15 (m, 8H), 6.96–6.94 (m, 4H), 6.89 (td, *J* = 7.5 Hz, 1.2 Hz, 2H), 6.83 (dd, *J* = 7.8 Hz, 1.5 Hz, 2H), 6.80 (dd, *J* = 7.9 Hz, 1.1 Hz, 2H), 6.28 (s, 1H).

Synthesis of PAc-XT: Tris(dibenzylideneacetone)dipalladium(0) (Pd$_2$(dba)$_3$; 0.18 g, 0.20 mmol), tri-*tert*-butylphosphonium tetrafluoroborate (P(*t*-Bu)$_3$·HBF$_4$; 0.23 g, 0.79 mmol), and sodium *tert*-butoxide (*t*-BuONa; 1.92 g, 20.0 mmol) were added to a mixture of 3-bromoxanthone (2.75 g, 10.0 mmol) and 9,9-diphenylacridan (3.67 g, 11.0 mmol) in dry toluene (50 mL). The mixture was refluxed for 18 h. After cooling to room temperature, the reaction mixture was filtered through a Celite pad, and the filtrate was concentrated under reduced pressure. The product was purified by silica-gel column chromatography (eluent: dichloromethane), recrystallized from dichloromethane/ethyl acetate, and dried under vacuum to afford PAc-XT as a yellow solid (4.85 g, 92%). This compound was further purified by temperature-gradient sublimation under vacuum (<5 × 10^{-3} Pa) before use. ^{1}H NMR (500 MHz, DMSO-d_6): δ 8.30 (d, *J* = 8.5 Hz, 1H), 8.23 (dd, *J* = 8.0 Hz, 1.7 Hz, 1H), 7.90 (td, *J* = 7.8 Hz, 1.7 Hz, 1H), 7.67 (d, *J* = 8.0 Hz, 1H), 7.52 (td, *J* = 7.5 Hz, 1.0 Hz, 1H), 7.37 (d, *J* = 1.9 Hz, 1H), 7.34–7.31 (m, 4H), 7.29–7.26 (m, 2H), 7.18 (td, *J* = 7.7 Hz, 1.4 Hz, 2H), 7.05–7.01 (m, 3H), 6.90 (d, *J* = 7.1 Hz, 4H), 6.83 (dd, *J* = 7.8 Hz, 1.4 Hz, 2H), 6.70 (dd, *J* = 8.2 Hz, 0.9 Hz, 2H). ^{13}C NMR (125 MHz, DMSO-d_6): δ 175.34, 156.89, 155.63, 146.85, 145.46, 140.83, 135.65, 131.52, 129.72, 129.51, 128.60, 127.85, 127.25, 126.61, 125.97, 124.59, 124.24, 121.55, 121.22, 119.94, 118.14, 117.32, 115.93, 56.47. MS (MALDI-TOF): *m/z* [*M*+H]$^+$ calcd 528.20; found, 528.31. Anal. Calcd (%) for C$_{38}$H$_{25}$NO$_2$: C, 86.50; H, 4.78; N, 2.65; found: C, 86.48; H, 4.74; N, 2.63.

Synthesis of XAc-XT: Pd$_2$(dba)$_3$ (0.08 g, 0.09 mmol), P(*t*-Bu)$_3$·HBF$_4$ (0.10 g, 0.34 mmol) and *t*-BuONa (0.85 g, 8.84 mmol) were added to a mixture of 3-bromoxanthone (1.22 g, 4.43 mmol) and 10*H*-spiro[acridine-9,9′-xanthene] (1.68 g, 4.84 mmol) in dry toluene (45 mL). The mixture was refluxed for 8 h. After cooling to room temperature, the resulting solution was poured into methanol. The precipitate was collected by filtration and washed with several portions of methanol. The product was purified by silica-gel column chromatography (eluent:

n-hexane/dichloromethane = 1:4, v/v), recrystallized from dichloromethane/ethyl acetate, and dried under vacuum to afford XAc-XT as a yellow solid (2.31 g, 96%) This compound was further purified by temperature-gradient sublimation under vacuum ($<5 \times 10^{-3}$ Pa) before use. ^{1}H NMR (500 MHz, DMSO-d_6): δ 8.58 (d, J = 8.3 Hz, 1H), 8.30 (dd, J = 8.0 Hz, 1.6 Hz, 1H), 8.07 (d, J = 1.8 Hz, 1H), 7.96 (td, J = 7.8 Hz, 1.7 Hz, 1H), 7.75 (d, J = 8.4 Hz, 1H), 7.65 (dd, J = 8.3 Hz, 1.9 Hz, 1H), 7.58 (t, J = 7.5 Hz, 1H), 7.27–7.23 (m, 4H), 7.17 (dd, J = 7.8 Hz, 1.3 Hz 2H), 7.07–7.03 (m, 2H), 6.95–6.92 (m, 2H), 6.75–6.72 (m, 4H), 6.31 (d, J = 8.4 Hz, 2H). ^{13}C NMR (125 MHz, DMSO-d_6): δ 175.71, 157.60, 155.75, 147.62, 146.58, 138.07, 135.89, 132.07, 131.97, 131.07, 129.49, 129.44, 127.96, 127.21, 127.02, 126.11, 124.75, 123.93, 121.35, 121.33, 121.31, 121.12, 118.26, 115.74, 114.03, 43.97. MS (MALDI-TOF): m/z $[M]^+$ calcd 541.17; found, 541.29. Anal. Calcd (%) for $C_{38}H_{23}NO_3$: C, 84.27; H, 4.28; N, 2.59; found: C, 83.99; H, 4.20; N, 2.63.

Synthesis of FAc-XT: $Pd_2(dba)_3$ (0.18 g, 0.20 mmol), P(*t*-Bu)$_3$·HBF$_4$ (0.23 g, 0.79 mmol) and *t*-BuONa (1.92 g, 20.0 mmol) were added to a mixture of 3-bromoxanthone (2.75 g, 10.0 mmol) and 10*H*-spiro[acridine-9,9′-fluorene] (3.65 g, 11.0 mmol) in dry toluene (50 mL). The mixture was refluxed for 4 h. After cooling to room temperature, the reaction mixture was filtered through a Celite pad, and the filtrate was concentrated under reduced pressure. The crude product was purified by silica-gel column chromatography (eluent: dichloromethane), recrystallized from dichloromethane/ethyl acetate, and dried under vacuum to afford FAc-XT as a yellow solid (2.19 g, 42%). This compound was further purified by temperature-gradient sublimation under vacuum ($<5 \times 10^{-3}$ Pa) before use. ^{1}H NMR (500 MHz, DMSO-d_6): δ 8.59 (d, J = 8.3 Hz, 1H), 8.31 (dd, J = 8.0 Hz, 1.7 Hz, 1H), 8.09 (d, J = 1.6 Hz, 1H), 8.00–7.95 (m, 3H), 7.75 (d, J = 8.3 Hz, 1H), 7.68 (dd, J = 8.3 Hz, 1.9 Hz, 1H), 7.58 (t, J = 7.5 Hz, 1H), 7.46–7.42 (m, 4H), 7.33 (t, J = 7.2 Hz, 2H), 6.98 (td, J = 7.8 Hz, 1.4 Hz, 2H), 6.63 (td, J = 7.5 Hz, 0.9 Hz, 2H), 6.41 (d, J = 8.3 Hz, 2H), 6.27 (dd, J = 7.8 Hz, 1.4 Hz, 2H). ^{13}C NMR (125 MHz, DMSO-d_6): δ 175.71, 157.57, 155.94, 155.76, 146.58, 140.18, 138.69, 135.89, 129.42, 128.59, 127.86, 127.54, 127.22, 126.91, 126.11, 125.52, 124.75, 124.50, 121.32, 121.28, 121.19, 120.92, 120.34, 118.26, 114.61, 56.14. MS (MALDI-TOF): m/z $[M]^+$ calcd 525.17; found, 525.12. Anal. Calcd (%) for $C_{38}H_{23}NO_2$: C, 86.84; H, 4.41; N, 2.66; found: C, 86.76; H, 4.36; N, 2.63.

Synthesis of MCz-XT: Palladium(II) acetate (Pd(OAc)$_2$; 0.05 g, 0.22 mmol), P(*t*-Bu)$_3$·HBF$_4$ (0.32 g, 1.10 mmol) and *t*-BuONa (1.71 g, 17.8 mmol) were added to a mixture of 3-

bromoxanthone (2.00 g, 7.27 mmol) and 1,3,6,8-tetramethyl-9*H*-carbazole (1.99 g, 8.91 mmol) in dry toluene (80 mL). The mixture was stirred for 18 h at 80 °C. After cooling to room temperature, the reaction mixture was poured into water and then extracted with toluene. The combined organic layers were washed with water and dried over anhydrous sodium sulfate. After filtration and evaporation, the product was purified by silica-gel column chromatography (eluent: chloroform), recrystallized from dichloromethane/methanol, and dried under vacuum to afford MCz-XT as a yellow solid (2.85 g, 94%). This compound was further purified by temperature-gradient sublimation under vacuum ($<5 \times 10^{-3}$ Pa) before use. ^{1}H NMR (500 MHz, DMSO-d_6): δ 8.30-8.26 (m, 2H), 8.02 (d, J = 1.9 Hz, 1H), 7.93 (td, J = 7.8 Hz, 1.7 Hz, 1H), 7.82 (s, 2H), 7.70 (d, J = 8.4 Hz, 1H), 7.57–7.51 (m, 2H), 6.94 (s, 2H), 2.43 (s, 6H), 1.86 (s, 6H). ^{13}C NMR (125 MHz, DMSO-d_6): δ 175.67, 155.82, 155.23, 148.05, 139.06, 135.85, 130.24, 129.00, 127.29, 126.15, 126.06, 124.76, 123.97, 121.27, 121.16, 120.86, 120.72, 118.28, 117.86, 20.72, 19.01. MS (MALDI-TOF): *m/z* $[M]^{+}$ calcd 417.17; found, 417.10. Anal. Calcd (%) for $C_{29}H_{23}NO_2$: C, 83.43; H, 5.55; N, 3.35; found: C, 83.43; H, 5.54; N, 3.32.

2. 7. 2 Quantum Chemical Calculations

All quantum chemical calculations were performed using the Gaussian 09 program package. Gas-phase geometry optimizations for the lowest excited singlet and triplet states were carried out using time-dependent density functional theory (TDDFT) calculations at the PBE0/6-31G(d) level.[27] Triplet spin-density distributions were computed using the solid-state geometry determined by single-crystal X-ray analysis at the unrestricted PBE0/6-31G(d) level.

2. 7. 3 Photophysical Characterizations

UV–vis absorption and PL spectra were measured with a UV-2550 spectrometer (Shimadzu) and a Fluoromax-4 spectrophotometer (Horiba Scientific), respectively, using spectral grade solvents. The PL quantum efficiencies were measured using an integration sphere system C9920-02 coupled with a PMA-11 photonic multichannel analyser (Hamamatsu Photonics) by photoexcitation of 340 nm. The temperature dependence of transient PL decays was measured using a C4334 Streak camera (Hamamatsu Photonics) with a N$_2$ gas laser (λ = 337 nm, pulse width = 500 ps and repetition rate = 20 Hz) under vacuum ($<4 \times 10^{-1}$ Pa). Room-temperature transient PL decay measurements were carried out using a C11367 Quantaurus-tau fluorescence lifetime spectrometer (Hamamatsu Photonics).

2. 7. 4 OLED Fabrication and Measurements

ITO-coated glass substrates were cleaned with detergent, deionized water, acetone, and isopropanol. The substrates were then subjected to UV–ozone treatment for 15 min before they were loaded into a vacuum evaporation system. The organic layers were thermally evaporated on the substrates under vacuum ($<3 \times 10^{-4}$ Pa) at an evaporation rate of <0.3 nm s^{-1}. LiF and Al layers were then deposited through a shadow mask. The layer thickness and the deposition rate were monitored *in situ* during deposition by an oscillating quartz thickness monitor. The current density–voltage–luminance characteristics of the devices were measured using a source meter (Keithley 2400, Keithley Instruments Inc.) and an absolute external quantum efficiency measurement system (C9920-12, Hamamatsu Photonics). The OLEDs were mounted to the entrance port of the measurement system's integrating sphere to collect the photons emitted from the front face of the devices. EL spectra were collected by an optical fiber connected to a spectrometer (PMA-12, Hamamatsu Photonics).

2. 7. 5 X-Ray Reflectometry Measurements

In the x-ray region, the complex refractive index (n_r), which is slightly smaller than 1, is expressed by following the equation

$$n_r = 1 - \delta + i\beta \tag{2-4}$$

where δ and β are the dispersion and absorption, respectively. Reflection was considered at an interface between air ($n_{air} = 1$) and another material ($n_1 = 1 - \delta$). Total reflection for incident angles below a critical angle (θ_C, $\theta < \theta_C$) occurs. Thus, the critical angle can be estimated by following equations, in accordance with Snell's law and small angle approximations,

$$1 - \delta = \cos\theta_C \approx 1 - \frac{\theta_C^2}{2}$$
$$\Leftrightarrow \theta_C \propto \sqrt{\rho} \tag{2-5}$$

Therefore, a density of a material (ρ) can be determined by a critical angle from a fitted curve using an experimental result.

Critical angles of the organic films exhibit a smaller angle than that of the Si substrate due to the lower densities of organic materials than those of Si substrates. In case of the thin organic film, the critical angle in the XRR patterns tends to be blurred. Thus, doped films for xanthone-based materials in a PPF host matrix with a large thickness of about 300 nm were fabricated on Si(100) substrates to obtain clearly apparent critical angles.[15]

XRR patterns were measured using a SmartLab diffractometer (Rigaku) using Cu K_α radiation ($\lambda = 0.15418$ nm) at 45 kV and 200 mA. The divergence angle of a beam was 0.01°, and the incident angles were scanned in the range of 0°–0.5° in steps of 0.01°. Only critical angles were employed for molecular film densities because the fringing patterns of XRR patterns for organic films have tendency to be affected by density, thickness, and surface roughness. The film densities were estimated from the critical angles for the total external reflection of the organic layers. Curve fitting and calculations were performed using the GlobalFit program package from Rigaku. The average intermolecular distances were estimated from the inverse cube root of the molecular film densities.[4a] As examplified in Figure 2-11, the average intermolecular distances of MCz-XT in a neat film was estimated to be 8.3 Å from a theoretical curve for the molecular film density of 1.21 g cm^{-3} using the critical angle.
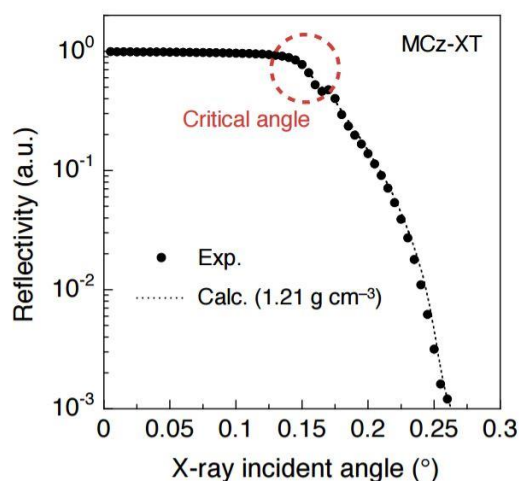
Figure 2-11. XRR pattern of MCz-XT in the neat film with a thickness of 300 nm.

2. 7. 6 Analysis of Nonradiative Rate Constants

The rate equation for singlet and triplet exciton densities (S_1 and T_1) is described by

$$\frac{d}{dt}\begin{pmatrix} S_1 \\ T_1 \end{pmatrix} = \begin{pmatrix} -(k_r^S + k_{nr}^S + k_{ISC}) & k_{RISC} \\ k_{ISC} & -(k_r^T + k_{nr}^T + k_{RISC} + k_{CQ}) \end{pmatrix}\begin{pmatrix} S_1 \\ T_1 \end{pmatrix} \tag{2-6}$$

where k_r^S, k_{nr}^S, and k_{ISC} are the rate constants of radiative decay (fluorescence), intrinsic non-radiative decay (internal conversion) and ISC for the singlet excitons, respectively. k_r^T, k_{nr}^T, k_{RISC}, and k_{CQ} are the rate constants of radiative decay (phosphorescence), intrinsic non-radiative decay, RISC and concentration quenching of the triplet exciton, respectively. The solution of equation (2-6) is given by

$$S_1, T_1 = A_1 \exp[-k_{PF}t] + A_2 \exp[-k_{DF}t] \tag{2-7}$$

where A_1 and A_2 are the intensities of the prompt and delayed fluorescence, respectively. The measurable decay rates of prompt and delayed fluorescence (k_{PF} and k_{DF}) are thus given by

$$\{(k_r^S + k_{nr}^S + k_{ISC}) - k_{PF}\}\{(k_r^T + k_{nr}^T + k_{RISC} + k_{CQ}) - k_{PF}\} - k_{ISC}k_{RISC} = 0 \tag{2-8}$$

$$\{(k_r^S + k_{nr}^S + k_{ISC}) - k_{DF}\}\{(k_r^T + k_{nr}^T + k_{RISC} + k_{CQ}) - k_{DF}\} - k_{ISC}k_{RISC} = 0 \tag{2-9}$$

Subtracting and adding equations (2-8) and (2-9) yield

$$k_{PF} + k_{DF} = k_r^S + k_{nr}^S + k_{ISC} + k_r^T + k_{nr}^T + k_{RISC} + k_{CQ} \tag{2-10}$$

$$k_{PF}k_{DF} = (k_r^S + k_{nr}^S + k_{ISC})(k_r^T + k_{nr}^T + k_{RISC} + k_{CQ}) - k_{ISC}k_{RISC} \tag{2-11}$$

The PL quantum efficiency of prompt fluorescence (Φ_{PF}) is expressed by

$$\Phi_{PF} = \frac{k_r^S}{k_r^S + k_{nr}^S + k_{ISC}} \tag{2-12}$$

By assuming (i) $k_{PF} \gg k_{DF}$, (ii) $k_r^S \gg k_{nr}^S$, k_{RISC} and (iii) $k_{RISC} \gg k_r^T$, k_{nr}^T, k_{CQ}, equations (2-10), (2-11), and (2-12) can be simplified to

$$k_{PF} \approx k_r^S + k_{ISC} \tag{2-13}$$

$$k_{PF}k_{DF} \approx k_r^S k_{RISC} \tag{2-14}$$

$$\Phi_{PF} \approx \frac{k_r^S}{k_r^S + k_{ISC}} = \frac{k_r^S}{k_{PF}} \tag{2-15}$$

Solving equations (2-13), (2-14), and (2-15) for k_{ISC} yields

$$k_{ISC} \approx k_{PF} - k_r^S = k_{PF}(1 - \Phi_{PF}) \tag{2-16}$$

Solving equations (2-13) and (2-14) for k_{RISC} yields

$$k_{RISC} \approx \frac{k_{PF}k_{DF}}{k_{PF} - k_{ISC}} \tag{2-1}$$

k_{ISC} and k_{RISC} were estimated from equations (2-16) and (2-1) for a doping concentration of 5

wt%, at which the above assumption seems valid.

When the concentration quenching of the triplet excitons is significant and the assumptions of $k_{PF} \gg k_{DF}$ and $k_{RISC} \gg k_{CQ}$ is not fulfilled, equations (2-10) and (2-11) can be simplified to

$$k_{PF} + k_{DF} \approx k_r^S + k_{ISC} + k_{RISC} + k_{CQ} \tag{2-17}$$

$$k_{PF}k_{DF} \approx k_r^S k_{RISC} + k_r^S k_{CQ} + k_{ISC}k_{CQ} \tag{2-18}$$

Solving equation (2-17) and (2-18) for k_{CQ} yields

$$k_{CQ} \approx \frac{1}{2}\left(k_{PF} + k_{DF} - 2k_{RISC} \pm \sqrt{(k_{PF} - k_{DF})^2 - 4k_{ISC}k_{RISC}}\right) \tag{2-2}$$

Assuming that k_{RISC} for a doping concentration of 5 wt% was concentration-independent, k_{CQ} values for doping concentrations of 20–100 wt% were estimated to be 10^3–10^5 s^{-1} from equation (2-2). The other solution yielded unreasonable values over 10^7 s^{-1}.

References

[1]   a) M. A. Baldo, D. O'brien, Y. You, A. Shoustikov, S. Sibley, M. Thompson, S. Forrest, *Nature* **1998**, *395* 151; b) S. J. Su, E. Gonmori, H. Sasabe, J. Kido, *Adv. Mater.* **2008**, *20*, 4189; c) S. Reineke, F. Lindner, G. Schwartz, N. Seidler, K. Walzer, B. Lüssem, K. Leo, *Nature* **2009**, *459*, 234; d) S. Y. Kim, W. I. Jeong, C. Mayr, Y. S. Park, K. H. Kim, J. H. Lee, C. K. Moon, W. Brütting, J. J. Kim, *Adv. Funct. Mater.* **2013**, *23*, 3896; e) Y. Zhang, J. Lee, S. R. Forrest, *Nat. Commun.* **2014**, *5*, 5008; f) J. Lee, H.-F. Chen, T. Batagoda, C. Coburn, P. I. Djurovich, M. E. Thompson, S. R. Forrest, *Nat. Mater.* **2016**, *15*, 92.

[2]   a) A. Endo, K. Sato, K. Yoshimura, T. Kai, A. Kawada, H. Miyazaki, C. Adachi, *Appl. Phys. Lett.* **2011**, *98*, 083302; b) H. Uoyama, K. Goushi, K. Shizu, H. Nomura, C. Adachi, *Nature* **2012**, *492*, 234; c) F. B. Dias, K. N. Bourdakos, V. Jankus, K. C. Moss, K. T. Kamtekar, V. Bhalla, J. Santos, M. R. Bryce, A. P. Monkman, *Adv. Mater.* **2013**, *25*, 3707; d) Q. Zhang, B. Li, S. Huang, H. Nomura, H. Tanaka, C. Adachi, *Nat. Photon.* **2014**, *8*, 326; e) S. Hirata, Y. Sakai, K. Masui, H. Tanaka, S. Y. Lee, H. Nomura, N. Nakamura, M. Yasumatsu, H. Nakanotani, Q. Zhang, K. Shizu, H. Miyazaki, C. Adachi, *Nat. Mater.* **2015**, *14*, 330; f) H. Kaji, H. Suzuki, T. Fukushima, K. Shizu, K. Suzuki, S. Kubo, T. Komino, H. Oiwa, F. Suzuki, A. Wakamiya, *Nat. Commun.* **2015**, *6*, 8476; g) Q. Zhang, D. Tsang, H. Kuwabara, Y. Hatae, B. Li, T. Takahashi, S. Y. Lee, T. Yasuda, C. Adachi, *Adv. Mater.* **2015**, *27*, 2096; h) M. Numata, T. Yasuda, C. Adachi, *Chem. Commun.* **2015**, *51*, 9443; i) S. Y. Lee, T. Yasuda, Y. S. Yang, Q. Zhang, C. Adachi, *Angew. Chem. Int. Ed.* **2014**, *126*, 6520.

[3]   H. Kuhn, *J. Chem. Phys.* **1970**, *53*, 101.

[4]   a) Y. Kawamura, J. Brooks, J. J. Brown, H. Sasabe, C. Adachi, *Phys. Rev. Lett.* **2006**, *96*, 017404; b) J. Ribierre, A. Ruseckas, K. Knights, S. Staton, N. Cumpstey, P. Burn, I. Samuel, *Phys. Rev. Lett.* **2008**, *100*, 017402.

[5]   a) M. A. Baldo, C. Adachi, S. R. Forrest, *Phys. Rev. B* **2000**, *62*, 10967; b) W. Staroske, M. Pfeiffer, K. Leo, M. Hoffmann, *Phys. Rev. Lett.* **2007**, *98*, 197402.

[6]   P. A. Vecchi, A. B. Padmaperuma, H. Qiao, L. S. Sapochak, P. E. Burrows, *Org. Lett.* **2006**, *8*, 4211.

[7]   K. Goushi, K. Yoshida, K. Sato, C. Adachi, *Nat. Photon.* **2012**, *6*, 253.

[8]   H. Nakanotani, T. Higuchi, T. Furukawa, K. Masui, K. Morimoto, M. Numata, H. Tanaka, Y. Sagara, T. Yasuda, C. Adachi, *Nat. Commun*. **2014**, *5*, 4016.

[9]   C. M. Marian, *J. Phys. Chem. C*, **2016**, *120*, 3715.

[10]   D. L. Dexter, *J. Chem. Phys.* **1953**, *21*, 836.

[11]   A. Ito, T. J. Meyer, *Phys. Chem. Chem. Phys.* **2012**, *14*, 13731.

[12]   S. M. Menke, R. J. Holmes, *J. Phys. Chem. C* **2016**, *120*, 8502.

[13]   X. Y. Liu, F. Liang, L. S. Cui, X. D. Yuan, Z. Q. Jiang, L. S. Liao, *Chem. Asian J.* **2015**, *10*, 1402.

[14]   C. Adamo, V. Barone, *J. Chem. Phys.* **1999**, *110*, 6158.

[15]   M. Shibata, Y. Sakai, D. Yokoyama, *J. Mater. Chem. C* **2015**, *3*, 11178.

Chapter 3

Regioisomeric Xanthone-Based Thermally Activated Delayed Fluorescence Materials for Highly Efficient Blue Organic Light-Emitting Diodes
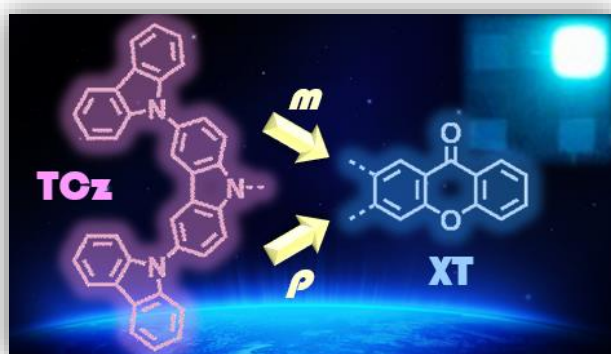
3. 1 Introduction

π-Conjugated donor–acceptor (D–A) molecules, which comprise an electron donor (D) unit and an electron acceptor (A) unit, are an important class of functional organic materials, owing to their unique optoelectronic and luminescent properties.[1] Since the donor and acceptor units primarily dominate the optoelectronic functionality of D–A molecules, their electronic coupling and intramolecular charge-transfer (ICT) interactions can be tuned by designing the D and A building blocks. Thus, exploring novel luminescent D–A systems and understanding the relationship between their chemical structure and optoelectronic properties are of great interest.

Over the last few years, TADF materials based on twisted D–A systems have emerged as a promising class of organic luminophores for the production of high-efficiency OLEDs without using rare metals.[2–4] The basic design strategy for achieving a small energy difference (ΔE_{ST}) between the lowest excited singlet (S_1) and triplet (T_1) states in a D–A molecule is to minimize the spatial overlap between the highest occupied molecular orbital (HOMO) and the lowest unoccupied molecular orbital (LUMO), in accordance with reduced electron-exchange interactions, by localizing these orbitals on the D and A constituents, respectively.[2–4] Therefore, not only the conformation (geometric structure) but also the linkage mode (regioisomeric structure) between the D and A units plays crucial roles for the degree of electronic coupling and ICT properties in such TADF emitters. Although a variety of D–A structured TADF emitters have been developed so far, there is very limited research on the regioisomeric effect on the photophysical and OLED characteristics of TADF materials.[5]

In this chapter, the author reports two regioisomeric blue TADF emitters consisting of xanthone (XT) as the A unit and *para-* or *meta*-linked 9,3':6',9''-tercarbazole (TCz) as the D unit, abbreviated as *p*-TCz-XT and *m*-TCz-XT. The effects of the regioisomeric D–A structures on their photophysical and TADF characteristics were examined. In comparison to *m*-TCz-XT, *p*-TCz-XT was found to exhibit superior EL properties. While XT derivatives have been widely studied as triplet sensitizers,[6] the XT unit has recently gained renewed attention for use as an efficient light-emitting material.[7] TADF-OLEDs employing *p*-TCz-XT and *m*-TCz-XT as blue emitters indeed achieved external EL quantum efficiencies (η_{ext}) as high as 14.4% and 12.1%, respectively, which are much higher than the theoretical limit of η_{ext} in conventional fluorescent OLEDs (η_{ext} <5%).

3. 2 Molelcular Design and Quantum Chemical Calculations

In chapter 2, high-efficiency xanthone-based TADF materials were introduced. Unfortunately, these materials exhibited light-blue emission because of strong electron-donating ability of acridan donor units. To obtain efficient blue TADF, TCz was employed as a donor unit, which has weaker electron-donating ability than the acridan donor unit, and hence should demonstrate efficient blue emission as well as a short emission lifetime, results from the Wurster structure (>N—aryl—N<) of tercarbazole.[8] Two regioisomeric blue TADF emitters consisting of xanthone (XT) as the A unit and *para-* or *meta-*linked TCz as the D unit, abbreviated as *p*-TCz-XT and *m*-TCz-XT (Figure 4-1) were designed.
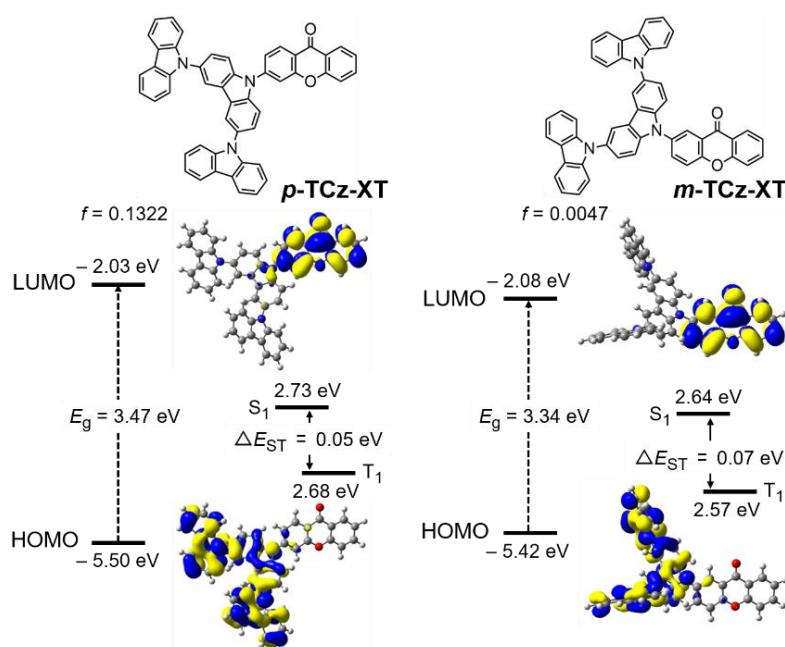
Figure 3-1. Molecular structures, HOMO and LUMO distributions, singlet and triplet energy levels, and oscillator strength (*f*) for *p*-TCz-XT and *m*-TCz-XT calculated at the PB1PBE/6-31G(d) level.

To understand the structure–property relationship at the molecular level, the geometrical and electronic properties were analyzed using time-dependent density functional theory (TD-DFT) calculations. As illustrated in Figure 4-1, *p*-TCz-XT and *m*-TCz-XT adopt a twisted D–A conformation in their optimized ground (S$_0$) state, with dihedral angles of 51° and 55°, respectively, between the XT unit and the adjacent carbazole unit. The highly twisted D–A conformations can effectively suppress the delocalization of electron density distribution; as a consequence, the HOMOs and LUMOs of both molecules are mostly localized on the electron-donating TCz and electron-accepting XT units, respectively. The calculated S$_1$ states of these

molecules mainly consist of the HOMO→LUMO transition with an ICT nature. Therefore, such well-separated frontier orbital distributions resulted in reasonably small calculated ΔE_{ST} values of 0.05 and 0.07 eV for *p*-TCz-XT and *m*-TCz-XT, respectively, allowing for efficient reverse intersystem crossing. If a single carbazole unit is introduced on the XT unit instead of the TCz unit in *p*-TCz-XT and *m*-TCz-XT, the calculated ΔE_{ST} values would be increased to 0.32 and 0.31 eV, respectively (Figure 4-2), because of insufficient spatial separation between their HOMO and LUMO.[8] In addition, for the S_1 state of *p*-TCz-XT, the oscillator strength (*f*) was calculated to be 0.1322, which is much larger than that of *m*-TCz-XT (*f* = 0.0047). Accordingly, a higher photoluminescence quantum yield (Φ_{PL}) as well as a higher radiative decay rate from the S_1 state can be expected in *p*-TCz-XT as compared to *m*-TCz-XT, owing to the para-linked D–A arrangement.
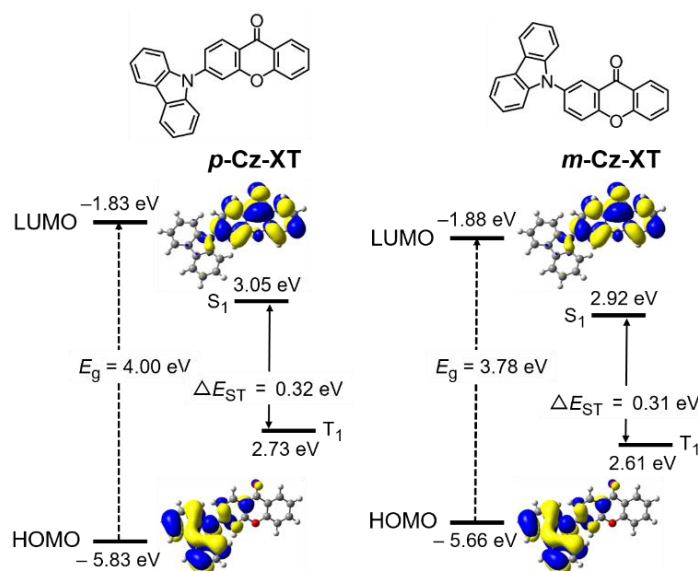
Figure 3-2. HOMO and LUMO distributions and S_1 and T_1 energy levels for monocarbazolyl analogs, *p*-Cz-XT and *m*-Cz-XT, calculated at the PBE1PBE/6-31G(d) level.

3. 3 Solvatochromic Analysis

Steady-state absorption and photoluminescence (PL) spectra of *p*-TCz-XT and *m*-TCz-XT in solvents with different polarities are depicted in Figure 4-3, and pertinent photophysical data are listed in Table 1. While the strong absorption bands below 300 nm originate from the π–π* transitions, weaker absorption bands ranging from 320 to 340 nm are attributable to the n–π* transitions of the TCz and XT units (Figure 4-4). Additionally, a lower-energy weak ICT absorption appeared at around 350–370 nm. The ICT absorption of *m*-TCz-XT was indeed much weaker than that of *p*-TCz-XT, supporting the foregoing theoretical calculation results.

The Φ_{PL} value of *p*-TCz-XT in toluene was noticeably high (99%), compared to that of *m*-TCz-XT (29%).

Intriguingly, the PL spectra of these XT-based molecules exhibited positive solvatochromism, whereas the absorption spectra presented trivial solvent dependence (Fig. 4-3a, b). Evidently, their PL emissions were bathochromically shifted in color and weakened in intensity as solvent polarity increased. For instance, the ICT emission maximum of *p*-TCz-XT was shifted from 454 nm in the non-polar toluene to 575 nm in the highly polar *N,N*-dimethylformamide (DMF). A locally excited (LE) emission band was also observed at a shorter wavelength (ca. 390–410 nm) on account of the weakened ICT emission intensity in highly polar solvents. Similar dual emission behavior was reported for some D–A molecules such as 4-(*N,N*-dimethylamino)benzonitrile, which exhibits twisted intramolecular charge transfer (TICT).[9] *p*-TCz-XT and *m*-TCz-XT can likewise undergo torsional motion along the D–A bond upon photoexcitation and lead to a charge-separated TICT excited state. The driving force for the TICT state formation is the increase in the dipole moment of the photoexcited S_1 state, which results in better solvation in polar media. On the basis of the solvatochromic analysis of *p*-TCz-XT and *m*-TCz-XT (Fig. 4-3c), the difference in their dipole moments ($\Delta\mu = \mu_e - \mu_g$) between the S_1 state and the ground (S_0) state can be evaluated from the slopes of the linear plots of the Stokes shift ($\Delta\nu$) versus the solvent polarity parameter (Δf), using the Lippert–Mataga eqn (1):[10]

$$\Delta\nu = \frac{1}{4\pi\varepsilon_0} \cdot \frac{2(\mu_e - \mu_g)^2}{hca^3} \cdot \Delta f + \text{constant} \tag{3-1}$$

where ε_0 is the vacuum permittivity, h is the Planck constant, c is the speed of light, and a is the Onsager solvent cavity radius (a = 6.9 Å for *p*-TCz-XT and 6.7 Å for *m*-TCz-XT) which was derived from the DFT calculations by adopting the Onsager model. Δf is defined by eqn (2), in which ε is the dielectric constant and n is the refractive index of each solvent.

$$\Delta f = \frac{\varepsilon - 1}{2\varepsilon + 1} - \frac{n^2 - 1}{2n^2 + 1} \tag{3-2}$$

As can be seen from Fig. 2c, both regioisomeric *p*-TCz-XT and *m*-TCz-XT displayed reasonable linear dependence, together with similar large slopes, indicating that their S_1 states were polarized and had larger dipole moments than the corresponding S_0 states, even in a low-polarity solvent such as toluene. The excited-state dipole moments (μ_e) for *p*-TCz-XT and *m*-TCz-XT were estimated to be 28.5 and 29.3 D, respectively, which were considerably larger than the calculated ground-state dipole moments (μ_g = 4.5 and 8.1 D, respectively). These

results present strong evidence for the formation of the charge-separated TICT excited states in these molecules, irrespective of their different linkage modes.
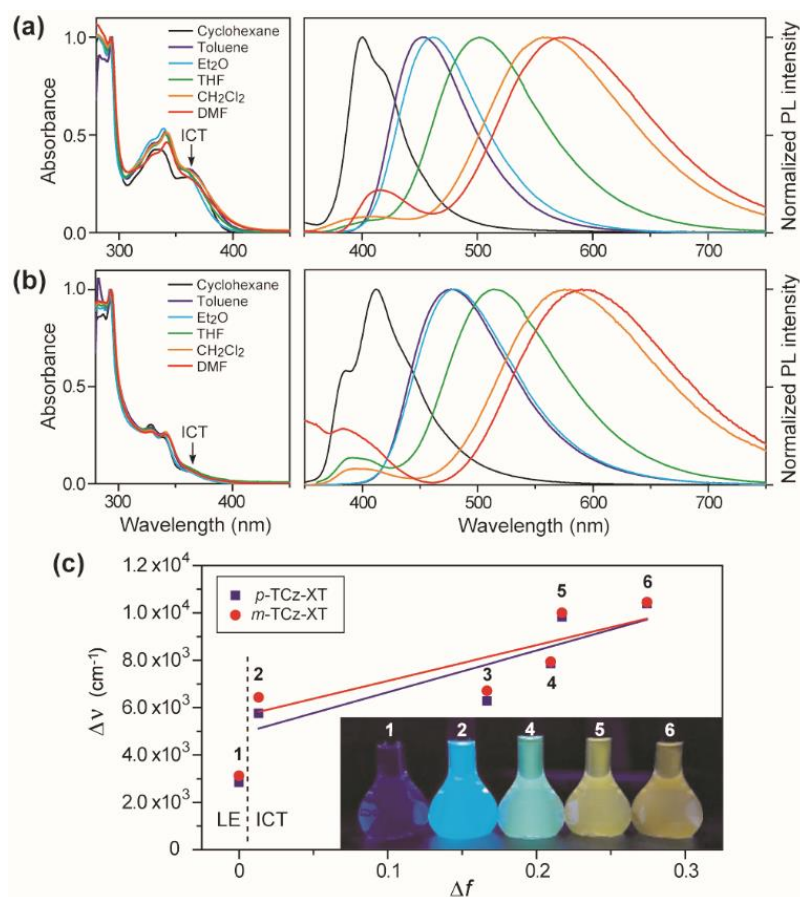
Figure 3-3. UV–vis absorption and PL spectra of (a) *p*-TCz-XT and (b) *m*-TCz-XT in different solvents. (c) Plots of Stokes shifts (Δv) as a function of solvent polarity (Δf). Nomination of solvents: cyclohexane (1), toluene (2), Et$_2$O (3), THF (4), CH$_2$Cl$_2$ (5), and DMF (6). Inset: photograph showing emission colors of *p*-TCz-XT in different solvents under UV irradiation at 365 nm. Note that the data points for cyclohexane solutions in (c) were excluded from the linear fits because of the LE emission characteristics.
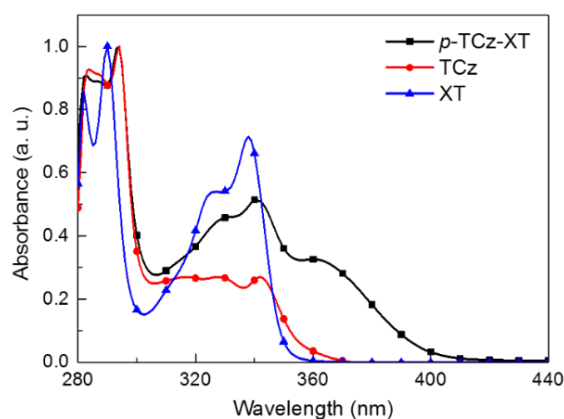
Figure 3-4. UV-vis absorption spectra of TCz and XT in toluene.

3. 4 Photophysical and TADF Properties

Since *p*-TCz-XT and *m*-TCz-XT are developed as TADF emitters for OLEDs, it is imperative to investigate the photophysical properties in solution as well as in thin films embedded in a solid host matrix. To prevent the backward excited energy transfer from the guest to the host in co-deposited films, we employed 2,8-bis(diphenylphosphoryl)dibenzo[*b,d*]furan (PPF)[11] as a host material, which possesses a higher T_1 energy (E_T = 3.1 eV) than those of *p*-TCz-XT and *m*-TCz-XT (E_T = 2.99 and 2.92 eV, respectively, Figure 4-5).
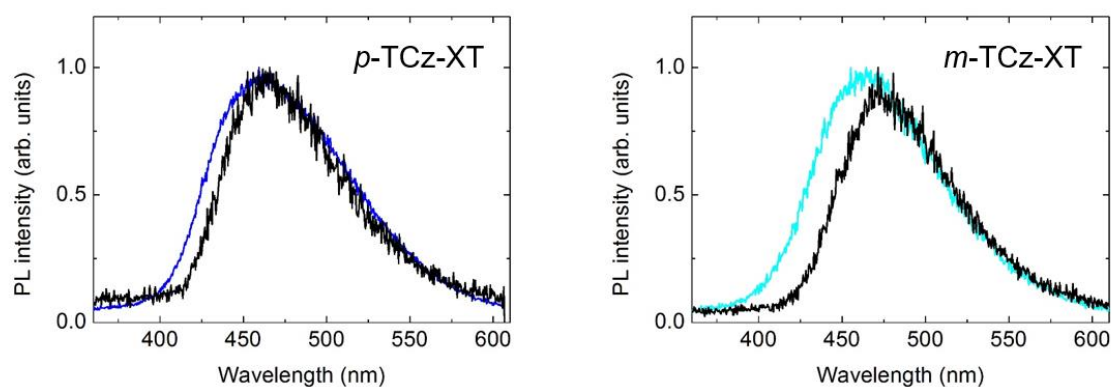
Figure 3-5. Fluorescence spectra (blue and light-blue lines) and phosphorescence spectra at 10 K (black lines) for *p*-TCz-XT:PPF and *m*-TCz-XT:PPF doped films.

As shown in Figure 4-6, temperature-dependent transient PL measurements revealed obvious TADF characteristics of *p*-TCz-XT and *m*-TCz-XT in their doped films. The transient PL curves clearly indicated two-component emission decays, consisting of a nanosecond-scale prompt component and a microsecond-scale delayed component at ambient temperature (300 K). Because the delayed emissions appeared with the same spectral distribution as the prompt fluorescence stemming from the S_1 state but with much longer transient lifetimes (Figure 4-6a, b), the long-lived emissions can be ascribed to TADF. Moreover, the delayed emission intensity gradually increased with increasing temperature from 10 to 300 K (Figure 4-6c, d), indicative of thermally activated up-conversion from the T_1 to S_1 states. At 300 K, the Φ_{PL} values of *p*-TCz-XT and *m*-TCz-XT in the doped films reached 84% and 72%, respectively (see Table 4-1). By comparing the proportion of the integrated intensities of each component to the overall Φ_{PL} values, the prompt and delayed fluorescence quantum yields (Φ_{PF} and Φ_{DF}) were thus determined to be 54% and 30% for *p*-TCz-XT and 21% and 51% for *m*-TCz-XT, respectively. From these results, the radiative decay rates from the S_1 state ($k_{r,S} = \Phi_{PF}/\tau_{PF}$) for *p*-TCz-XT and *m*-TCz-XT can be calculated to be 4.9×10^7 and 8.4×10^6 s^{-1}, respectively. It is noteworthy that the $k_{r,S}$ of *p*-TCz-XT is one order of magnitude larger than that of *m*-TCz-XT, whereas

these materials show similar values for the intersystem-crossing rates ($k_{ISC} = (1-\Phi_{PF})/\tau_{PF}$) on the order of 10^7.
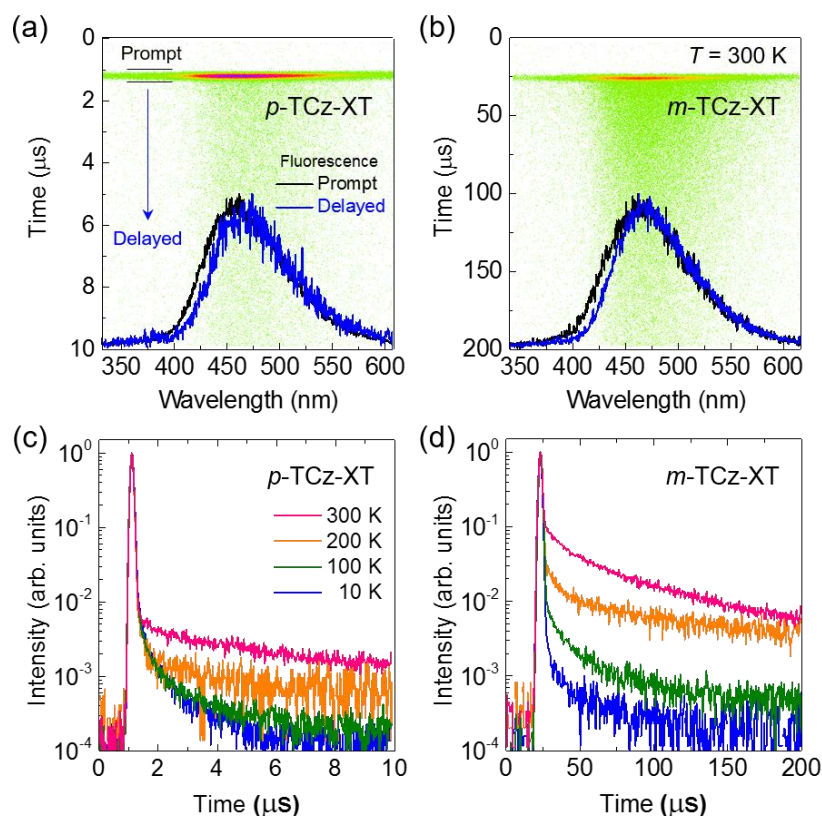
Figure 3-6. Top: streak images and time-dependent PL spectra for (a) 6 wt%-*p*-TCz-XT:PPF and (b) 6 wt%-*m*-TCz-XT:PPF doped films measured at 300 K. Bottom: temperature dependence of transient PL decays ranging from 10 to 300 K for (c) 6 wt%-*p*-TCz-XT:PPF and (d) 6 wt%-*m*-TCz-XT:PPF doped films.

Table 3-1. Photophysical properties for regioisomeric xanthone-based TADF emitters

compound	λ_{abs} (nm) sol[a]	λ_{PL} (nm) sol[a] / film[b]	Φ_{PL}[c] (%) sol[a] / film[b]	τ_{PF}[d] (ns)	τ_{DF}[d] (µs)	HOMO[e] (eV)	LUMO[f] (eV)	E_S[g] (eV)	E_T[g] (eV)	ΔE_{ST}[h] (eV)
p-TCz-XT	294,329[j], 340,360[j]	454 / 464	99 / 84	11	8.5	−5.73	−2.81	3.06	2.99	0.07
m-TCz-XT	294,328, 341,365[j]	477 / 473	29 / 72	25	103	−5.73	−3.12	3.04	2.92	0.12

[a] Measured in diluted toluene solution. [b] Measured in 6 wt%-doped thin films in a PPF solid host matrix. [c] Absolute PL quantum yield evaluated using an integrating sphere under N₂. [d] PL lifetimes of prompt fluorescence (τ_{PF}) and delayed fluorescence (τ_{DF}) components for the 6 wt%-doped films measured at 300 K. [e] Determined by photoelectron yield spectroscopy in neat films. [f] Deduced from the HOMO and optical energy gap (E_g) values using LUMO = HOMO + E_g. [g] Lowest singlet (E_S) and triplet (E_T) energies estimated from onset wavelengths of the emission spectra at 300 and 5 K in the doped thin films, respectively. [h] Singlet–triplet energy splitting determined experimentally using $\Delta E_{ST} = E_S − E_T$. [i] Calculated by TD-DFT at PBE1PBE/6-31G(d). [j] Shoulder peak.

3. 5 Electroluminescence Performance

To evaluate the EL performance of *p*-TCz-XT and *m*-TCz-XT as TADF emitters, OLEDs were fabricated with the following device configuration (Figure 4-7): indium-tin-oxide (ITO, 100 nm)/HAT-CN (10 nm)/α-NPD (40 nm)/CCP (5 nm)/6 wt%-TADF emitter:PPF (20 nm)/PPF (10 nm)/TPBi (30 nm)/Liq (1 nm)/Al (80 nm). In this device structure, HAT-CN (2,3,6,7,10,11-hexacyano-1,4,5,8,9,12-hexaazatriphenylene) and α-NPD (4,4'-bis-[*N*-(1-naphthyl)-*N*-phenylamino]-1,1'-biphenyl) served as a hole-injection layer and hole-transporting layer, respectively; while TPBi (1,3,5-tris(*N*-phenylbenzimidazol-2-yl)benzene) and Liq (8-hydroxyquinoline lithium) were used as an electron-transporting layer and electron-injection material, respectively. Additionally, thin layers of high-E_T CCP (9-phenyl-3,9'-bicarbazole) and PPF were incorporated as exciton-blocking layers.

As shown in Figure 4-8a, the *p*-TCz-XT and *m*-TCz-XT-based devices displayed blue EL emissions with the peaks at 473 and 484 nm, and their EL spectra were comparable to the corresponding PL spectra.
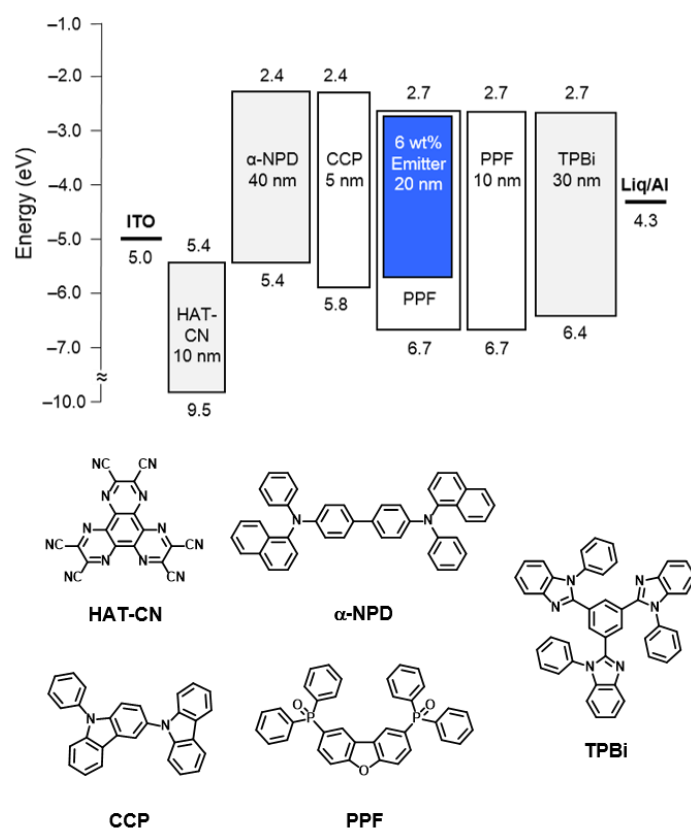
Figure 3-7. Energy-level diagram for TADF-OLEDs based on *p*-TCz-XT and *m*-TCz-XT as emitters (top) and chemical structures of the materials used in the devices (bottom).
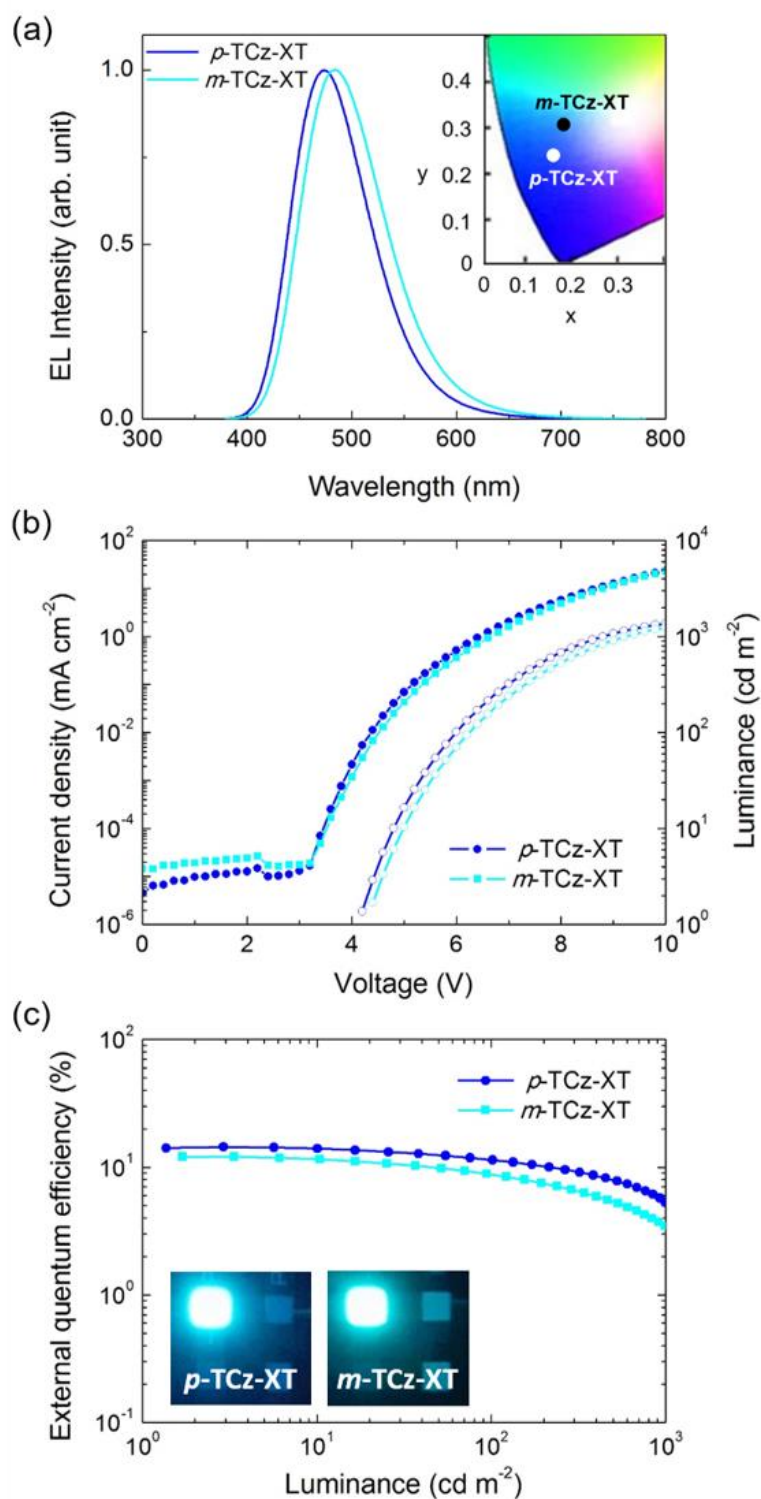
Figure 3-8. (a) EL spectra measured at 10 mA cm^{-2} (inset: EL color coordinates on the CIE 1931 chromaticity diagram), (b) current density–voltage–luminance (*J–V–L*) characteristics, and (c) external EL quantum efficiency (η_{ext}) versus luminance plots for the TADF-OLEDs (inset: photographs displaying EL emissions).

The Commission Internationale de l'Éclairage (CIE) color coordinates of the *p*-TCz-XT and *m*-TCz-XT-based devices were (0.16, 0.24) and (0.18, 0.31), respectively. Figure 4-8b and 4-8c show the current density–voltage–luminance (*J–V–L*) and η_{ext}–*J* characteristics of these TADF-OLEDs. A high maximum η_{ext} of 14.4% was achieved in the *p*-TCz-XT-based TADF-OLED at low current densities. Moreover, even at a practical high luminance of 100 cd m^{-2}, the η_{ext} of the *p*-TCz-XT-based device remained as high as 11.4%, demonstrating reduced efficiency roll-off characteristics owing to the short delayed fluorescence lifetime (τ_{DF} = 8.5 μs; Table 1). The overall EL performance of the *m*-TCz-XT-based device (maximum η_{ext} = 12.1%) was slightly lower than that of the *p*-TCz-XT-based device, which is primarily attributable to its lower Φ_{PL} value. The relatively large efficiency roll-off in the *m*-TCz-XT-based device should originate from the long-lived excited state of the T$_1$ excitons (τ_{DF} = 103 μs), which undergoes exciton deactivation processes, such as triplet–triplet annihilation (TTA) and singlet–triplet annihilation (STA), degrading the EL efficiency.

3. 6 Conclusion

Two blue TADF emitters consisting of a xanthone acceptor unit and an isomeric *para-* or *meta*-linked tercarbazole donor unit were designed and synthesized. These luminophores exhibited obvious TICT characteristics, as revealed by solvatofluorochromism and transient PL analyses. Their TADF properties as well as EL device characteristics were significantly affected by the regioisomeric linkage mode. The best OLED performance was attained based on *para*-linked *p*-TCz-XT, which exhibited a maximum EL quantum efficiency of 14.4%. These results can provide valuable information for future design strategy for organic semiconductors with efficient light emission toward OLED applications.

3. 7 Experimental Section

3. 7. 1 Materials and Synthesis

All regents and solvents were purchased from Sigma-Aldrich, Tokyo Chemical Industry (TCI), or Wako Pure Chemical Industries, and used as received unless otherwise noted. 3-bromoxanthone,[7a] 9,3':6',9''-tercarbazole,[12] 9-phenyl-3,9'-bicarbazole (CCP),[3g] and 2,8-bis(diphenylphosphoryl)dibenzo[*b,d*]furan (PPF)[13] were prepared according to the literature procedures, and were further purified by temperature-gradient vacuum sublimation. 2,3,6,7,10,11-Hexacyano-1,4,5,8,9,12-hexaazatriphenylene (HAT-CN) was donated by the Nippon Soda Co., Ltd. and was purified by vacuum sublimation before use. Other OLED

materials were purchased from E-Ray Optoelectronics Technology Co., Ltd., and were used for the device fabrication without further purification.

NMR spectra were recorded on a Bruker Avance III 400 spectrometer. Chemical shifts of ^{1}H and ^{13}C NMR signals were referenced to tetramethylsilane ($\delta = 0.00$), CDCl$_3$ ($\delta = 77.0$), and DMSO-d_6 ($\delta = 39.5$) as internal standards, respectively. Matrix-assisted laser desorption ionization time-of-flight (MALDI-TOF) mass spectra were collected on a Bruker Daltonics Autoflex III spectrometer using dithranol as the matrix. Elemental analysis was performed using a Yanaco MT-5 CHN corder.
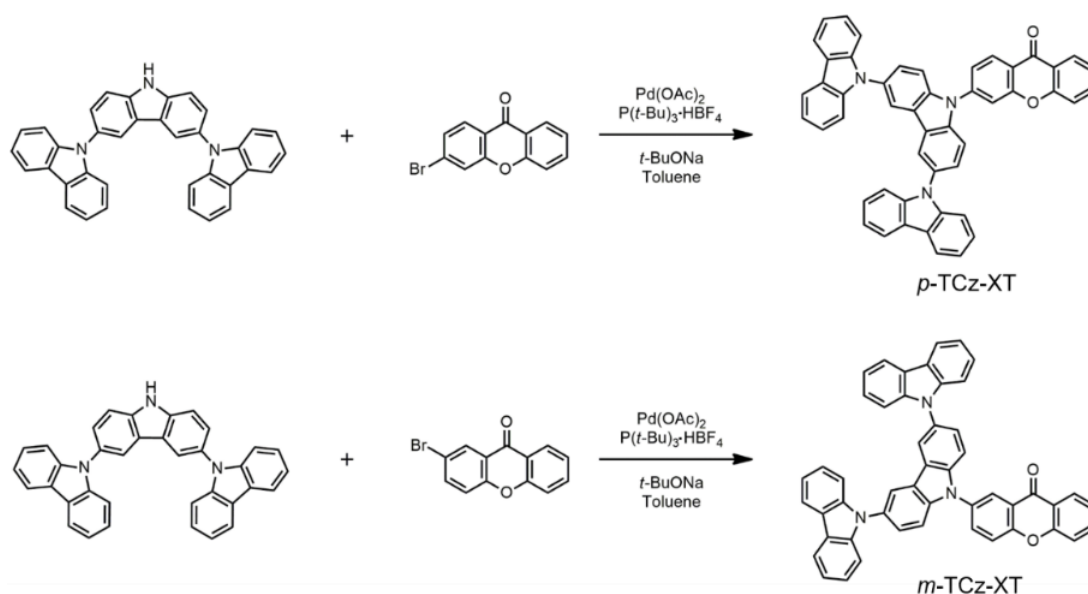
Scheme 1. Synthesis of *p*-TCz-XT and *m*-TCz-XT.

Synthesis of *p*-TCz-XT: Pd(OAc)$_2$ (0.03 g, 0.13 mmol), P(*t*-Bu)$_3$·HBF$_4$ (0.20 g, 0.69 mmol), and *t*-BuONa (1.03 g, 10.7 mmol) were added to a solution of 3-bromoxanthone (1.23 g, 4.47 mmol) and 9,3′:6′,9″-tercarbazole (2.23 g, 4.48 mmol) in dry toluene (50 mL). The mixture was refluxed for 72 h under N$_2$. After cooling to room temperature, the reaction mixture was poured into water and then extracted with CHCl$_3$. The combined organic layers were washed with water and dried over anhydrous Na$_2$SO$_4$. After filtration and evaporation, the product was purified by silica-gel column chromatography (eluent: ethyl acetate/hexane = 1:9, v/v), recrystallized from CHCl$_3$/ hexane, and dried under vacuum to afford *p*-TCz-XT as a light yellow solid (yield = 1.50 g, 49%). This compound was further purified by temperature-gradient sublimation before use. ^{1}H NMR (400 MHz, DMSO-d_6): δ 8.75 (d, $J = 2.1$ Hz, 2H), 8.57 (d, $J = 8.5$ Hz, 1H), 8.30 (dd, $J = 8.0$ Hz, 1.7 Hz, 1H), 8.27 (d, $J = 7.7$ Hz, 5H), 8.01 (dd, $J = 8.5$ Hz, 1.9 Hz, 1H), 7.98–

7.94 (m, 3H), 7.75 (td, J = 8.0 Hz, 2.1 Hz, 3H), 7.57 (td, J = 7.5 Hz, 0.9 Hz, 1H), 7.46–7.40 (m, 8H), 7.29 (td, J = 7.2 Hz, 1.5 Hz, 4H). ^{13}C NMR (100 MHz, CDCl$_3$): δ 176.36, 157.28, 156.34, 143.06, 141.65, 139.80, 135.28, 131.36, 129.19, 126.94, 126.65, 125.97, 124.74, 124.56, 123.26, 122.19, 122.03, 121.01, 120.37, 119.92, 119.85, 118.05, 115.50, 111.45, 109.62. MS (MALDI-TOF): *m/z* calcd 691.23 [*M*]$^+$; found, 691.56. Anal. calcd (%) for C$_{49}$H$_{29}$N$_3$O$_2$: C 85.07, H 4.23, N 6.07; found: C 84.98, H 4.11, N 6.13.

Synthesis of *m*-TCz-XT: Pd(OAc)$_2$ (0.01 g, 0.04 mmol), P(*t*-Bu)$_3$·HBF$_4$ (0.08 g, 0.28 mmol), and *t*-BuONa (0.42 g, 4.37 mmol) were added to a solution of 2-bromoxanthone (0.50 g, 1.82 mmol) and 9,3′:6′,9″-tercarbazole (0.90 g, 1.81 mmol) in dry toluene (40 mL). The mixture was refluxed for 72 h under N$_2$. After cooling to room temperature, the reaction mixture was poured into water and then extracted with CHCl$_3$. The combined organic layers were washed with water and dried over anhydrous Na$_2$SO$_4$. After filtration and evaporation, the product was purified by silica-gel column chromatography (eluent: ethyl acetate/hexane = 1:5, v/v), recrystallized from CHCl$_3$/hexane, and dried under vacuum to afford *m*-TCz-XT as a light yellow solid (yield = 0.63 g, 50%). This compound was further purified by temperature-gradient sublimation before use. ^{1}H NMR (400 MHz, DMSO-*d$_6$*): δ 8.72 (d, J = 1.8 Hz, 2H), 8.54 (d, J = 2.7 Hz, 1H), 8.37 (dd, J = 8.9 Hz, 2.7 Hz, 1H), 8.28 (dd, J = 8.0 Hz, 1.6 Hz, 1H), 8.26 (d, J = 7.8 Hz, 4H), 8.08 (d, J = 8.9 Hz, 1H), 7.97 (td, J = 7.8 Hz, 1.7 Hz, 1H), 7.80 (d, J = 8.1 Hz, 1H), 7.75–7.69 (m, 4H), 7.57 (td, J = 7.5 Hz, 0.9 Hz, 1H), 7.44–7.39 (m, 8H), 7.28 (td, J = 7.2 Hz, 1.5 Hz, 4H). ^{13}C NMR (100 MHz, CDCl$_3$): δ 176.54, 156.26, 155.31, 141.74, 140.65, 135.45, 133.61, 133.15, 130.81, 126.94, 126.51, 125.94, 125.15, 124.60, 124.18, 123.22, 123.20, 121.61, 120.49, 120.31, 119.88, 119.75, 118.19, 111.09, 109.70. MS (MALDI-TOF): *m/z* calcd 691.23 [*M*]$^+$; found, 691.16. Anal. calcd (%) for C$_{49}$H$_{29}$N$_3$O$_2$: C 85.07, H 4.23, N 6.07; found: C 85.24, H 4.14, N, 6.13.

3. 7. 2 Quantum Chemical Calculations

Density functional theory (DFT) calculations were performed using the Gaussian 09 program package. The molecular geometries in the ground state were optimized using the PBE1PBE functional with the 6-31G(d) basis set in the gas phase. The lowest singlet and triplet excited states were computed using the optimized structures with time-dependent DFT (TD-DFT) at the same level.

3. 7. 3 Photophysical Characterizations

Organic thin films for photophysical measurements were prepared by vacuum deposition under high vacuum ($\sim 7 \times 10^{-5}$ Pa) onto quartz glass or Si(100) substrates. UV–vis absorption and photoluminescence (PL) spectra were measured with a JASCO V-670 spectrometer and a JASCO FP-8600 spectrophotometer, respectively, using degassed spectral grade solvents. The absolute PL quantum yields ($\varPhi_{PL}$) were determined using a JASCO ILF-835 integrating sphere system by photoexcitation of 290 nm. The transient PL characteristics of doped thin films were performed using a Hamamatsu Photonics C11367 Quantaurus-tau fluorescence lifetime spectrometer (λ_{ex} = 340 nm, pulse width = 100 ps, repetition rate = 20 Hz) under N_2, and a Hamamatsu Photonics C9300 streak camera with an N_2 gas laser (λ_{ex} = 337 nm, pulse width = 500 ps, and repetition rate = 20 Hz) under vacuum ($< 4 \times 10^{-1}$ Pa). The HOMO energy levels of the materials in thin films were determined using a Riken-Keiki AC-2 ultraviolet photoelectron spectrometer. The LUMO energy levels were estimated by subtracting the optical energy gap (E_g) from the measured HOMO energies; E_g values were determined from the high-energy onset position of the PL spectra of thin films.

3. 7. 4 OLED Fabrication and Measurements

Indium tin oxide (ITO)-coated glass substrates were cleaned with detergent, deionized water, acetone, and isopropanol. The substrates were then subjected to UV–ozone treatment for 30 min before they were loaded into a vacuum evaporation system. The organic layers and a cathode aluminum layer were thermally evaporated on the substrates under vacuum ($< 6 \times 10^{-5}$ Pa) with an evaporation rate of < 0.3 nm s^{-1} through a shadow mask. The layer thickness and deposition rate were monitored in situ during deposition by an oscillating quartz thickness monitor. OLED characteristics were measured using a Keithley 2400 source meter and a Konica Minolta CS-2000 spectroradiometer.

References

[1]   a) Y. Li, T. Liu, H. Liu, M.-Z. Tian, Y. Li, *Acc. Chem. Res.* **2014**, *47*, 1186; b) T.-D. Kim, K.-S. Lee, *Macromol. Rapid Commun.* **2015**, *36*, 943; c) L. Duan, J. Qiao, Y. Sun, Y. Qiu, *Adv. Mater.* **2011**, *23*, 1137; d) M. Shimizu, T. Hiyama, *Chem. Asian J.* **2010**, *5*, 1516-1531; e) L. Dou, Y. Liu, Z. Hong, G. Li, Y. Yang, *Chem. Rev.* **2015**, *115*, 12633.

[2]   For reviews, see: a) Y. Tao, K. Yuan, T. Chen, P. Xu, H. Li, R. Chen, C. Zheng, L. Zhang, W. Huang, *Adv. Mater.* **2014**, *26*, 7931; b) N. Aizawa, I. S. Park, T. Yasuda, *AAPPS Bull.* **2016**, *26*, 9.

[3]   a) H. Uoyama, K. Goushi, K. Shizu, H. Nomura, C. Adachi, *Nature* **2012**, *492*, 234; b) Q. Zhang, J. Li, K. Shizu, S. Huang, S. Hirata, H. Miyazaki, C. Adachi, *J. Am. Chem. Soc.* **2012**, *134*, 14706; c) J. Lee, K. Shizu, H. Tanaka, H. Nomura, T. Yasuda, C. Adachi, *J. Mater. Chem. C* **2013**, *1*, 4599; d) S. Y. Lee, T. Yasuda, Y. S. Yang, Q. Zhang, C. Adachi, *Angew. Chem. Int. Ed.* **2014**, *53*, 6402; e) Q. Zhang, B. Li, S. Huang, H. Nomura, H. Tanaka, C. Adachi, *Nat. Photon.* **2014**, *8*, 326; f) S. Hirata, Y. Sakai, K. Masui, H. Tanaka, S. Y. Lee, H. Nomura, N. Nakamura, M. Yasumatsu, H. Nakanotani, Q. Zhang, K. Shizu, H. Miyazaki, C. Adachi, *Nat. Mater.* **2015**, *14*, 330; g) M. Numata, T. Yasuda, C. Adachi, *Chem. Commun.* **2015**, *51*, 9443; h) I. S. Park, S. Y. Lee, C. Adachi, T. Yasuda, *Adv. Funct. Mater.* **2016**, *26*, 1813; i) S. Y. Lee, C. Adachi, T. Yasuda, *Adv. Mater.* **2016**, *28*, 4626; j) I. S. Park, J. Lee, T. Yasuda, *J. Mater. Chem. C* **2016**, *4*, 7911.

[4]   a) H. Wang, L. Xie, Q. Peng, L. Meng, Y. Wang, Y. Yi, P. Wang, *Adv. Mater.* **2014**, *26*, 5198; b) V. Jankus, P. Data, D. Graves, C. McGuinness, J. Santos, M. R. Bryce, F. B. Dias, A. P. Monkman, *Adv. Funct. Mater.* **2014**, *24*, 6178; c) J. W. Sun, J. Y. Baek, K.-H. Kim, C.-K. Moon, J.-H. Lee, S.-K. Kwon, Y.-H. Kim, J.-J. Kim, *Chem. Mater.* **2015**, *27*, 6675; d) D. R. Lee, M. Kim, S. K. Jeon, S.-H. Hwang, C. W. Lee, J. Y. Lee, *Adv. Mater.* **2015**, *27*, 5861; e) P. Rajamalli, N. Senthilkumar, P. Gandeepan, P.-Y. Huang, M.-J. Huang, C.-Z. Ren-Wu, C.-Y. Yang, M.-J. Chiu, L.-K. Chu, H.-W. Lin, C.-H. Cheng, *J. Am. Chem. Soc.* **2016**, *138*, 628; f) D. Zhang, M. Cai, Y. Zhang, D. Zhang, L. Duan, *Mater. Horiz.* **2016**, *3*, 145; g) T. Hatakeyama, K. Shiren, K. Nakajima, S. Nomura, S. Nakatsuka, K. Kinoshita, J. Ni, Y. Ono, T. Ikuta, *Adv. Mater.* **2016**, *28*, 2777; h) T.-A. Lin, T. Chatterjee, W.-L. Tsai, W.-K. Lee, M.-J. Wu, M. Jiao, K.-C. Pan, C.-L. Yi, C.-L. Chung, K.-T. Wong, C.-C. Wu, *Adv. Mater.* **2016**, *28*, 6976; i) K. Wu, T. Zhang, L. Zhan, C. Zhong, S. Gong, N. Jiang, Z.-H. Lu, C. Yang, *Chem. Eur. J.* **2016**, *22*, 10860.

[5]   a) K. Wu, T. Zhang, L. Zhan, C. Zhong, S. Gong, Z.-H. Lu, C. Yang, *Adv. Opt. Mater.* **2016**, *4*, 1558; b) D.-Y. Chen, W. Liu, C.-J. Zheng, K. Wang, F. Li, S.-L. Tao, X.-M. Ou, X.-H. Zhang, *ACS Appl. Mater. Interfaces* **2016**, *8*, 16791.

[6]   a) H. J. Pownall, J. R. Huber, *J. Am. Chem. Soc.* **1971**, *93*, 6429; b) J. C. Scaiano, *J. Am. Chem. Soc.* **1980**, *102*, 7747; c) B. Nickel, G. Roden, *Chem. Phys. Lett.* **1980**, *74*, 368; d) R. E. Connors, W. R. Christian, *J. Phys. Chem.* **1982**, *86*, 1524; e) S. Jockusch, H. J. Timpe, W. Schnabel, N. J. Turro, *J. Phys. Chem.* **1997**, *101*, 440; f) V. Rai-Constapel, M. Etinski, C. M. Marian, *J. Phys. Chem. A* **2013**, *117*, 3935.

[7]   a) H. Nakanotani, T. Higuchi, T. Furukawa, K. Masui, K. Morimoto, M. Numata, H. Tanaka, Y. Sagara, T. Yasuda, C. Adachi, *Nat. Commun.* **2014**, *5*, 4016; b) N. Aizawa, C.-J. Tsou, I. S. Park, T. Yasuda, *Polym. J.* **2016**, (DOI: 10.1038/pj.2016.82); c) Y. Zhang, H. Ma, S. Wang, Z. Li, K. Ye, J. Zhang, Y. Liu, Q. Peng, Y. Wang, *J. Phys. Chem. C* **2016**, *120*, 19759; d) C. M. Marian, *J. Phys. Chem. C* **2016**, *120*, 3715.

[8]   S. Y. Lee, T. Yasuda, H. Nomura, C. Adachi, *Appl. Phys. Lett.* **2012**, *101*, 093306.

[9]   Z. R. Grabowski, K. Rotkiewicz, W. Rettig, *Chem. Rev.* **2003**, *103*, 3899.

[10]   a) E. Z. Lippert, *Z. Naturforsch. A: Phys. Sci.* **1955**, *10*, 541; b) N. Mataga, Y. Kaifu, M. Koizumi, *Bull. Chem. Soc. Jpn.* **1955**, *28*, 690.

[11]   P. A. Vecchi, A. B. Padmaperuma, H. Qiao, L. S. Sapochak, P. E. Burrows, *Org. Lett.* **2006**, *8*, 4211.

[12]   K. Albrecht, K. Yamamoto, *J. Am. Chem. Soc.* **2009**, *131*, 2244.

[13]   P. A. Vecchi, A. B. Padmaperuma, H. Qiao, L. S. Sapochak, P. E. Burrows, *Org. Lett.* **2006**, *8*, 42.

Chapter 4

Isobenzofuranone- and Chromone-Based Thermally Activated Delayed Fluorescence Materials for Reduced Efficiency Roll-Off in Blue Organic Light-Emitting Diodes
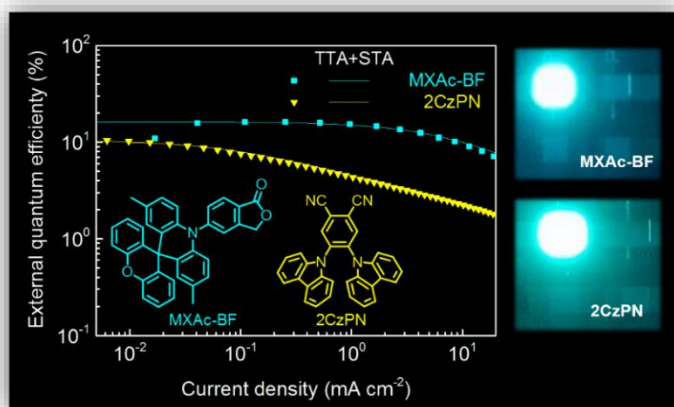
4. 1 Introduction

Over the past decade, much research has been focused on the development of red, green, and blue emitters for phosphorescent OLEDs.[1–3] Promising red and green phosphorescent organometallic iridium complexes have been reported with high quantum efficiency, high color purity, and long-term stability,[1,2] whereas devices containing blue phosphorescent emitters have exhibited lower operational stability than their counterparts owing to the limit to molecular design of pure blue emitters.[3] Furthermore, the use of expensive rare metal elements is indispensable to improve the exciton generation in phosphorescent OLEDs. To realize cost-effective and high-performance devices, purely organic luminescent molecules are essential prerequisites for next-generation OLEDs with high stability. The use of pure-organic TADF luminophores allows for internal electroluminescence (EL) quantum efficiencies (η_{int}) of nearly 100% in OLEDs by harvesting excited triplet excitons through up conversion of the lowest excited triplet (T_1) state to the emissive singlet (S_1) state.[4] Up to date, a few studies on various blue TADF emitters exhibiting high external EL quantum efficiency (η_{ext}) have been reported.[5] However, TADF-based OLEDs suffer from the exciton annihilation processes (so-called efficiency roll-off) such as triplet–triplet and singlet–triplet annihilations (TTA and STA) at high current density which are caused by their relatively long excited state lifetimes.[6] Hence, the reduction of the efficiency roll-off remains an important challenge for high-performance blue TADF-OLEDs.

In this chapter, a series of highly efficient isobenzofuranone or chromone-based blue TADF emitters with donor–acceptor (D–A) electronic structures are reported. Isobenzifuranone chromophores have been widely used as intermediates for the synthesis of various photochromic materials[7] as well as for the development of aggregation induced emission emitters for OLEDs.[8] Chromone derivatives have a good electrochemiluminescence properties and have been studied to advance molecular electronics because of intriguing electronic properties.[9] Blue EL emission with high η_{ext} of up to 16.2% and reduced efficiency roll-off can be achieved using isobenzofuranone and chromone derivatives as TADF emitters in OLEDs employing heavily doped emitting layers.

4. 2 Molecular Design and Quantum Chemical Calculations

In chapter 3, efficient blue TADF materials were designed and synthesized utilizing the tercabazole donor unit with the xanthone acceptor unit. However, these materials exhibited relatively lower Φ_{PL} than xanthone- and acridan-based light-blue TADF materials in chapter 2. In this chapter, a series of D–A compounds consisting of isobenzofuranone (BF) or 2-methyl chromone (CM) as an acceptor unit and spiro[2,7-dimethylacridan-9-9'-xanthene] (MXAc) or spiro[acridan-9-9'-xanthene] (XAc) as a donor unit was designed (Figure 4-1) for high-performance blue TADF. The BF and CM units which have relatively higher LUMO levels by shortening π-conjugation length at the LUMO states were selected to realize blue light emission.
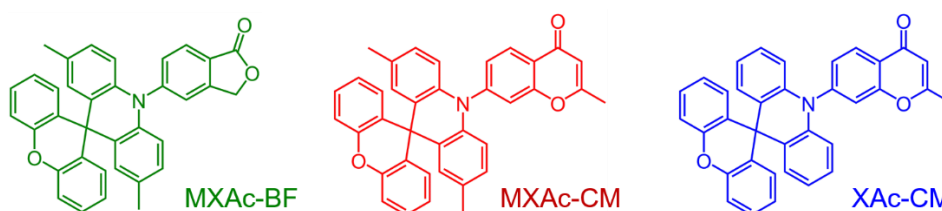
Figure 4-1. Molecular structures for MXAc-BF, MXAc-CM, and XAc-CM.

To gain insights into the geometrical and electronic properties at the molecular level, the highest occupied and the lowest unoccupied natural transition orbitals (NTOs) for the S_1 state of MXAc-BF, MXAc-CM, and XAc-CM were calculated with a time-dependent density functional theory (TD-DFT) method, which provide an orbital interpretation of intramolecular charge transfer (ICT) transition. As displayed in Figure 4-2, all of these molecules adopt nearly orthogonal D–A conformation in their optimized structures, with dihedral angles of about 88°, between the BF (or CM) and acridan units. Because of such highly twisted geometry between the donor and acceptor constituents, the highest occupied NTOs are thoroughly localized on the electron-donating acridan moiety, whereas the lowest unoccupied NTOs are predominantly distributed over the electron-accepting BF (or CM) units. Therefore, this clear separation of the NTOs leads to calculated small energy gap between the S_1 and T_1 states (ΔE_{ST}) values of 0.04–0.10 eV for these molecules, allowing for efficient reverse intersystem crossing (RISC). The replacement of CM-based acceptor with the xanthone (XT) acceptor results in a decrease of the LUMO level because of weak electron-withdrawing characteristics; as a consequence, the S_1 excitation energy for XAc-CM was calculated to be 2.84 eV, which is larger than that of XAc-XT (2.58 eV) in the previous chapter 2.[10] Accordingly, blue photoluminescence (PL) emission

can be expected in XAc-CM as compared to the light blue TADF emitter, XAc-XT, owing to the increased bandgap energy.
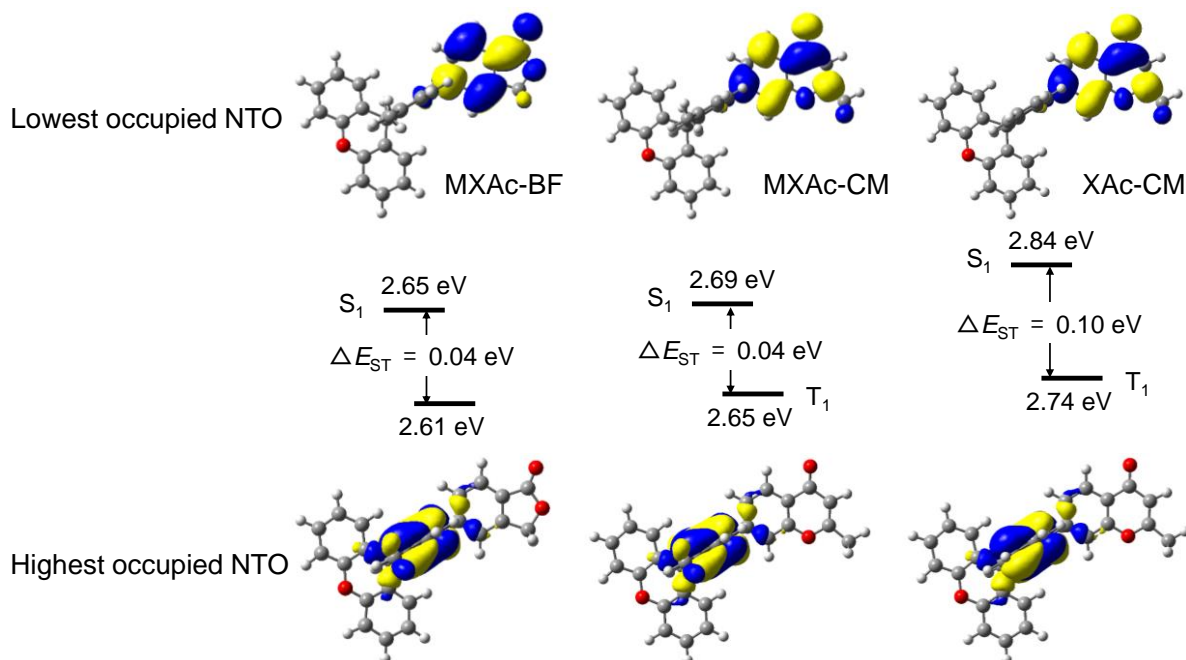
Figure 4-2. Natural transition orbitals of the lowest excited singlet states and singlet and triplet energy levels for MXAc-BF, MXAc-CM, and XAc-CM calculated at the PBE1PBE/6-31G(d) level.

4. 3 Photophysical and TADF Properties

The steady-state UV–vis absorption and PL spectra of MXAc-BF, MXAc-CM, and XAc-CM in toluene solution are dipicted in Figure 4-3 and the photophysical data are summarized in Table 4-1. The lower-energy weak absorption in the range of 350–400 nm could be assigned to the ICT transition from the acridan group to benzofuranone or chromone moieties. Upon photoexcitation, compounds MXAc-BF, MXAc-CM, and XAc-CM in dilute solution emit blue with emission peaks ranging from 449 to 468 nm.

In the absence of oxygen, compounds MXAc-BF, MXAc-CM, and XAc-CM exhibited PL quantum yields (Φ_{PL}) of 43–74%. Oxygen quenching of the excited triplet states by nitrogen bubbling leads to increased delayed fluorescence, which subsequently increases Φ_{PL}. For these compounds, both prompt and delayed fluorescence in the absence of oxygen were observed, whereas only prompt fluorescence was observed in the presence of triplet oxygen in aerated solutions. This results suggest that significantly efficient $T_1 \rightarrow S_1$ up conversion through RISC occurs in TADF molecules.
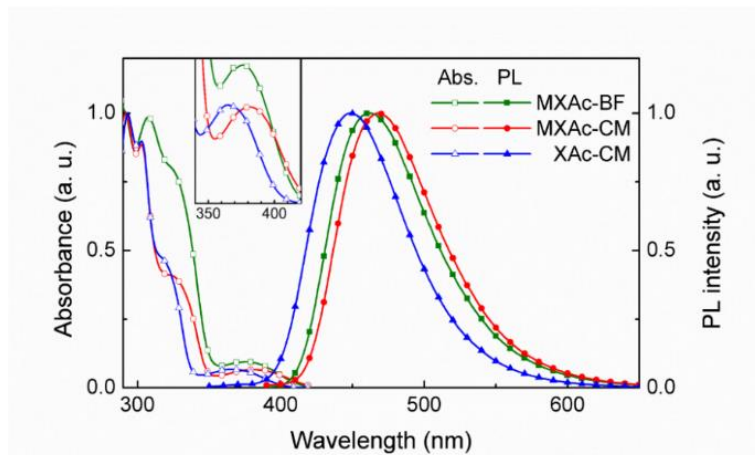
Figure 4-3. UV–vis absorption and PL spectra of MXAc-BF, MXAc-CM, and XAc-CM in toluene solution. The inset shows a magnified view of the lower-energy ICT absorptions.

Table 4-1. PL properties of the BF and CM-based TADF emitters in 1.0×10^{-5} M toluene solutions

Emitter	In aerated solution			After N$_2$ bubbling		
	Φ_{PL} (%)	τ_{PF} (ns)	τ_{DF} (µs)	Φ_{PL} (%)	τ_{PF} (ns)	τ_{DF} (µs)
MXAc-BF	16	12	n.d.	64	21	1.7
MXAc-CM	18	15	n.d.	74	34	0.9
XAc-CM	18	13	n.d.	43	25	0.3

To elucidate the photophysical and TADF properties, solid thin films containing high doping concentration (50 wt% and 100 wt%) of MXAc-BF, MXAc-CM, and XAc-CM were prepared by vacuum deposition and photophysical results are summarized in Table 4-2. For this host–guest system, 2,8-bis(diphenylphosphoryl)dibenzo[*b,d*]furan (PPF)[11] was selected as a host material possessing a high T$_1$ energy (E_T =3.1 eV) to prevent a back energy transfer from the guest to host and to control over the T$_1$ excitons confinement in the guest molecules. The Φ_{PL} of the heavily doped films of MXAc-BF, MXAc-CM, and XAc-CM in PPF (50 wt% doping concentration) are 88%, 79%, and 71%, respectively. The delayed fluorescence lifetimes (τ_{DF}) of 3.0–4.2 µs for compounds MXAc-BF, MXAc-CM, and XAc-CM are rather short compared with those of previously reported blue TADF emitters.[5c–5e,12] Using the onset of fluorescence and phosphorescence emission measured at 5 K, the ΔE_{ST} values of MXAc-BF, MXAc-CM, and XAc-CM were experimentally estimated to be in the range of 0.08–0.11 eV (Figure 4-4), which leading to thermal activation of the T$_1$→S$_1$ RISC in consequence of a shorter τ_{DF}. An obvious TADF feature of the doped films of MXAc-BF, MXAc-CM, and XAc-CM was revealed by analyzing temperature-dependent transition PL measurement using a streak camera.

For the 50 wt%-MXAc-BF:PPF codeposited film, the transient PL curve unambiguously indicated both a nanosecond-scale prompt component and a microsecond-scale delayed component at 300 K, as shown in Figure 4-5. Because the delayed emission appeared with a similar spectral distribution as the prompt fluorescence (Figure 4-5a), the delayed emission can be ascribed to the singlet emission through RISC processes. Furthermore, the long-live emission intensity gradually increased with increasing temperature from 10 K to 300 K (Figure 4-5b), indicating that the $T_1 \rightarrow S_1$ RISC process was accelerated by thermal energy. The prompt and delayed fluorescence quantum yields (Φ_{PF} and Φ_{DF}) can be determined from the proportion of integrated areas of each component to the total Φ_{PL} value in the transient PL decay curves (Figure 4-6), as listed in Table 4-2. For the MXAc-BF-doped film (Φ_{PL} = 88%), the fractional contributions of Φ_{PF} and Φ_{DF} were determined to be 34% and 54% at ambient temperature (300 K). In addition, the efficiencies (Φ_{ISC} and Φ_{RISC}) of intersystem crossing (ISC) and RISC values are calculated to be 66% and 82%, respectively. This result suggests that 66% of initially created S_1 excitons undergo $S_1 \rightarrow T_1$ ISC process; meanwhile, 82% of the formed T_1 excitons are up converted into the S_1 state through efficient $T_1 \rightarrow S_1$ RISC process which can ultimately lead to emit delayed fluorescence. The RISC efficiency of MXAc-BF (Φ_{RISC} = 82%) is found to be higher than those of MXAc-CM and XAc-CM (65% and 54%, respectively), whereas all compounds show similar Φ_{ISC} values ranging from 60% to 66%.

Table 4-2. Photophysical properties for isobenzofuranone and chromone-based TADF emitters

Compound	Doping conc. (wt%)	λ_{PL} (nm)	$\Phi_{PL}{}^a$ (%)	$\Phi_{PF}{}^b$ (%)	$\Phi_{DF}{}^c$ (%)	$\Phi_{ISC}{}^d$ (%)	$\Phi_{RISC}{}^e$ (%)	τ_{PF} (ns)^f/ τ_{DF} (μs)^f	$E_S{}^g$/ $E_T{}^g$ (eV)	$\Delta E_{ST}{}^h$ (eV)
MXAc-BF	50	478	88	34	54	66	82	24 / 4.2	2.98/2.90	0.08
	100	478	78	35	43	65	66	24 / 3.9		
MXAc-CM	50	484	79	40	39	60	65	33 / 3.0	2.95/2.87	0.08
	100	482	71	38	33	62	52	33 / 3.0		
XAc-CM	50	462	71	37	34	63	54	26 / 4.0	3.11/3.00	0.11
	100	461	53	37	16	63	26	25 / 2.7		

^{a}Absolute PL quantum yield evaluated using an integrating sphere under N_2. ^{b}Quantum efficiency of prompt fluorescence. ^{c}Quantum efficiency of delayed fluorescence. ^{d}Quantum efficiency of ISC. ^{e}Quantum efficiency of RISC. ^{f}PL lifetimes of prompt (τ_{PF}) and delayed (τ_{DF}) decay components at 300 K. ^{g}Lowest singlet (E_S) and triplet (E_T) energies estimated from onset wavelengths of the emission spectra at 10 K in the doped films, respectively. ^{h}Singlet–triplet energy splitting determined experimentally using $\Delta E_{ST} = E_S - E_T$.
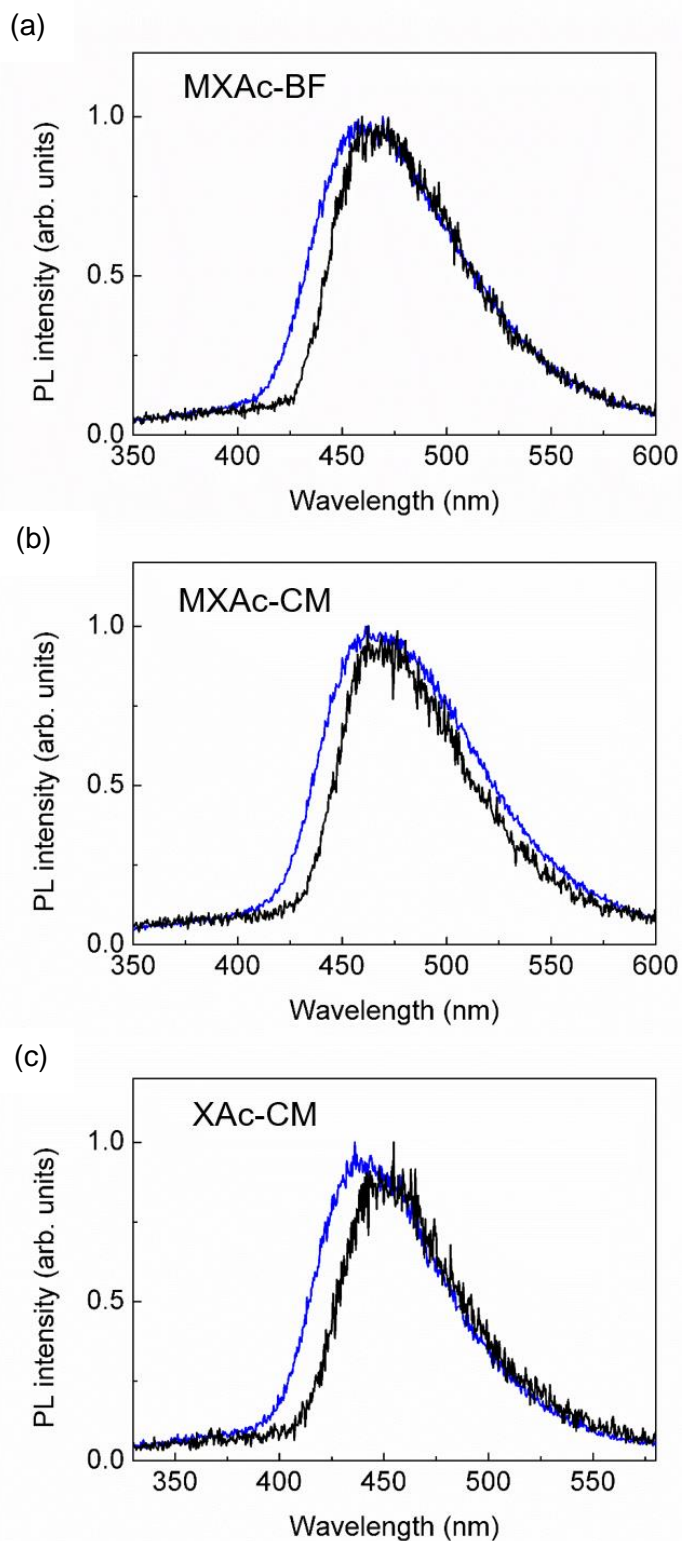
Figure 4-4. Fluorescence spectra (blue lines) and phosphorescence spectra (black lines) at 10 K for (a) 50 wt%-MXAc-BF:PPF, (b) 50 wt%-MXAc-CM:PPF, and (c) 50 wt%-XAc-CM:PPF doped films.
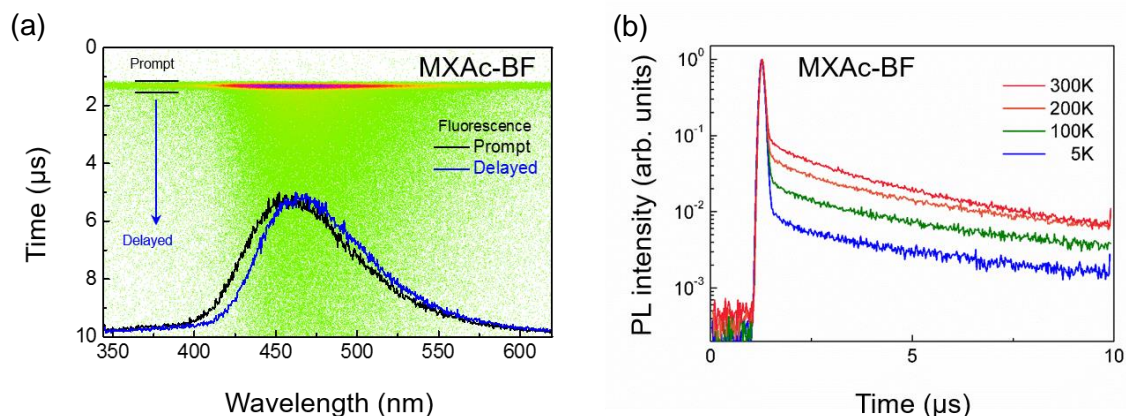
Figure 4-5. (a) Streak image and time-dependent PL spectra for 50 wt%-MXAc-BF:PPF doped film measured at 300 K. (b) temperature dependence of transient PL decay ranging from 10 to 300 K.
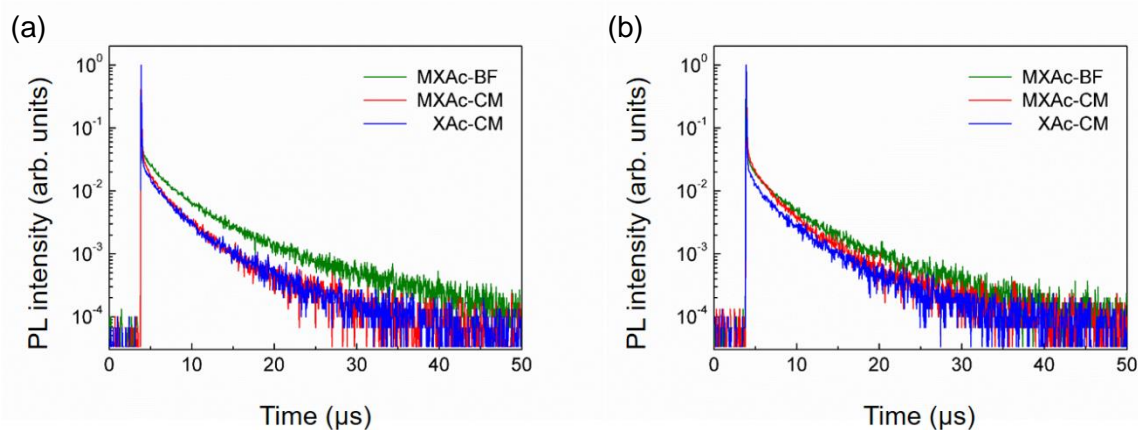
Figure 4-6. Transient PL decay curves of (a) BF and CM-based TADF molecules in a PPF solid host matrix at 50 wt% doping concentrations and (b) BF and CM-based TADF molecules in neat films.

4. 4 Electroluminescence Performance

To evaluate the EL performance of TADF emitters, multilayer OLEDs were fabricated using 50 wt%-emitter:PPF doped or non-doped films as the emitting layers (EML). The configuration of the devices was as follow (Figure 4-7): indium-tin-oxide (ITO, 100 nm)/HAT-CN (10 nm)/α-NPD (40 nm)/CCP (5 nm)/EML (20 nm)/PPF (10 nm)/TPBi (30 nm)/Liq (1 nm)/Al (80 nm). In this device architecture, HAT-CN (2,3,6,7,10,11-hexacyano-1,4,5,8,9,12-hexaazatriphenylene) and α-NPD (4,4'-bis-[*N*-(1-naphthyl)-*N*-phenylamino]-1,1'-biphenyl) served as a hole-injection layer and hole-transporting layer, respectively; while TPBi (1,3,5-tris(*N*-phenylbenzimidazol-2-yl)benzene) and Liq (8-hydroxyquinoline lithium) were used as an electron-transporting layer and electron-injection material, respectively. Additionally, thin

layers of CCP (9-phenyl-3,9'-bicarbazole) and PPF with high T_1 energy (E_T = 3.0 and 3.1 eV, respectively) were incorporated as exciton-blocking layers.
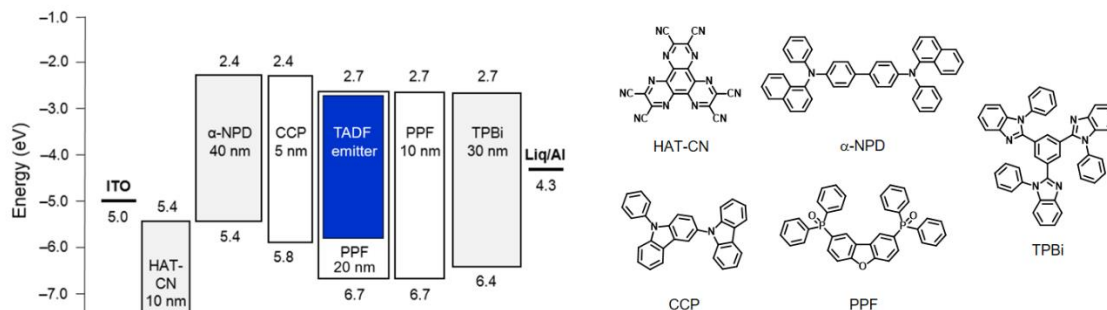
Figure 4-7. Energy-level diagram for TADF-OLEDs based on MXAc-BF, MXAc-CM and XAc-CM as emitters (left) and chemical structures of the materials used in the devices (right).

The EL spectra, current density–voltage–luminance (J–V–L) characteristics, and external EL quantum efficiency versus luminance (η_{ext}–L) characteristics of the fabricated TADF-OLEDs are shown in Figure 4-8, and the device parameters are compiled in Table 4-3. The devices using MXAc-BF, MXAc-CM, and XAc-CM at a high doping concentration (50 wt%) displayed blue EL emissions with the peaks at 479, 478, and 462 nm and the Commission Internationale de l'Éclairage (CIE) color coordinates were (0.17, 0.29), (0.16, 0.29), and (0.16, 0.19), respectively (Figure 4-8a). These devices indicated similar J–V characteristics with rather low turn-on voltages in the range of 3.0–3.6 V (Figure 4-8b). Remarkably, a considerably high η_{ext} of 16.1% was achieved for the device incorporating MXAc-BF at a doping concentration of 50 wt% (Figure 4-8c). The devices using MXAc-CM and XAc-CM at a 50 wt% doping concentration exhibited η_{ext} of 14.9% and 12.1%, respectively. In addition, the η_{ext} values for the devices containing MXAc-BF, MXAc-CM, and XAc-CM still remained as high as 11.9%, 11.0%, and 7.2%, respectively, at practical brightness of 1000 cd m^{-2} for lighting application. It is noteworthy that high EL efficienciency with the maximum η_{ext} value of 16.2% is attained for the non-doped device utilizing the MXAc-BF as a thin neat layer (Figure 4-8f). Moreover, the MXAc-BF-based non-doped device was still high η_{ext} value of 12.8%, even at a high luminance of 1000 cd m^{-2}. The MXAc-CM and XAc-CM-based non-doped OLEDs without using an additional host material exhibited η_{ext} of 11.0% and 8.2%, respectively.

Figure 4-8. (a–c) Performance of TADF OLEDs based on 50 wt%-doped emission layers and (d–f) non-doped neat (100 wt%) emission layers measured at 10 mA^{-2}, including (a, d) EL spectra, (b, e) current density–voltage–luminance (J–V–L) characteristics, and (c, f) external EL quantum efficiency versus luminance (η_{ext}–L) characteristics.

Table 4-3. Device performances of TADF OLEDs

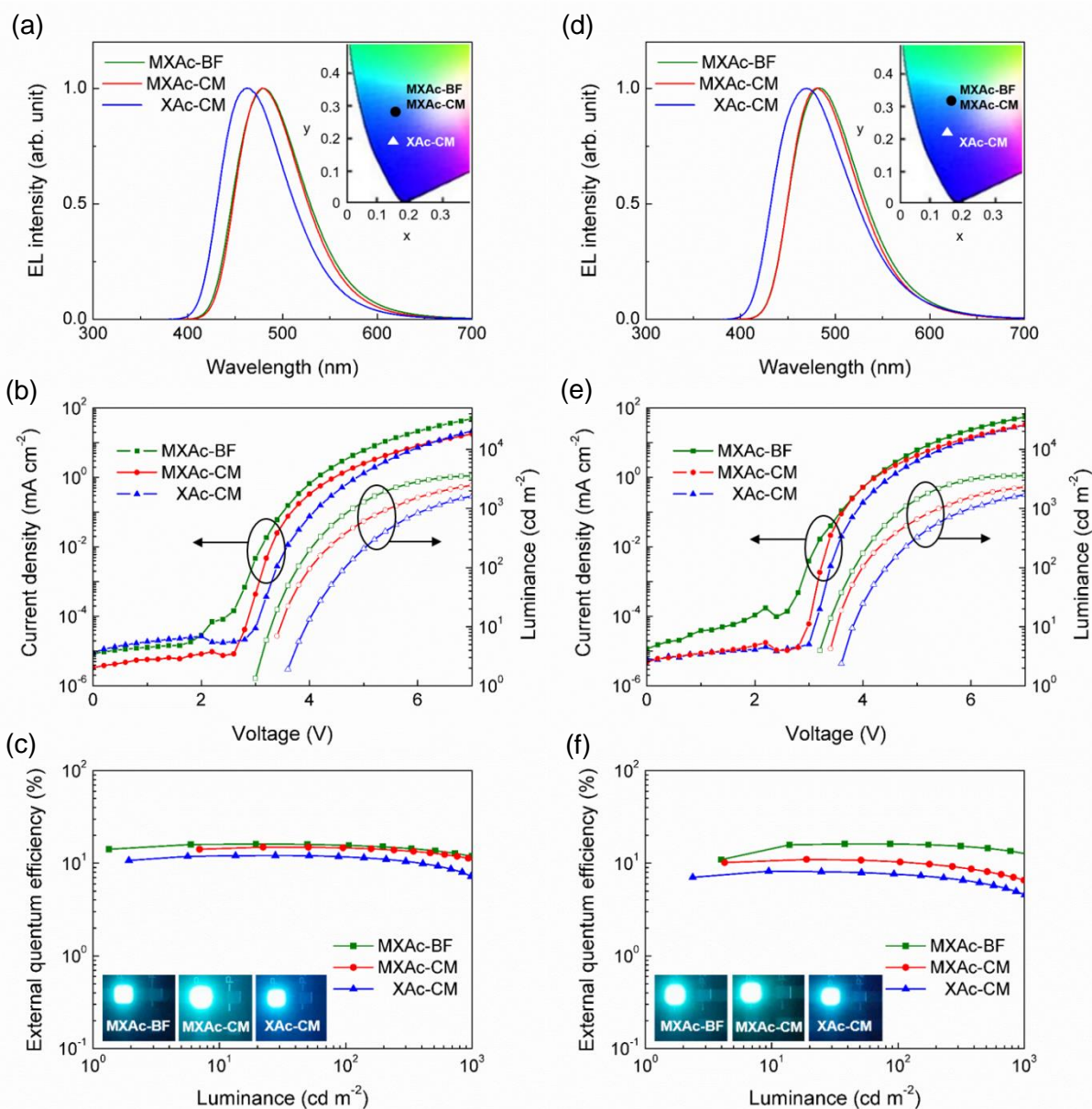| Emitter	Doping conc. (wt%)	$\lambda_{EL}{}^a$ (nm)	$V_{on}{}^b$ (V)	η_{ext} (%)	
				Maximum	at 1000 cd m^{-2}
MXAc-BF	50	479	3.0	16.1	11.9
	100	483	3.2	16.2	12.8
MXAc-CM	50	478	3.4	14.9	11.0
	100	480	3.4	11.0	6.6
XAc-CM	50	462	3.6	12.1	7.2
	100	470	3.6	8.2	4.6

^{a} Maximum EL wavelength. ^{b} Turn-on voltage at 1 cd m^{-2}.

4. 5 Analysis of Efficiency Roll-Off

To examine the origin of improved performance of the BF and CM-based OLEDs with higher η_{ext} values at high current density, exciton annihilation processes in devices employing the sky-blue emitting 1,2-bis(carbazol-9-yl)-4,5-dicyanobenzene (2CzPN)[4] and blue emitting BF and CM-based TADF materials with the same device configuration were investigated. Time-resloved transient PL charactersitics of a 6wt%-2CzPN:PPF doped film were measured to calculate the rate constants using the PL efficiencies and decay times (Figure 4-9). The efficiency roll-off characteristics for all the devices was analyzed by TTA and STA models using the following equations and parameters in Table 4-4.[6b,13]

$$\frac{dN_S}{dt} = -(k_r^s + k_{ISC})N_S + k_{RISC}N_T - k_{STA}N_S N_T + \alpha k_{TTA}N_T^2 + \frac{J}{4de} \tag{4-1}$$

$$\frac{dN_T}{dt} = k_{ISC}N_s - (k_{RISC} + k_{nr}^T)N_T - (1+\alpha)k_{TTA}N_T^2 + \frac{3J}{4de} \tag{4-2}$$

where N_S and N_T are singlet and triplet exciton densities, respectively, α is the singlet exciton production ratio via TTA, d is the thickness of recombination zone, e is the electron charge, and k_{TTA} and k_{STA} are the rate constants of TTA and STA, respectively. For the steady-state current, η_{ext} can be described as following equation.

$$\eta_{ext}(J) = \eta_0 \frac{N_S(t=\infty, J)}{N_{S_0}} \tag{4-3}$$

where, η_0 is the maximum external EL quantum efficiency and N_{S_0} is a singlet exciton density without TTA and STA. Assuming that $d = 10$ nm and $\alpha = 0.25$, the fitted curves (solid lines in Figure 4-10) based on the TTA and STA models are in reasonable agreement with the experimental η_{ext}–J plots, which reveals that TTA and STA exciton deactivation contribute mainly to the efficiency roll-off of these devices. The η_{ext}, current density when η_{ext} reduces to half of the initial η_{ext} (J_0), k_{TTA}, and k_{STA} are complied in Table 4-5. Although all devices were

similar with respect to k_{TTA} and k_{STA}, the BF and CM-based devices showed much larger J_0 (11.3–17.7 mA cm^{-2}) than that of 2CzPN (0.6 mA cm^{-2}), suggesting that the efficiency roll-off at high current density was extremely suppressed in the BF and CM-based devices. Because the exciton density primarily depends on the exciton lifetime in an OLED structure, the fast k_{RISC} originating from relatively shorter TADF lifetimes causes decreased triplet exciton density and lead to suppressed both TTA and STA processes.

Table 4-4. Rate constants of PL decay processes for MXAc-BF, MXAc-CM, XAc-CM, and 2CzPN

compound	Doping conc. (%)	$k_r{}^a$ (10^7 s^{-1})	$k_{ISC}{}^b$ (10^7 s^{-1})	$k_{RISC}{}^c$ (10^5 s^{-1})	$k_{nr}{}^{Td}$ (10^5 s^{-1})
MXAc-BF	50	1.4	2.8	5.7	0.44
	100	1.5	2.7	4.8	0.87
MXAc-CM	50	1.2	1.8	5.4	1.2
	100	1.2	1.9	4.3	1.5
XAc-CM	50	1.5	2.5	3.6	1.2
	100	1.5	2.5	2.6	2.8
2CzPN	6	2.5	3.1	0.05	0.01

^{a}Rate constant of radiative decay (S$_1$→S$_0$). ^{b}Rate constant of ISC (S$_1$→T$_1$). ^{c}Rate constant of RISC (T$_1$→S$_1$). ^{d}Rate constant of nonradiative decay (T$_1$→S$_0$).
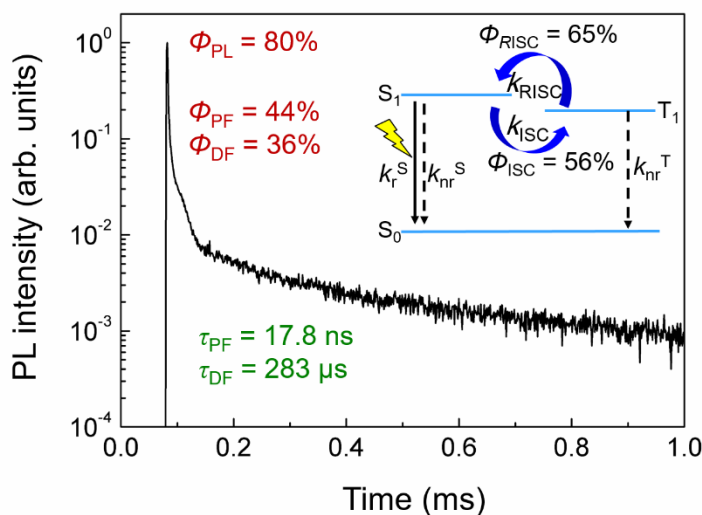
Figure 4-9. Transient PL decay curves of 2CzPN molecules in a PPF solid host matrix at 6 wt% doping concentrations. (inset: PL decay processes for 2CzPN; $k_r{}^s$ and $k_{nr}{}^s$ are the rate constants of radiative and nonradiative decay (S$_1$→S$_0$), $k_{nr}{}^T$ is the rate constant of nonradiative decay (T$_1$→S$_0$), k_{ISC} is the rate constant of ISC (S$_1$→T$_1$), and k_{RISC} is the rate constant of RISC (T$_1$→S$_1$)).
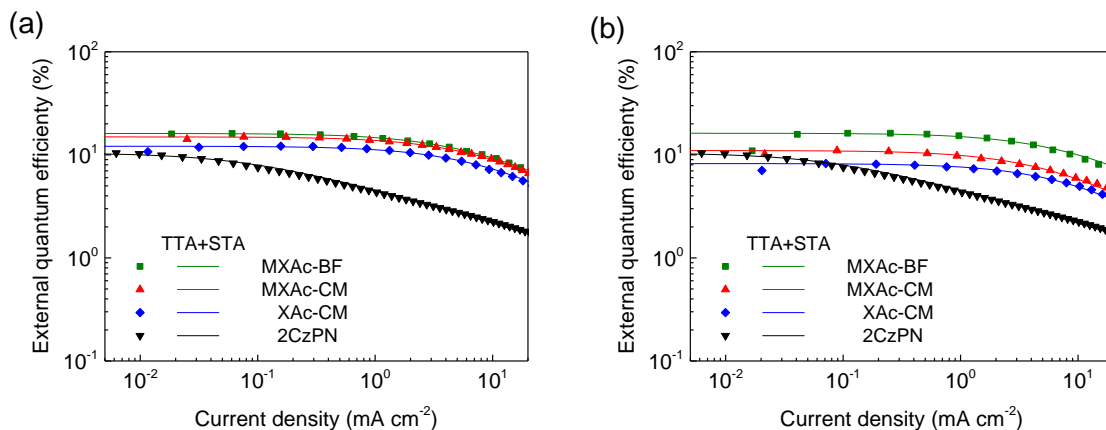
Figure 4-10. External EL quantum efficiency versus current density (η_{ext}–J) characteristics for TADF-OLEDs based on (a) 50 wt%-doped emission layers and (b) non-doped neat (100 wt%) emission layers. The solid lines are the fitting results based on TTA and STA models.

Table 4-5. η_{ext} values, J_0 values, rate constants of TTA, and rate constants of STA, for MXAc-BF, MXAc-CM, XAc-CM, and 2CzPN

compound	Doping conc. (%)	$\eta_{ext,max}$ (%)	$J_0{}^a$ (mA cm^{-2})	$k_{TTA}{}^b$ (10^{-15} cm^{3}s^{-1})	$k_{STA}{}^c$ (10^{-11} cm^3 s^{-1})
MXAc-BF	50	16.1	14.8	11	7.0
	100	16.2	17.7	5.1	7.0
MXAc-CM	50	14.9	16.3	8.0	7.4
	100	11.0	11.3	8.7	11
XAc-CM	50	12.1	16.3	3.9	7.7
	100	8.2	15.5	2.3	15
2CzPN	6	10.4	0.6	2.3	2.1

^{a}Current density when η_{ext} reduces to half of the initial η_{ext}. ^{b}Rate constant of TTA. ^{c}Rate constant of STA.

4. 6 Conclusion

A new family of blue TADF emitters comprised of isobenzofuranone and chromone as acceptor units and spiroacridan as a donor unit, was designed and synthesized. Their small ΔE_{ST} values ranging from 0.08 to 0.11 eV induce fast RISC, leading to short triplet exciton lifetimes (< 4.2 μs). The OLEDs based on these TADF emitters exhibited high maximum external EL quantum efficiencies of up to 16.2% with extremely suppressed efficiency roll-off characteristics even in their heavily doped and non-doped devices. From analysis of efficiency roll-off, the fast RISC for isobenzofuranone and chromone-based TADF emitters significantly suppressed STA and TTA processes. These results open new perspectives for the design of high-performance purely organic blue TADF emitters and devices with reduced efficiency roll-off.

4. 7 Experimental Section

4. 7. 1 Materials and Synthesis
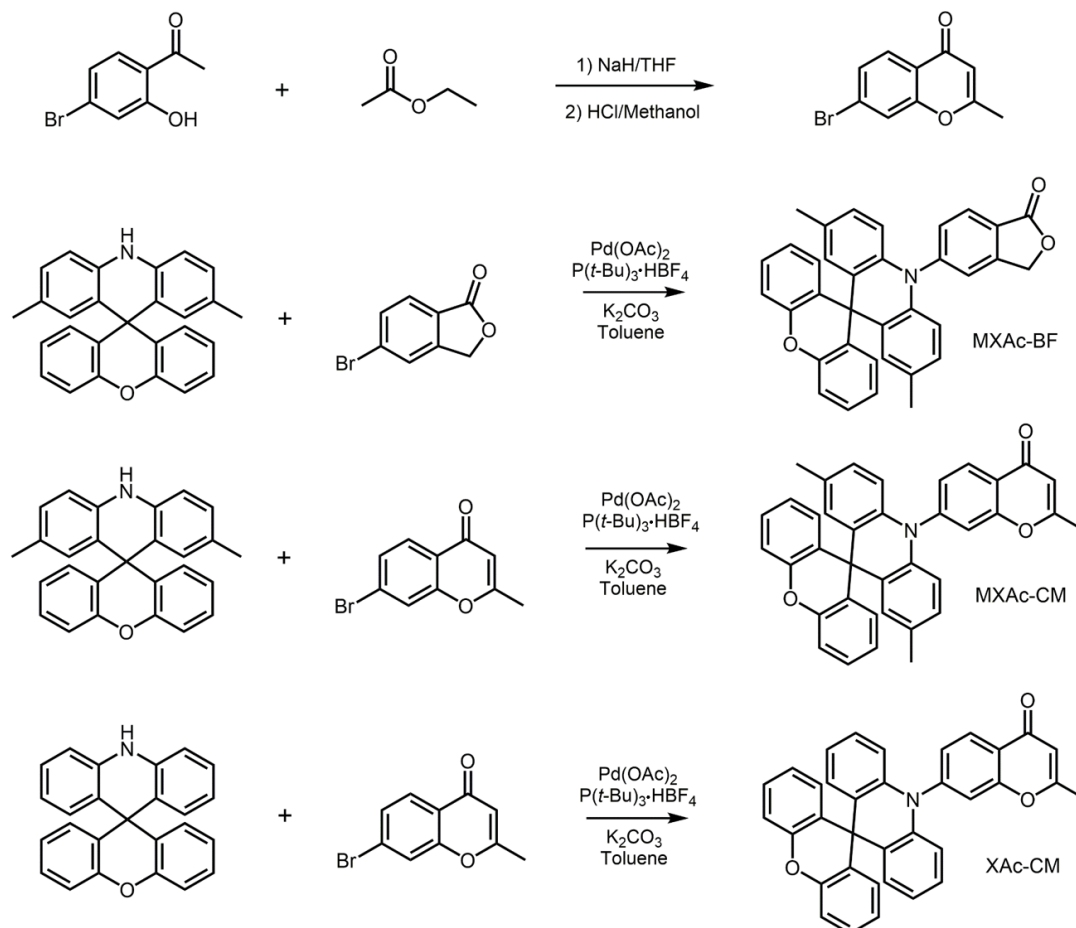
Scheme 4-1. Synthetic routes for 7-bromo-2-methyl-chromone, MXAc-CM, MXAc-CM, and XAc-CM.

All regents and solvents were purchased from Sigma-Aldrich, Tokyo Chemical Industry (TCI), or Wako Pure Chemical Industries, and used as received unless otherwise noted. 7-bromo-2-methyl chromone,[14] 10*H*-spiro[2,7-dimethylacridan-9,9′-xanthene],[5c] 10*H*-spiro[acridan-9,9′-xanthene],[5b] 9-phenyl-3,9'-bicarbazole (CCP),[5b] and 2,8-bis(diphenylphosphoryl)dibenzo[*b,d*]furan (PPF)[15] were prepared according to the literature procedures, and were further purified by temperature-gradient vacuum sublimation. 2,3,6,7,10,11-Hexacyano-1,4,5,8,9,12-hexaazatriphenylene (HAT-CN) was donated by the Nippon Soda Co., Ltd. and was purified by vacuum sublimation before use. Other OLED materials were purchased from E-Ray Optoelectronics Technology Co., Ltd., and were used for the device fabrication without further purification.

NMR spectra were recorded on a Bruker Avance III 500 or III 400 spectrometer. Chemical shifts of ^{1}H and ^{13}C NMR signals were referenced to tetramethylsilane (δ = 0.00), CDCl$_3$ (δ = 77.0), and DMSO-d_6 (δ = 39.5) as internal standards, respectively. Matrix-assisted laser desorption ionization time-of-flight (MALDI-TOF) mass spectra were collected on a Bruker Daltonics Autoflex III spectrometer using dithranol as the matrix. Elemental analysis was performed using a Yanaco MT-5 CHN corder.

Synthesis of 7-bromo-2-methyl-chromone: A mixture of 4-bromo-2-hydroxyacetophenone (5.08 g, 23.6 mmol) and anhydrous ethyl acetate (5.12 g, 58.1 mmol) in dry THF (9.5 mL) was added dropwise to a solution of sodium hydride (60% dispersion in mineral oil, 2.27 g, 94.6 mmol) in dry THF (2.5 mL) under a nitrogen atmosphere. The mixture was stirred for 5 min at room temperature. The reaction mixture was quenched by pouring a large amount of ice water, and then acidified to pH 6 with HCl *aq.* (6M). The solution was extracted with ethyl acetate, and the combined organic layers were washed with water, and dried over anhydrous MgSO$_4$. After filtration and evaporation, a solution of the crude 1-(4-bromo-2-hydroxyphenyl)butane-1,3-dione in methanol (30 mL) was added conc. HCl (36%, 1mL) without further purification. The mixture was stirred for 14 h at room temperature. The reaction mixture was concentrated under reduced pressure. The product was purified by silica gel column chromatography (eluent: ethyl acetate/*n*-hexane = 1:1, v/v), recrystallized from CHCl$_3$/*n*-hexane, and dried under vacuum to afford 7-bromo-2-methyl chromone as a light yellow solid (3.84 g, 68%). ^{1}H NMR (400 MHz, CDCl$_3$): δ 8.04 (d, *J* = 8.4 Hz, 1H), 7.62 (d, *J* = 1.6 Hz, 1H), 7.50 (dd, *J* = 8.4 Hz, 2.0 Hz, 1H), 6.17 (s, 1H), 2.38 (s, 3H). MS (MALDI-TOF): *m/z* [*M*]$^+$ calcd 237.96; found, 238.37.

Synthesis of MXAc-BF: Pd(OAc)$_2$ (0.09 g, 0.40 mmol), P(*t*-Bu)$_3$·HBF$_4$ (0.55 g, 1.90 mmol), and K$_2$CO$_3$ (5.26 g, 38.1 mmol) were added to a solution of 5-bromophthalide (2.70 g, 12.7 mmol) and spiro[2,7-dimethylacridan-9,9′-xanthene] (4.76 g, 12.7 mmol) in dry toluene (150 mL). The mixture was stirred for 5 days at 90 °C. After cooling to room temperature, the reaction mixture was poured into water and then extracted with CHCl$_3$. The combined organic layers were washed with water and dried over anhydrous Na$_2$SO$_4$. After filtration and evaporation, the product was purified by silica gel column chromatography (eluent: CHCl$_3$/ethyl acetate/*n*-hexane = 2:1:7, v/v), recrystallized from CHCl$_3$/*n*-hexane, and dried under vacuum to afford MXAc-BF as a light yellow solid (3.79 g, 59%). This compound was

further purified by temperature-gradient sublimation before use. ^{1}H NMR (500 MHz, DMSO-d_6): δ 8.21 (d, $J = 8.0$ Hz, 1H), 7.89 (d, $J = 0.7$ Hz, 1H), 7.70 (dd, $J = 8.0$ Hz, 1.5 Hz, 1H), 7.26–7.22 (m, 4H), 7.10 (dd, $J = 7.8$ Hz, 1.0 Hz, 2H), 7.03 (td, $J = 7.0$ Hz, 2.2 Hz, 2H), 6.73 (dd, $J = 8.6$ Hz, 1.7 Hz, 2H), 6.47 (d, $J = 1.7$ Hz, 2H), 6.12 (d, $J = 8.5$ Hz, 2H), 5.56 (s, 2H), 1.95 (s, 6H). ^{13}C NMR (125 MHz, CDCl$_3$): δ 170.05, 149.40, 148.48, 147.55, 136.63, 132.88, 132.79, 131.79, 131.22, 130.48, 129.71, 128.67, 127.89, 127.61, 125.67, 125.61, 123.64, 116.01, 113.73, 69.36, 44.63, 20.47. MS (MALDI-TOF): m/z [M]$^+$ calcd 507.18; found, 507.21. Anal. Calcd (%) for C$_{38}$H$_{25}$NO$_2$: C, 82.82; H, 4.96; N, 2.76; found: C, 82.74; H, 4.93; N, 2.82.

Synthesis of MXAc-CM: Pd(OAc)$_2$ (0.03 g, 0.13 mmol), P(t-Bu)$_3$·HBF$_4$ (0.18 g, 0.62 mmol), and K$_2$CO$_3$ (1.73 g, 12.5 mmol) were added to a solution of 7-bromo-2-methyl-chromone (1.00 g, 4.18 mmol) and spiro[2,7-dimethylacridan-9,9′-xanthene] (1.57 g, 4.18 mmol) in dry toluene (50 mL). The mixture was stirred for 5 days at 90 °C. After cooling to room temperature, the reaction mixture was poured into water and then extracted with CHCl$_3$. The combined organic layers were washed with water and dried over anhydrous Na$_2$SO$_4$. After filtration and evaporation, the product was purified by silica gel column chromatography (eluent: CHCl$_3$/ethyl acetate/n-hexane = 2:1:5, v/v), recrystallized from CHCl$_3$/n-hexane, and dried under vacuum to afford MXAc-CM as a light yellow solid (1.16 g, 52%). This compound was further purified by temperature-gradient sublimation before use. ^{1}H NMR (500 MHz, DMSO-d_6): δ 8.36 (d, $J = 8.3$ Hz, 1H), 7.91 (d, $J = 1.8$ Hz, 1H), 7.56 (dd, $J = 8.3$ Hz, 1.9 Hz, 1H), 7.26–7.21 (m, 4H), 7.13 (dd, $J = 7.8$ Hz, 1.1 Hz, 2H), 7.03 (td, $J = 7.1$ Hz, 2.0 Hz, 2H), 6.73 (dd, $J = 8.6$ Hz, 1.6 Hz, 2H), 6.47 (d, $J = 1.7$ Hz, 2H), 6.39 (d, $J = 0.5$ Hz, 1H), 6.15 (d, $J = 8.5$ Hz, 2H), 2.46 (s, 3H), 1.95 (s, 6H). ^{13}C NMR (125 MHz, CDCl$_3$): δ 177.55, 166.53, 158.09, 148.47, 146.52, 136.54, 132.69, 131.85, 131.25, 130.36, 129.65, 128.69, 128.27, 127.89, 127.56, 123.66, 123.41, 120.99, 115.95, 113.81, 110.99, 44.63, 20.63, 20.48. MS (MALDI-TOF): m/z [M]$^+$ calcd 533.20; found, 532.90. Anal. Calcd (%) for C$_{38}$H$_{23}$NO$_2$: C, 83.28; H, 5.10; N, 2.62; found: C, 83.36; H, 5.02; N, 2.66.

Synthesis of XAc-CM: Pd(OAc)$_2$ (0.03 g, 0.13 mmol), P(t-Bu)$_3$·HBF$_4$ (0.18 g, 0.62 mmol), and K$_2$CO$_3$ (1.39 g, 10.1 mmol) were added to a solution of 7-bromo-2-methyl-chromone (1.00 g, 4.18 mmol) and spiro[acridane-9,9′-xanthene] (1.74 g, 5.01 mmol) in dry toluene (50 mL). The mixture was stirred for 5 days at 90 °C. After cooling to room temperature, the reaction mixture was poured into water and then extracted with CHCl$_3$. The combined organic layers

were washed with water and dried over anhydrous Na_2SO_4. After filtration and evaporation, the product was purified by silica gel column chromatography (eluent: ethyl acetate/*n*-hexane = 1:2, v/v), recrystallized from CH_2Cl_2/methanol, and dried under vacuum to afford XAc-CM as a light yellow solid (1.05 g, 50%). This compound was further purified by temperature-gradient sublimation before use. ^{1}H NMR (500 MHz, DMSO-d_6): δ 8.38 (d, J = 8.3 Hz, 1H), 7.99 (d, J = 1.9 Hz, 1H), 7.62 (dd, J = 8.3 Hz, 1.9 Hz, 1H), 7.26–7.22 (m, 4H), 7.14 (dd, J = 8.0 Hz, 1.3 Hz, 2H), 7.03 (td, J = 6.9 Hz, 2.3 Hz, 2H), 6.93 (td, J = 7.1 Hz, 2.8 Hz, 2H), 6.74-6.70 (m, 4H), 6.40 (s, 1H), 6.24 (d, J = 8.3 Hz, 2H). ^{13}C NMR (125 MHz, $CDCl_3$): δ 177.48, 166.59, 158.13, 148.48, 145.94, 138.44, 132.54, 131.80, 131.19, 129.86, 128.85, 128.21, 127.70, 127.04, 123.68, 123.59, 121.45, 120.98, 116.03, 113.93, 111.03, 44.64, 20.64. MS (MALDI-TOF): m/z $[M]^+$ calcd 505.17; found, 504.99. Anal. Calcd (%) for $C_{29}H_{23}NO_2$: C, 83.15; H, 4.59; N, 2.77; found: C, 83.11; H, 4.56; N, 2.80.

4. 7. 2 Quantum Chemical Calculations

Density functional theory (DFT) calculations were performed using the Gaussian 09 program package. The molecular geometries in the ground state were optimized using the PBE1PBE functional with the 6-31G(d) basis set in the gas phase. The lowest singlet and triplet excited states were computed using the optimized structures with time-dependent DFT (TD-DFT) at the same level.

4. 7. 3 Photophysical Characterizations

Organic thin films for photophysical measurements were prepared by vacuum deposition under high vacuum (~7×10^{-5} Pa) onto quartz glass or Si(100) substrates. UV–vis absorption and photoluminescence (PL) spectra were measured with a JASCO V-670 spectrometer and a JASCO FP-8600 spectrophotometer, respectively, using degassed spectral grade solvents. The absolute PL quantum yields (Φ_{PL}) were determined using a JASCO ILF-835 integrating sphere system by photoexcitation of 290 nm. The transient PL characteristics of doped thin films were performed using a Hamamatsu Photonics C11367 Quantaurus-tau fluorescence lifetime spectrometer (λ_{ex} = 340 nm, pulse width = 100 ps, repetition rate = 20 Hz) under N_2, and a Hamamatsu Photonics C9300 streak camera with an N_2 gas laser (λ_{ex} = 337 nm, pulse width = 500 ps, and repetition rate = 20 Hz) under vacuum ($< 4\times10^{-1}$ Pa). The HOMO energy levels of the materials in thin films were determined using a Riken-Keiki AC-2 ultraviolet photoelectron spectrometer. The LUMO energy levels were estimated by subtracting the optical energy gap

(E_g) from the measured HOMO energies; E_g values were determined from the high-energy onset position of the PL spectra of thin films.

4. 7. 4 OLED Fabrication and Measurements

Indium tin oxide (ITO)-coated glass substrates were cleaned with detergent, deionized water, acetone, and isopropanol. The substrates were then subjected to UV–ozone treatment for 30 min before they were loaded into a vacuum evaporation system. The organic layers and a cathode aluminum layer were thermally evaporated on the substrates under vacuum ($< 6 \times 10^{-5}$ Pa) with an evaporation rate of < 0.3 nm s^{-1} through a shadow mask. The layer thickness and deposition rate were monitored in situ during deposition by an oscillating quartz thickness monitor. OLED characteristics were measured using a Keithley 2400 source meter and a Konica Minolta CS-2000 spectroradiometer.

References

[1]   a) Y. Sun, N. C. Giebink, H. Kanno, B. Ma, M. E. Thompson, S. R. Forrest, *Nature* **2006**, *440*, 908; b) S. Reineke, F. Lindner, G. Schwartz, N. Seidler, K. Walzer, B. Lüssem. K. Leo, *Nature* **2009**, *459*, 234.

[2]   a) C. Adachi, M. A. Baldo, S, R Forrest, M. E. Thompson, *Appl. Phys. Lett.* **2000**, *77*, 904; b) S.-Y. Kim, W.-I. Jeong, C. Mayr, Y.-S. Park, K.-H. Kim, J.-H. Lee, C.-K. Moon, W. Brütting, J.-J. Kim, *Adv. Funct. Mater.* **2013**, *23*, 3896; c) Y.-S. Park, S. Lee, K.-H. Kim, S.-Y. Kim, J.-H. Lee, J.-J. Kim, *Adv. Funct. Mater.* **2013**, *23*, 4914.

[3]   a) Y. Chi, P.-T. Chou, *Chem. Soc. Rev.* **2010**, *39*, 638; b) H. Xu, R. Chen, Q. Sun, W. Lai, Q. Su, W. Huang, X. Liu, *Chem. Soc. Rev.* **2014**, *43*, 3259.

[4]   H. Uoyama, K. Goushi, K. Shizu, H. Nomura, C. Adachi, *Nature* **2012**, *492*, 234.

[5]   a) Q. Zhang, B. Li, S. Huang, H. Nomura, H. Tanaka, C. Adachi, *Nat. Photonics* **2014**, *8*, 326; b) M. Numata, T. Yasuda, C. Adachi, *Chem. Commun.* **2015**, *51*, 9443; c) I. S. Park, H. Komiyama, T. Yasuda, *Chem. Sci.* **2016**, *7*, in press; d) I. S. Park, J. Lee, T. Yasuda, *J. Mater. Chem. C* **2016**, *4*, 7911; e) T. Hakakeyama, K. Shiren, K. Nakajima, S. Nomura, S. Nakatuaka, K. Kinoshita, J. Ni, Y. Ono, T. Ikuta, *Adv. Mater.* **2016**, *28*, 2777.

[6]   a) S. Y. Lee, T. Yasuda, H. Nomura, C. Adachi, *Appl. Phys. Lett.* **2012**, *101*, 093306; b) K. Masui, H. Nakanotani, C. Adachi, *Org. Electron.* **2013**, *14*, 2721.

[7]   a) I. Cerskus, R.B. Philp, *Agents Actions* **1981**, *11*, 281; b) Y.-P. Wang, Y.-L. Wei, C. Dong, *J. Photochem. Photobiol. A: Chem.* **2006**, *117*, 6; c) J. Safari, H. Naeimi, A.A. Khakpour, R.S. Jondani, S.D.A. Khalili, *J. Mol. Catal. A: Chem.* **2007**, *270*, 236.

[8]   M. Shanmugasundaram, J. Joseph, D. Ramaiah, *J. Photochem. Photobiol. A: Chemistry* **2016**, *330*, 156.

[9]   S. Yang, A. Elangovan, T. Ho, *Photochem. Photobiol. Sci.* **2005**, *4*, 327.

[10]   J. Lee, N. Aizawa, M. Numata, C. Adachi, T. Yasuda, *Adv. Mater.* **2016**, *28*, in press. DOI: 10.1002/adma.201604856

[11]   P. A. Vecchi, A. B. Padmaperuma, H. Qiao, L. S. Sapochak, P. E. Burrows, *Org. Lett.* **2006**, *8*, 42.

[12]   a) Q. Zhang, J. Li, K. Shizu, S. Huang, S. Hirata, H. Miyazaki, C. Adachi, *J. Am. Chem. Soc.* **2012**, *134*, 14706; b) S. Wu, M. Aonuma, Q. Zhang, S. Huang, T. Nakagawa, K. Kuwabara, C. Adachi, *J. Mater. Chem. C* **2014**, *2*, 421; c) W. Liu, C.-J. Zhang, K. Wang, Z. Chen, D.-Y. Chen, F. Li, X.-M. Ou, Y.-P. Dong, X.-H. Zhang, *ACS Appl. Mater.*

Interfaces **2015**, *7*, 18930; d) X. Cai, B. Gao, X.-L. Li, Y. Cao, S.-J. Su, *Adv. Funct. Mater.* **2016**, *26*, 8042; e) Y. J. Cho, S. K. Jeon, S.-S. Lee, E. Yu, J. Y. Lee, *Chem. Mater.* **2016**, *28*. 5400.

[13]   M. Inoue, T. Serevičius, H. Nakanotani, K. Yoshida, T. Matsushima, S. Jursenas, C. Adachi, *Chem. Phys. Lett.* **2016**, 644, 62.

[14]   D. Zhao, B. Beiring, F. Glorius, *Angew. Chem. Int. Ed.* **2013**, *52*, 8454.

Chapter 5

Oxadiazole- and Triazole-Based Thermally Activated Delayed Fluorescence Materials for Efficient Blue and Green Organic Light-Emitting Diodes
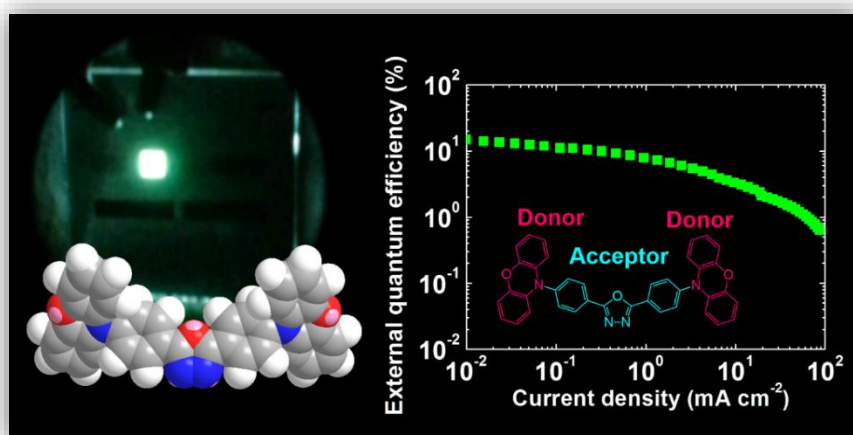
5. 1 Introduction

An important factor in designing molecules with a small energy difference (ΔE_{ST}) between the lowest excited singlet (S_1) and triplet (T_1) states is control of the spatial overlap between the highest occupied molecular orbital (HOMO) and the lowest unoccupied molecular orbital (LUMO). Because the HOMO and LUMO tend to be distributed over electron-donating and -accepting moieties, respectively, by combining suitable electron-donating and -accepting groups, the HOMO and LUMO distributions in a molecule can be separated. Using steric hindrance to twist a molecule is also an effective way to spatially separate its HOMO and LUMO. By incorporating a structural twist into a suitable donor–acceptor (D–A) system, a TADF emitter (PXZ-TRZ) with ΔE_{ST} ~0 eV has been reported.[1]

Oxadiazole and phenoxazine derivatives have been used extensively as fluorescent emitters for OLEDs.[2–4] However, because these materials are conventional fluorescent emitters rather than TADF ones, external electroluminescence (EL) quantum efficiencies (η_{ext}) obtained for their devices are less than those of phosphorescent OLEDs. In these fluorescent compounds, the large overlap between HOMO and LUMO is probably a major factor preventing the generation of TADF.

In this chapter, the author reports TADF emitters with the D–A–D or D–A electronic structure by appending electron-accepting groups into the nitrogen atom of phenoxazine. The strong electron-accepting ability of oxadiazole or triazole and the electron-donating ability of phenoxazine lead to a small ΔE_{ST}, and as such, effective $T_1 \rightarrow S_1$ up conversion. An OLED using D–A–D-type molecule as an emitter exhibited high η_{ext} of 14.9%, which exceeds those obtained with common fluorescent emitters.

5. 2 Molecular Design and Quantum Chemical Calculations

The electron accepting units 1,3,4-oxadiazole and 1,2,4-triazole are well-known for their electron-transporting abilities and have been widely used as building blocks to develop electron-transporting materials for OLEDs.[5–7] Because 1,2,4-triazole has a deep LUMO energy level, it has also been used to develop bipolar host materials for phosphorescent OLEDs.[8,9] Phenoxazine is potentially a good electron donor and hence has been used for hole injection materials in OLEDs.[10] Phenoxazine-based compounds have also been used as dyes in dye-sensitized solar cells,[11] laser dyes,[12] and fluorescent stains.[13,14] A new class of D–A–D or D–A molecules containing 2,5-diphenyl-1,3,4-oxadiazole (OXD) or 3,4,5-triphenyl-1,2,4-

triazole (TAZ) as an acceptor and phenoxazine (PXZ) as a donor was designed as shown in Figure 5-1.
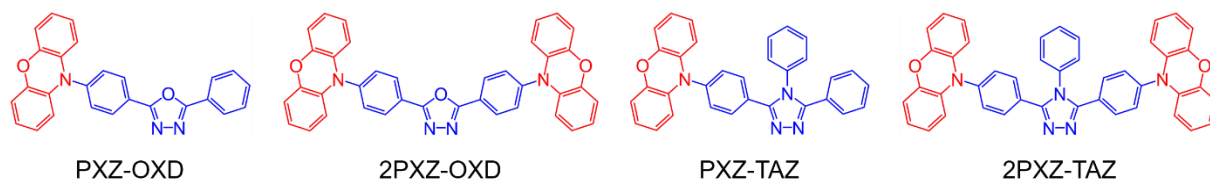

| PXZ-OXD | 2PXZ-OXD | PXZ-TAZ | 2PXZ-TAZ |

Figure 5-1. Molecular structures for PXZ-OXD, 2PXZ-OXD, PXZ-TAZ, and 2PXZ-TAZ.

To investigate the origin of $T_1 \rightarrow S_1$ up conversion in the TADF emitters, quantum chemical calculations based on density functional theory (DFT) were performed. Absorption and emission wavelengths for the four compounds in toluene solution were computed with time-dependent density functional theory (TD-DFT)[15,16] and the CAM-B3LYP/cc-pVDZ method[17,18] using the polarizable continuum model.[19–21] The calculated absorption and emission wavelengths are in reasonable agreement with experimental values, as shown in Table 5-1. Therefore, the CAM-B3LYP/cc-pVDZ method describes the excited states of the compounds well. In the following, the theoretical results were obtained from gas-phase calculations at the CAM-B3LYP/cc-pVDZ level of theory.

Figure 5-2 shows the highest occupied and the lowest unoccupied natural transition orbitals (NTOs) for the S_1 state of the compounds calculated with the TD-DFT method using the optimized ground-state molecular geometry. The highest occupied NTO are largely localized on the two phenoxazine moieties, whereas the lowest unoccupied NTO are localized on the OXD (or TAZ) moieties, resulting in a limited overlap between the two NTOs. This small overlap is caused by the strong electron-donating and -accepting abilities of phenoxazine and OXD (or TAZ), respectively. The calculated twisting angle (74.9°) is in good agreement with the experimental value of 76.7° obtained from X-ray diffraction patterns (Figure 5-3). This large dihedral angle also plays an important role in separating the HOMO and LUMO of 2PXZ-OXD. The small spatial overlap between the highest occupied and the lowest unoccupied NTOs is also realized for PXZ-OXD, PXZ-TAZ and 2PXZ-TAZ. The small spatial overlap between the frontier orbitals leads to a weak exchange interaction and consequently to the smallest ΔEST among the four compounds (Table 5-2). The efficient $T_1 \rightarrow S_1$ up conversion in 2PXZ-OXD is attributed to its small ΔE_{ST}.

Table 5-1. Calculated and experimental absorption and emission wavelengths for PXZ-OXD, 2PXZ-OXD, PXZ-TAZ, and 2PXZ-TAZ

Compound	λ_{abs} (nm)		λ_{em} (nm)	
	Calc.	Exp.	Calc.	Exp.
PXZ-OXD	416	390	513	495
2PXZ-OXD	439	397	525	502
PXZ-TAZ	366	372	428	455
2PXZ-TAZ	370	376	438	462

Absorption (λ_{abs}) and emission wavelengths (λ_{em}) were computed using time-dependent density functional theory (TD-DFT) at the CAM-B3LYP/cc-pVDZ level of theory. Solvent effects were taken into account by means of the polarizable continuum model.

Highest occupied NTO   Lowest unoccupied NTO
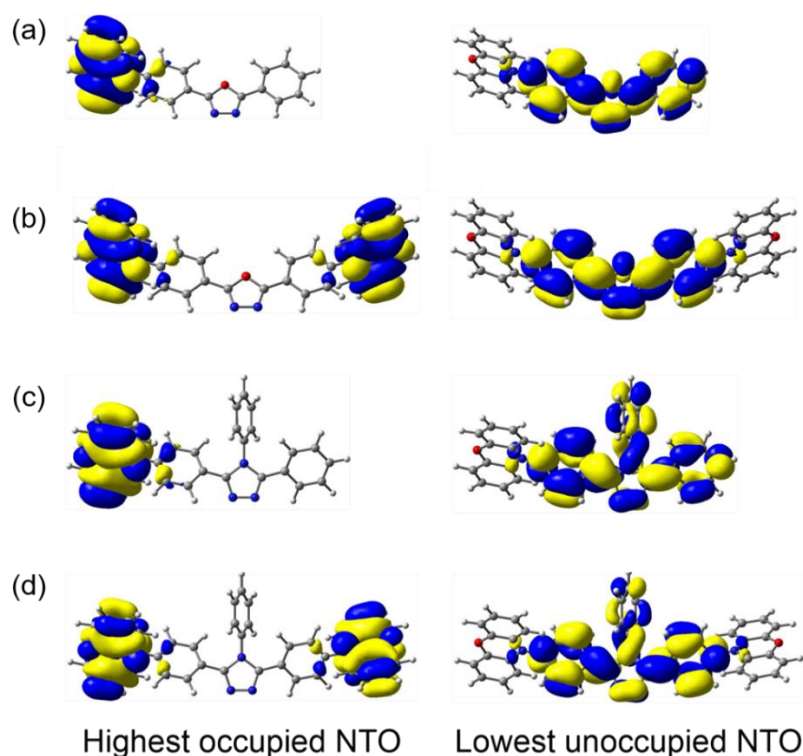
Figure 5-2. Highest occupied and lowest unpccupied natural transition orbitals for S_1 of (a) PXZ-OXD, (b) 2PXZ-OXD, (c) PXZ-TAZ, and (d) 2PXZ-TAZ calculated at the TD-DFT-CAM-B3LYP/cc-pVDZ//CAM-B3LYP/cc-pVDZ level of theory.
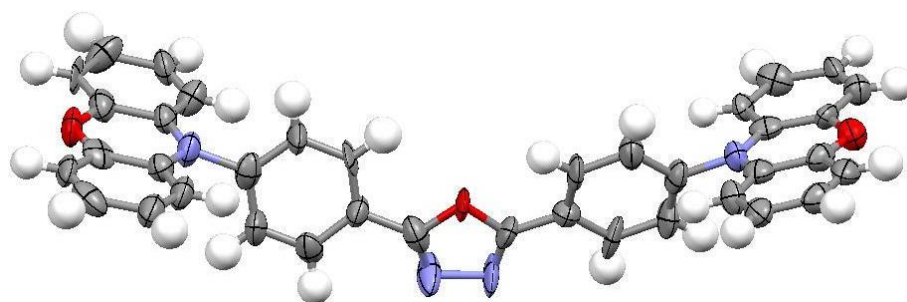

Figure 5-3. ORTEP diagram of the molecular structure of 2PXZ-OXD determined by single crystal X-ray diffraction. The torsion angle is 76.7°.

Table 5-2. Calculated S_1 and T_1 excitation energies and ΔE_{ST} of PXZ-OXD, 2PXZ-OXD, PXZ-TAZ, and 2PXZ-TAZ

Compound	S_1 energy (eV)	T_1 energy (eV)	ΔE_{ST} (eV)
PXZ-OXD	3.49 (0.0001)	2.84	0.65
2PXZ-OXD	3.40 (0.0000)	2.83	0.57
PXZ-TAZ	3.80 (0.0000)	2.83	0.97
2PXZ-TAZ	3.69 (0.0000)	2.83	0.86

Calculation of ΔE_{ST} was carried out with TD-DFT at the CAM-B3LYP/cc-pVDZ level of theory. Oscillator strengths (*f*) of the S_1 states shown in parentheses.

5. 3 Photophysical and TADF Properties

To investigate the luminescent properties of the four compounds, photoluminescence (PL) quantum efficiencies (Φ_{PL}) were compared in toluene solution in air and those in the absence of oxygen (Table 5-3). UV–vis absorption and PL spectra are shown in Figure 5-4. For all the compounds, Φ_{PL} increased after nitrogen bubbling, suggesting that quenching of triplet states by oxygen occurred in air, and was suppressed by nitrogen bubbling. For PXZ-OXD, 2PXZ-OXD, and 2PXZ-TAZ, the observation of both short (in the order of 1–10 ns) and long (in the order of 1–10 μs) lifetime components after nitrogen bubbling shows that these molecules emit both normal and delayed fluorescence in the absence of oxygen. In contrast, only short-lived components were observed in air. Observation of the Φ_{PL} and fluorescence lifetimes of these compounds reveals that nitrogen bubbling suppresses oxygen quenching of the excited triplet states, leading to increased delayed fluorescence and consequently, increased Φ_{PL}.

In the absence of oxygen, 2PXZ-OXD with a D–A–D-type structure exhibits a higher Φ_{PL} (43.1%) than PXZ-OXD with a D–A-type structure (29.8%). The larger increase in Φ_{PL} caused by nitrogen bubbling for 2PXZ-OXD (43.1% − 19.9% = 23.2%) than that for PXZ-OXD (29.8% − 18.1% = 11.7%) shows that 2PXZ-OXD exhibits more effective $T_1{\rightarrow}S_1$ up conversion than PXZ-OXD. 2PXZ-TAZ and PXZ-TAZ also showed a similar trend, although their Φ_{PL} were low compared with those of 2PXZ-OXD and PXZ-OXD. These observations suggest that D–A–D-type structures can emit more total fluorescence (normal and delayed fluorescence) than D–A-type structures in the absence of oxygen. 2PXZ-OXD exhibits a higher Φ_{PL} than highly-efficient TADF emitter PXZ-TRZ, with D–A-type structure.[1] Thus, improved Φ_{PL} were successfully achieved by developing TADF materials with D–A–D-type structures. These findings provide a guideline for molecular design to enhance the Φ_{PL} of TADF emitters.

Theoretical calculations can provide insight into the relative efficiency of $T_1{\rightarrow}S_1$ up conversion. As listed in Table 5-2, the D–A–D-type compounds have smaller ΔE_{ST} than the D–A-type compounds, which explains the experimental observation that the D–A–D-type

compounds display more efficient $T_1 \rightarrow S_1$ up conversion than the D–A-type ones. As mentioned above, oxadiazole derivatives exhibit a larger increase in Φ_{PL} than triazole derivatives when oxygen is removed from the system. This is because the oxadiazole derivatives have smaller ΔE_{ST} than the triazole ones. The relative order of the calculated ΔE_{ST} is consistent with that of the increase in Φ_{PL} caused by nitrogen bubbling. Thus, the calculated ΔE_{ST} readily explain the relative efficiency of $T_1 \rightarrow S_1$ up conversion. Radiative decay rate from the S_1 state is often related to the oscillator strength of the state (f): molecules with large f show a high Φ_{PL}. However, this is not true for our TADF compounds. For example, 2PXZ-OXD (smaller f) exhibits a higher Φ_{PL} than PXZ-OXD (larger f). This result suggests that non-radiative decay has a non-negligible impact on the Φ_{PL} of these compounds. It is probable that the order of the Φ_{PL} is controlled by not only oscillator strengths, but also by competitive vibronic couplings causing non-radiative decay.
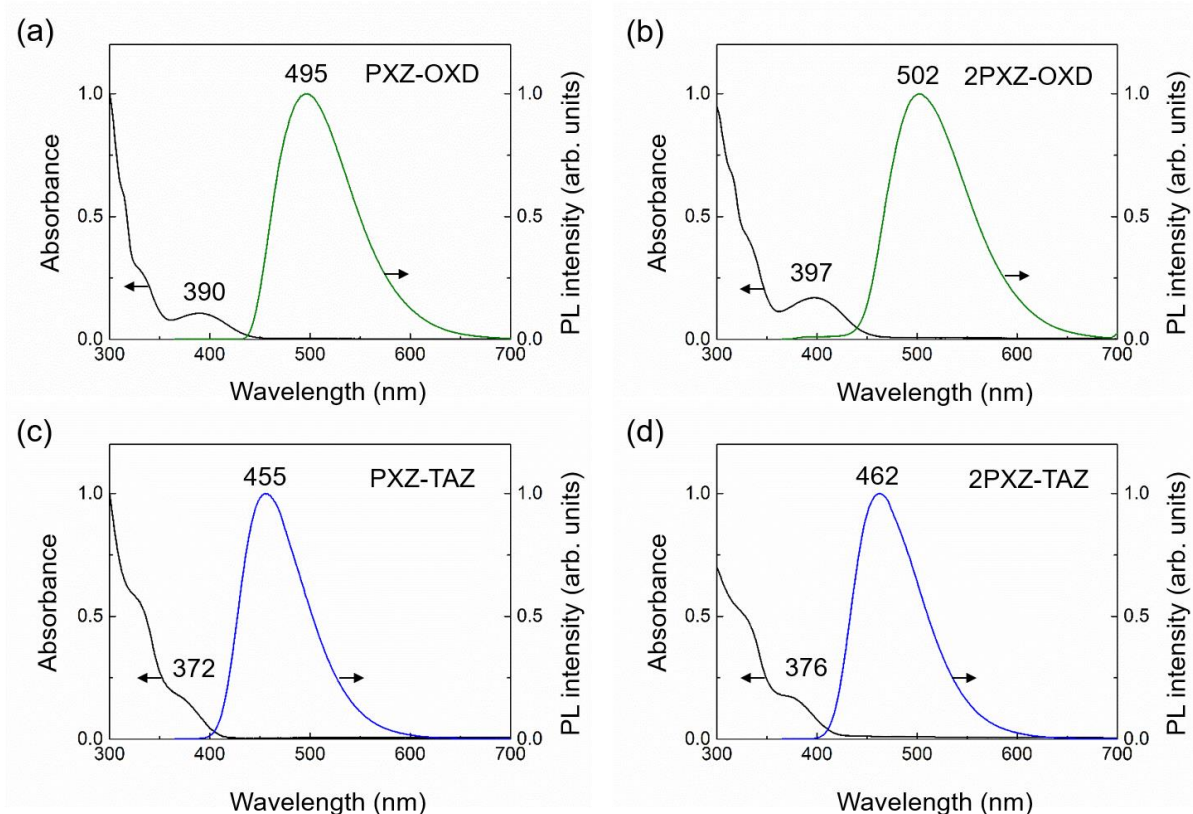

Figure 5-4. Uv–vis absorption and PL spectra of (a) PXZ-OXD, (b) 2PXZ-OXD, (c) PXZ-TAZ, and (d) 2PXZ-TAZ in toluene at room temperature.

Table 5-3. PL properties of PXZ-OXD, 2PXZ-OXD, PXZ-TAZ, and 2PXZ-TAZ in toluene solution

Compound	Φ_{PL} (%)	τ_{PF} (ns)	τ_{DF} (μs)	Φ_{PL} (%)	τ_{PF} (ns)	τ_{DF} (μs)
PXZ-OXD	18.1	7.39	n.d.	29.8	11.01	4.73
2PXZ-OXD	19.1	8.93	n.d.	43.1	21.25	13.27
PXZ-TAZ	10.3	2.51	n.d.	12.7	2.85	0.016
2PXZ-TAZ	10.6	2.97	n.d.	15.2	3.28	28.88

τ_{PF} and τ_{DF} are lifetimes of prompt and delayed components, respectively. The delayed components were not observed in air.

To evaluate the efficiency of delayed fluorescence of 2PXZ-OXD and 2PXZ-TAZ in a host material, doped films of the 2PXZ-OXD and 2PXZ-TAZ emitters in a bis[2-(diphenylphosphino)phenyl]ether oxide (DPEPO) film were prepared by vaccum codeposition. The 6 wt% 2PXZ-OXD-doped films showed the PL emission centerd at 517 nm. The Φ_{PL} values of 2PXZ-OXD in the doped films reached $87 \pm 3\%$. Therefore, T_1 excitons of 2PXZ-OXD are well confined using the DPEPO host because the T_1 energy level of DPEPO (3.0 eV)[22] is much higher than the S_1 level of 2PXZ-OXD (2.40 eV).

Figure 5-5 shows the transient PL decay curves measured for the doped film of 2PXZ-OXD and 2PXZ-TAZ using streak camera. The intense emission is ascribed to a prompt fluorescent component, and the long tails are the delayed components. From the transient PL decay curve, the lifetimes for the prompt and delayed components at 300 K were estimated to be 11.23 ns and 0.52 μs, respectively. Contributions from the prompt (Φ_{PF}) and delayed components (Φ_{DF}) to the total Φ_{PL} were determined to be 76.6% and 10.4%, respectively. The fact that the intensity of the delayed component increases with increasing temperature 8 to 200 K (Figure 5-5a) shows that the delayed component originates from TADF. From the blue edges of fluorescence and phosphorescence shown in Figure 5-6a, ΔE_{ST} was determined to be 0.15 eV. Although the T_1 state becomes emissive when cooling from room temperature to low temperature, because the phosphorescence is weak, the PL spectra does not show a bathochromic shift (Figure 5-7). Interestingly, the delayed component of the transient decay in Figure 5-5a decreased with increasing temperature over 200 K. 2PXZ-TAZ showed transient PL characteristics similar to those of 2PXZ-OXD (Figure 5-5a). From transient PL measurements, 2PXZ-TAZ was found to emit sky-blue light with PL peaks centerd at 467 nm. The delayed component ($\Phi_{DF} = 20.2\%$) was twice that for 2PXZ-OXD. However, because the prompt component ($\Phi_{PF} = 31.8\%$) is small, the total Φ_{PL} ($52\pm3\%$) is lower than that for 2PXZ-OXD ($87\pm3\%$). The lifetime for the delayed component was determined to be 2.09 μs, which was four times longer than that for

2PXZ-OXD. From the fluorescence and phosphorescence spectra measured at 8 K (Figure 5-6b), ΔE_{ST} was determined to be 0.23 eV, which was larger than that of 2PXZ-OXD. Assuming that spin-orbit couplings of 2PXZ-TAZ and 2PXZ-OXD are comparable, it is probable that the larger ΔE_{ST} of 2PXZ-TAZ leads to a lower rate of reveerse intersystem crossing and consequently, a longer τ_{DF} than that of 2PXZ-OXD.

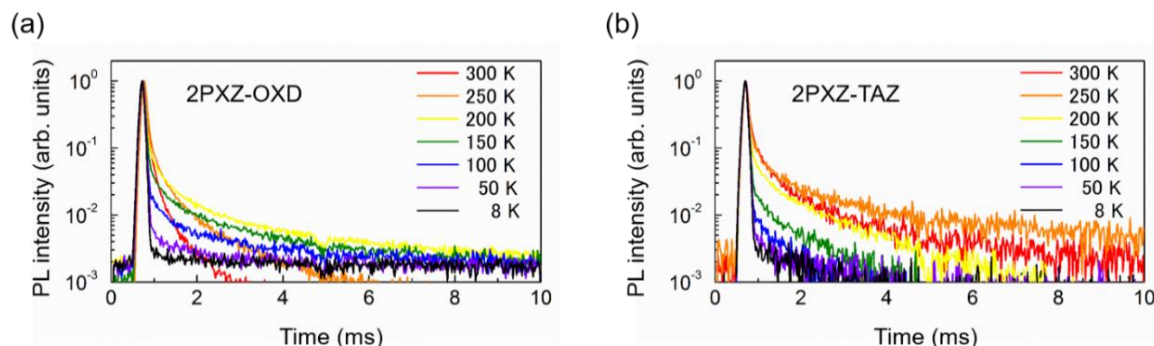**Figure 5-5.** Temperature dependence of transient PL decay curves ranging from 8 to 300 K for (a) 6 wt%-2PXZ-OXD:DPEPO and (b) 6 wt%-2PXZ-TAZ:DPEPO doped films.
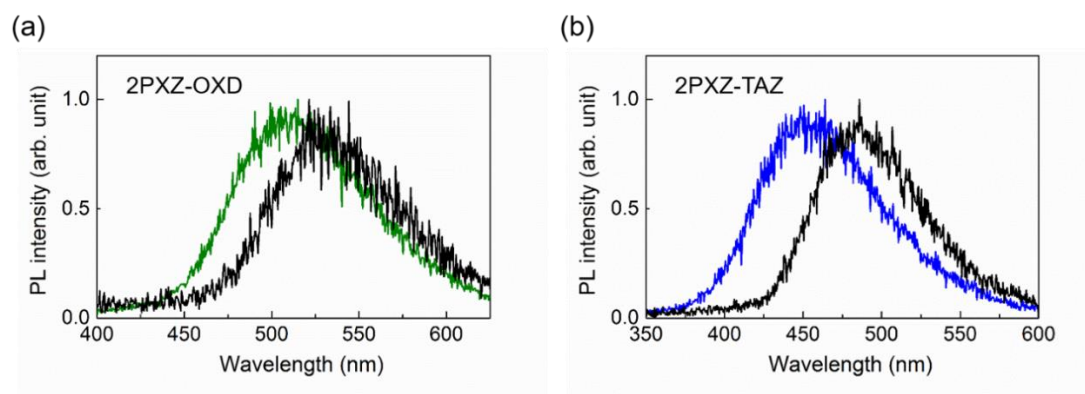

Figure 5-6. Fluorescence spectra (green and blue lines) and phosphorescence spectra at 8 K (black lines) for (a) 6 wt%-2PXZ-OXD:DPEPO and (b) 6 wt%-2PXZ-TAZ:DPEPO doped films.
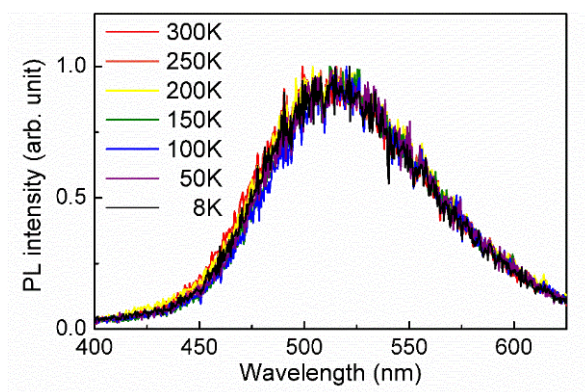

Figure 5-7. Temperature dependence of PL spectrum of 6wt%-2PXZ-OXD:DPEPO doped film.

5. 4 Electroluminescence Performance

To evaluate the potential of 2PXZ-OXD and 2PXZ-TAZ in OLEDs, OLEDs were fabricated with the following device configuration: indium-thin-oxide (ITO, 100nm)/α-NPD (30nm)/mCP (10nm)/6 wt% TADF emitter:DPEPO (15 nm)/DPEPO (10nm)/TPBi (40 nm)/LiF (0.8 nm)Al (90 nm). In this device structure, α-NPD (4,4'-bis-[N-(1-naphthyl)-N-phenylamino]-1,1'-biphenyl) and TPBi (1,3,5-tris(N-phenylbenzimidazol-2-yl)benzene) were served as an hole-transporting layer and electon-transporting layer and electron-injection layer, respectively. Additionally, thin layers of mCP (1,3-bis(9-carbazolyl)benzene) and DPEPO were inserted as an exciton blocking layers. The 2PXZ-OXD-based device showed green emission, while the 2PXZ-TAZ-based one exhibited blue emission (Figure 5-8a), reflecting the PL spectra of their doped films. The peak positions of the EL spectra of the 2PXZ-OXD-based device was observed at 508 nm. The 2PXZ-TAZ-based device displayed blue EL emission peak at 456 nm. The respective Commission Internationale de l'Éclairage (CIE) color coordinates of the 2PXZ-OXD and 2PXZ-TAZ-based devices were (0.25, 0.45) and (0.16, 0.15) at 10 mA cm^{-2}, respectively. Figure 5-8b and 5-8c depict the current density–voltage–luminance (*J–V–L*) and η_{ext} vs. *J* characteristics of the 2PXZ-OXD- and 2PXZ-TAZ-based OLEDs. The OLED containing 2PXZ-OXD as a green emitter showed a high maximum η_{ext} of 14.9%.

The theoretical maximum η_{ext} for this device was calculated using the equation:

$$\eta_{ext} = \left[0.25\Phi_{PF} + \{0.75 + 0.25(1 - \Phi_{PF})\} \frac{\Phi_{DF}}{1 - \Phi_{PF}} \right] \gamma \eta_{out} \tag{5-1}$$

where γ is the charge recombination factor and η_{out} is the light out-coupling efficiency, respectively.[23] Assuming that $\eta_{out} = 0.27$, η_{ext} is estimated to be 14.9%, which is consistent with the maximum η_{ext} obtained experimentally (Table 5-4). Here we define prompt and delayed components of η_{ext} as

$$\eta_{PF} = 0.25\Phi_{PF}\gamma\eta_{out} \tag{5-2}$$

$$\eta_{DF} = \{0.75 + 0.25(1 - \Phi_{PF})\} \frac{\Phi_{DF}}{1 - \Phi_{PF}} \gamma\eta_{out} \tag{5-3}$$

respectively. η_{PF} corresponds to the η_{ext} when an emitter is a conventional fluorescent molecule ($\Phi_{DF} = 0\%$ in Eq. (1)); that is, the molecule only emits fluorescence without a delayed component. For the 2PXZ-OXD-based device, $\eta_{PF} = 5.2\%$ and $\eta_{DF} = 9.7\%$ ($\eta_{out} = 0.27$). The contribution from TADF to the overall η_{ext} is almost twice that from the prompt component, showing that highly efficient $T_1 \rightarrow S_1$ up conversion is responsible for the high η_{ext} of this device.
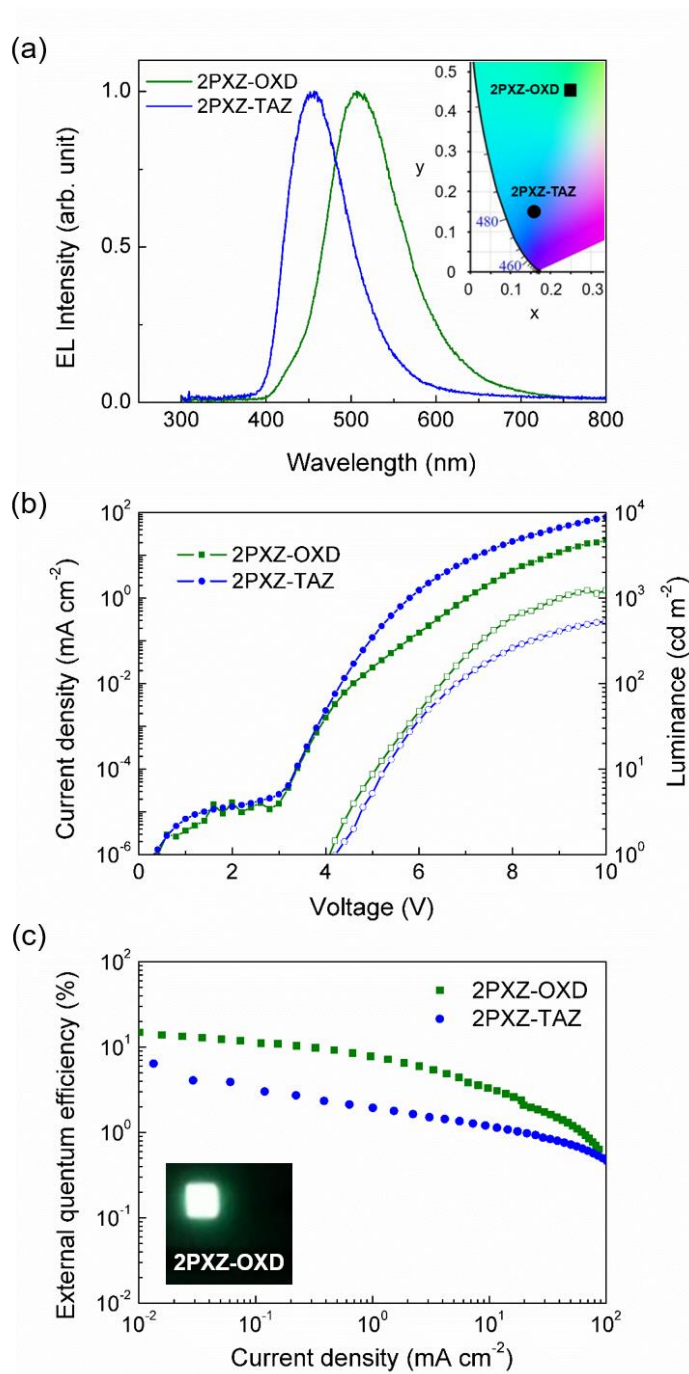
Figure 5-8. (a) EL spectra measured at 100 mA cm^{-2} (inset: EL color coordinates on the CIE 1931 chromaticity diagram), (b) current density–voltage–luminance (*J–V–L*) characteristics and (c) external EL quantum efficiency (η_{ext}) versus current density plots for the TADF-OLEDs (inset: photographs displaying EL emissions).

In the case of a 2PXZ-TAZ-based device, because Φ_{PF} is small, η_{ext} is low compared with that for the 2PXZ-OXD-based device. However, it is larger than the theoretical maximum η_{ext} for conventional fluorescent devices (5%). This is because efficient $T_1 \rightarrow S_1$ up conversion occurs in 2PXZ-TAZ. Assuming that $\eta_{out} = 0.15$, the calculated η_{ext} is in good agreement with the experimental result (6.4%). The theoretically estimated delayed component $\eta_{DF} = 5.8\%$ is approximately seven times that of the prompt component $\eta_{PF} = 0.8\%$. Thus, TADF makes a large contribution to η_{ext} for the 2PXZ-TAZ-based device.

Table 5-4. PL properties of TADF emitters and device performances of TADF OLEDs

Compound	τ_{PF} (ns)	τ_{DF} (ms)	Φ_{PL} (%)	Φ_{PF} (%)	Φ_{DF} (%)	η_{out}	η_p (%)	η_d (%)	η_{ext} (%) Calc.	η_{ext} (%) Exp.
2PXZ-OXD	11.23	0.52	87±3	76.6	10.4	0.27	5.2	9.7	14.9	14.9
2PXZ-TAZ	23.20	2.09	52±3	31.8	20.2	0.15	0.8	5.8	6.4	6.4

Subscripts PF and DF denote prompt and delayed components, respectively. τ, Φ, and η are the PL lifetime, PL quantum efficiency and theoretical maximum EL quantum efficiency, respectively. η_{out} was set as 0.27 and 0.15 for 2PXZ-OXD and 2PXZ-TAZ, respectively.

5. 5 Conclusion

Highly efficient TADF materials with D–A–D-type structures were developed. The D–A–D-type compounds show more efficient TADF and higher η_{ext} in toluene solution than D–A-type compounds. D–A–D-type molecule 2PXZ-OXD displayed an extremely high Φ_{PL} of 87% when doped into the host DPEPO. The η_{ext} of an OLED using 2PXZ-OXD as a green emitter reached 14.9%, which surpasses those obtained with conventional fluorescent emitters.

5. 6 Experimental Section

5. 6. 1 Materials and Synthesis

Commercially available reagents and solvents were used without further purification unless otherwise noted. All of the reactions were performed under a nitrogen atmosphere in dry solvents using standard Schlenk techniques. NMR spectra were recorded on an Avance III 400 spectrometer (Bruker). Chemical shifts of ^{1}H and signals were determined relative to the signals of tetramethylsilane ($\delta = 0.00$), CDCl$_3$ ($\delta = 77.0$) as internal standards. Matrix-assisted laser desorption ionization time-of-flight (MALDI-TOF) mass spectra were collected on an Autoflex III spectrometer (Bruker Daltonics) using dithranol as a matrix. Elemental analysis was carried out with a MT-5 CHN Corder (Yanaco).
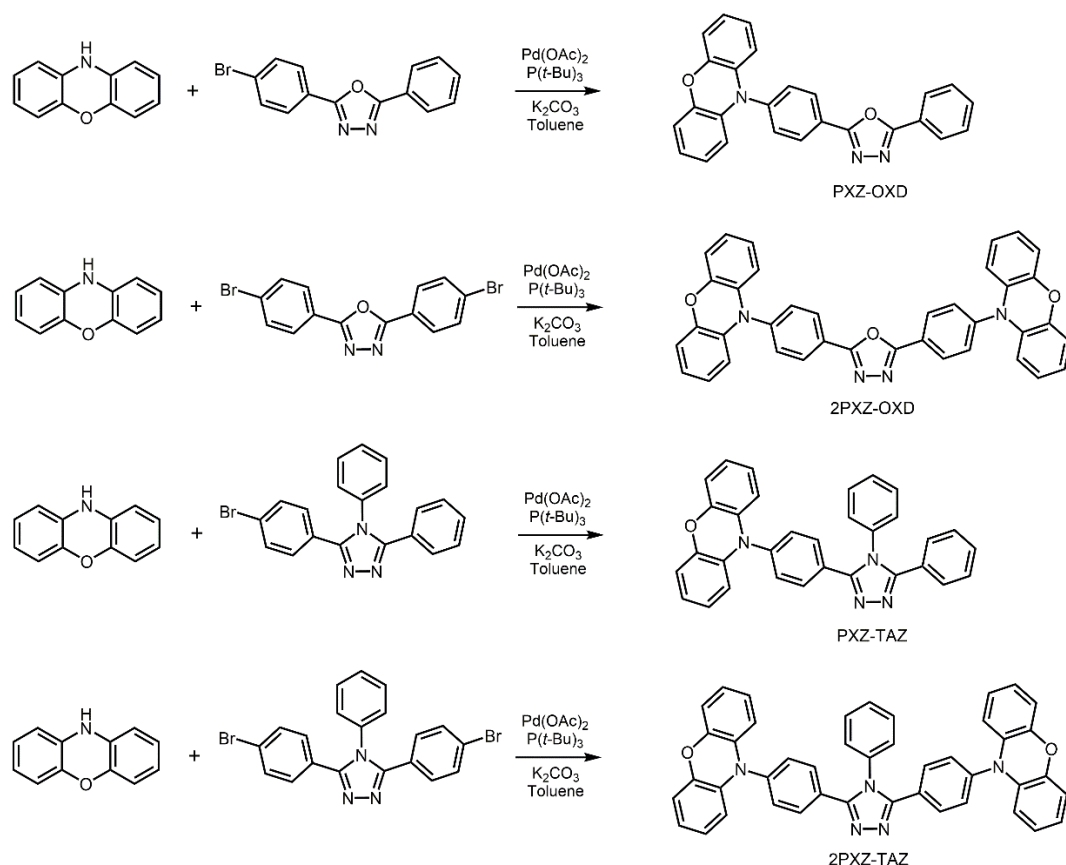
Scheme 5-1. Synthesis routes for PXZ-OXD, 2PXZ-OXD, PXZ-TAZ, and 2PXZ-OXD.

Synthesis of PXZ-OXD: To a solution of 2-(4-bromophenyl)-5-phenyl-1,3,4-oxadiazole (1.20 g, 3.98 mmol, synthesized by a reported method[24]), phenoxazine (802 mg, 4.38 mmol) and potassium carbonate (1.81 g, 13.1 mmol) in toluene (30 mL) was added, with stirring, a solution of palladium(II) acetate (29.2 mg, 0.13 mmol) and tri-*tert*-butylphosphine (97.1 mg, 0.48 mmol) in toluene (30 mL). The mixture was stirred and heated under reflux for one day. The cooled mixture was partitioned between chloroform and water. The organic layer was separated, and the aqueous layer was extracted with chloroform. The combined organic layers were washed with brine, dried over MgSO$_4$, and concentrated *in vacuo*. Purification of the residue by column chromatography (eluent: toluene/ethyl acetate = 10:1) afforded 1.52 g of PXZ-OXD. The yield was over 94%. The compound was further purified by sublimation under reduced pressure for OLED fabrication. ^{1}H NMR (CDCl$_3$, 400 MHz) δ = 5.98 (d, 2H), 6.64 (t, 2H), 6.69 (t, 2H), 6.72 (d, 2H), 7.55 (m, 5H), 8.17 (d, 2H), 8.38 (d, 2H); ^{13}C NMR (CDCl$_3$, 100MHz) δ = 113.3, 115.7, 121.9, 123.3, 127.0, 129.2, 129.7, 131.8, 131.9, 133.7, 142.4, 144.0. MS (MALDI-TOF): *m/z* [*M*+H]$^+$ calcd 403; found, 403. Anal. Calcd (%) for C$_{54}$H$_{36}$N$_8$: C, 77.41; H, 4.25; N, 10.42; found: C, 77.58; H, 4.18; N, 10.42.

Synthesis of 2PXZ-OXD: To a solution of 2,5-bis(4-bromophenyl)-1,3,4-oxadiazole (630.8 mg, 1.66 mmol, synthesized by a reported method[25]), phenoxazine (668.7 mg, 3.65 mmol) and potassium carbonate (1.52 g, 11.0 mmol) in toluene (25 mL) was added, with stirring, a solution of palladium(II) acetate (25.0 mg, 0.11 mmol) and tri-*tert*-butylphosphine (81.0 mg, 0.40 mmol) in toluene (25 mL). The mixture was stirred and heated under reflux for one day. The cooled mixture was partitioned between chloroform and water. The organic layer was separated, and the aqueous layer was extracted with chloroform. The combined organic layers were washed with brine, dried over $MgSO_4$, and concentrated *in vacuo*. Purification of the residue by column chromatography (eluent: chloroform) afforded 965.2 mg of 2PXZ-OXD. The yield was over 99%. The compound was further purified by sublimation under reduced pressure for OLED fabrication. ^{1}H NMR ($CDCl_3$, 400 MHz) δ = 5.99 (d, 4H), 6.61 (t, 4H), 6.68 (m, 8H), 7.57 (d, 4H), 8.39 (d, 4H); ^{13}C NMR ($CDCl_3$, 100MHz) δ = 113.3, 115.8, 121.9, 123.3, 129.7, 131.9, 133.7, 142.6, 144.0, 164.2. MS (MALDI-TOF): m/z [M+H]$^+$ calcd 584; found, 584. Anal. Calcd (%) for $C_{54}H_{36}N_8$: C, 78.07; H, 4.14; N, 9.58; found: C, 78.02; H, 4.06; N, 9.56.

Synthesis of PXZ-TAZ: To a solution of 3-(4-bromophenyl)-4,5-diphenyl-1,2,4-triazole (1.00 g, 2.66 mmol, synthesized by a reported method[26]), phenoxazine (537 mg, 2.93 mmol) and potassium carbonate (1.21 g, 8.79 mmol) in toluene (20 mL) was added, with stirring, a solution of palladium(II) acetate (20.2 mg, 0.09 mmol) and tri-*tert*-butylphosphine (64.7 mg, 0.32 mmol) in toluene (20 mL). The mixture was stirred and heated under reflux for one day. The cooled mixture was partitioned between chloroform and water. The organic layer was separated, and the aqueous layer was extracted with chloroform. The combined organic layers were washed with brine, dried over $MgSO_4$, and concentrated *in vacuo*. Purification of the residue by column chromatography (eluent: toluene/ethyl acetate = 1:1) afforded 1.01 g of PXZ-TAZ. The yield was over 79%. The compound was further purified by sublimation under reduced pressure for OLED fabrication. ^{1}H NMR (DMSO, 400 MHz) δ = 5.79 (d, 2H), 6.67 (t, 2H), 6.70 (t, 2H), 6.74 (d, 2H), 7.39 (d, 2H), 7.41 (m, 6H), 7.46 (d, 2H), 7.52 (d, 2H), 7.67 (d, 2H); ^{13}C NMR ($CDCl_3$, 100MHz) δ = 113.2, 115.6, 121.6, 123.2, 126.7, 127.8, 128.5, 128.8, 129.8, 130.2, 131.0, 131.3, 133.9, 134.6, 140.4, 143.9. MS (MALDI-TOF): m/z [M+H]$^+$ calcd 478; found, 478. Anal. Calcd (%) for $C_{54}H_{36}N_8$: C, 80.32; H, 4.63; N, 11.71; found: C, 81.21; H, 4.58; N, 11.70.

Synthesis of 2PXZ-TAZ: To a solution of 3,5-bis(4-bromophenyl)-4-phenyl-4H-1,2,4-triazole (1.50 g, 3.30 mmol, synthesized by a reported method[24]), phenoxazine (1.33 g, 7.26 mmol) and potassium carbonate (3.01 g, 21.8 mmol) in toluene (40 mL) was added, with stirring, a solution of palladium(II) acetate (49.4 mg, 0.22 mmol) and tri-*tert*-butylphosphine (161.9 mg, 0.80 mmol) in toluene (40 mL). The mixture was stirred and heated under reflux for one day. The cooled mixture was partitioned between chloroform and water. The organic layer was separated, and the aqueous layer was extracted with chloroform. The combined organic layers were washed with brine, dried over $MgSO_4$, and concentrated *in vacuo*. Purification of the residue by column chromatography (eluent: chloroform/hexane=1:4) afforded 1.52 g of 2PXZ-TAZ. The yield was over 70%. The compound was further purified by sublimation under reduced pressure for OLED fabrication. ^{1}H NMR ($CDCl_3$, 400 MHz) $\delta = 5.88$ (d, 4H), 6.57 (t, 4H), 6.64 (m, 8H), 7.30 (m, 6H), 7.55 (m, 3H), 7.68 (d, 4H); ^{13}C NMR ($CDCl_3$, 100MHz) $\delta = 113.2$, 115.6, 121.7, 123.2, 126.9, 127.8, 130.4, 131.1, 131.2, 133.8, 135.1, 140.5, 143.9, 154.3. MS (MALDI-TOF): *m*/*z* [*M*+H]$^+$ calcd 659; found, 659. Anal. Calcd (%) for $C_{54}H_{36}N_8$: C, 80.10; H, 4.43; N, 10.62; found: C, 80.11; H, 4.37; N, 10.61.

5. 6. 2 Quantum Chemical Calculations

All quantum chemical calculations were performed using the Gaussian 09 program package. S_0 geometries were optimized at the CAM-B3LYP/cc-pVDZ level of theory. S_1 and NTOs were calculated with a time-dependent density functional theory (TD-DFT) method using the optimized S_0 geometries (denoted as TD-CAM-B3LYP/cc-pVDZ//CAM-B3LYP/cc-pVDZ). Solvent effects were taken into account within the polarizable continuum model.

5. 6. 3 Photophysical Measurements

UV–vis absorption and PL spectra were measured with a UV-2550 spectrometer (Shimadzu) and a Fluoromax-4 spectrophotometer (Horiba Scientific), respectively, using spectral grade solvents. The PL quantum efficiencies were measured using an integration sphere system C9920-02 coupled with a PMA-11 photonic multichannel analyser (Hamamatsu Photonics) by photoexcitation (PXZ-OXD = 390 nm, 2PXZ-OXD = 400 nm, PXZ-TAZ = 370 nm , and 2PXZ-TAZ = 380 nm). The temperature dependence of transient PL decays was measured using a C4334 Streak camera (Hamamatsu Photonics) with a N_2 gas laser ($\lambda = 337$ nm, pulse width = 500 ps and repetition rate = 20 Hz) under vacuum ($<4 \times 10^{-1}$ Pa). Room-temperature transient

PL decay measurements were carried out using a C11367 Quantaurus-tau fluorescence lifetime spectrometer (Hamamatsu Photonics).

5. 6. 4 OLED Fabrication and Characterization

ITO-coated glass substrates were cleaned with detergent, deionized water, acetone, and isopropanol. The substrates were then subjected to UV–ozone treatment for 15 min before they were loaded into a vacuum evaporation system. The organic layers were thermally evaporated on the substrates under vacuum ($<3 \times 10^{-4}$ Pa) at an evaporation rate of <0.3 nm s^{-1}. LiF and Al layers were then deposited through a shadow mask. The layer thickness and the deposition rate were monitored *in situ* during deposition by an oscillating quartz thickness monitor. The current density–voltage–luminance characteristics of the devices were measured using a source meter (Keithley 2400, Keithley Instruments Inc.) and an absolute external quantum efficiency measurement system (C9920-12, Hamamatsu Photonics). The OLEDs were mounted to the entrance port of the measurement system's integrating sphere to collect the photons emitted from the front face of the devices. EL spectra were collected by an optical fiber connected to a spectrometer (PMA-12, Hamamatsu Photonics).

References

[1]   H. Tanaka, K. Shizu, H. Miyazaki and C. Adachi, *Chem. Commun.* **2012**, *48*, 11392.

[2]   Y. Hamada, C. Adachi, T. Tsutsui and S. Saito, *J. J. Appl. Phys.* **1992**, *31*, 1812.

[3]   N. Tamoto, C. Adachi and K. Nagai, *Chem. Mater.* **1997**, *9*, 1077.

[4]   Y. Zhu, A. P. Kulkarni and S. A. Jenekhe, *Chem. Mater.* **2005**, *17*, 5225.

[5]   C. Adachi, T. Tsutsui and S. Saito, *Appl. Phys. Lett.* **1989**, *55*, 1489.

[6]   J. Kido, C. Ohtaki, K. Hongawa, K. Okuyama and K. Nagai, *J. J. Appl. Phys.* **1993**, *32*, L917.

[7]   A. P. Kulkarni, C. J. Tonzola, A. Babel and S. A. Jenekhe, *Chem. Mater.* **2004**, *16*, 4556.

[8]   C. Adachi, M. A. Baldo, S. R. Forrest and M. E. Thompson, *Appl. Phys. Lett.* **2000**, *77*, 904.

[9]   Y. Tao, Q. Wang, L. Ao, C. Zhong, C. Yang, J. Qin and D. Ma, *J. Phys. Chem. C* **2009**, *114*, 601.

[10]   Y. Park, B. Kim, C. Lee, A. Hyun, S. Jang, J.-H. Lee, Y.-S. Gal, T. H. Kim, K.-S. Kim and J. Park, *J. Phys. Chem. C* **2011**, *115*, 4843.

[11]   K. M. Karlsson, X. Jiang, S. K. Eriksson, E. Gabrielsson, H. Rensmo, A. Hagfeldt and L. Sun, *Chem. Eur. J.* **2011**, *17*, 6415.

[12]   D. Basting, D. Ouw and F. P. Schäfer, *Opt. Commun.* **1976**, *18*, 260.

[13]   P. Greenspan, E. P. Mayer and S. D. Fowler, *J. Cell Biol.* **1985**, *100*, 965.

[14]   P. Greenspan and S. D. Fowler, *J. Lipid Res.* **1985**, *26*, 781.

[15]   R. Bauernschmitt and R. Ahlrichs, *Chem. Phys. Lett.* **1996**, *256*, 454.

[16]   M. E. Casida, C. Jamorski, K. C. Casida and D. R. Salahub, *J. Chem. Phys.* **1998**, *108*, 4439.

[17]   T. Yanai, D. P. Tew and N. C. Handy, *Chem. Phys. Lett.* **2004**, *393*, 51.

[18]   J. T. H. Dunning, *J. Chem. Phys.* **1989**, *90*, 1007.

[19]   R. Improta, V. Barone, G. Scalmani and M. J. Frisch, *J. Chem. Phys.* **2006**, *125*, 054103.

[20]   R. Improta, G. Scalmani, M. J. Frisch and V. Barone, *J. Chem. Phys.* **2007**, *127*, 074504.

[21]   J. Tomasi, B. Mennucci and R. Cammi, *Chem. Rev.* **2005**, *105*, 2999.

[22]   H. Xu, L.-H. Wang, X.-H. Zhu, K. Yin, G.-Y. Zhong, X.-Y. Hou and W. Huang, *J. Phys. Chem. B* **2006**, *110*, 3023.

[23]   A. Endo, K. Sato, K. Yoshimura, T. Kai, A. Kawada, H. Miyazaki and C. Adachi, *Appl. Phys. Lett.* **2011**, *98*, 083302.

[24]   W. Kwon, B. Ahn, D. M. Kim, Y.-G. Ko, S. G. Hahm, Y. Kim, H. Kim, and M. Ree, *J. Phys. Chem. C* **2011**, *115*, 19355.

[25]   X. J. Feng, P. L. Wu, K. F. Li, M. S. Wong, and K. W. Cheah, *Chem. Eur. J* **2011**, *17*, 2518.

[26]   S. Kwon, K.-R. Wee, A.-L. Kim, and S. O. Kang, *J. Phys. Chem. Lett.* **2010**, *1*, 295.

Chapter 6

Phenazine-Based Thermally Activated Delayed Fluorescence Materials for Emission Color Tuning in Organic Light-Emitting Diodes
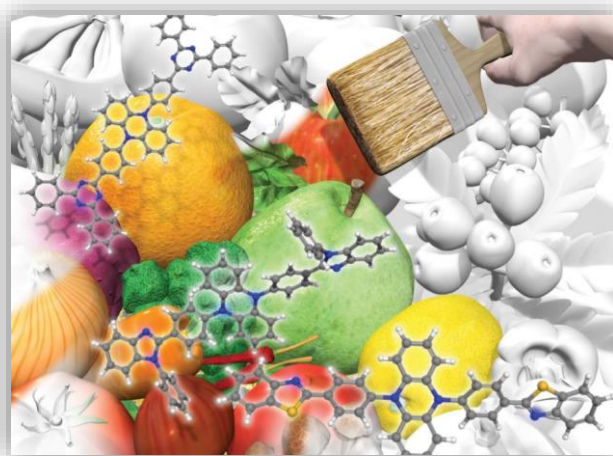
6. 1 Introduction

Photophysical properties of TADF compounds depend on an energy difference (ΔE_{ST}) between the lowest excited singlet (S_1) and triplet (T_1) states. For TADF compounds, ΔE_{ST} is related to the degree of spatial overlap between the highest occupied molecular orbital (HOMO) and lowest unoccupied molecular orbital (LUMO). Thus, by spatially separating HOMO and LUMO, ΔE_{ST} can be decreased. TADF compounds with well separated HOMO and LUMO, for example, PIC-TRZ-2,[1] PXZ-TRZ,[2] *bis*-PXZ-TRZ, and *tri*-PXZ-TRZ,[3] have ΔE_{ST} values of nearly 0 eV.

By modulating ΔE_{ST}, the delayed fluorescence lifetime (τ_{DF}) of TADF compounds can be controlled. When ΔE_{ST} is small, the reverse intersystem crossing (RISC) in a TADF compound is expected to be fast, leading to short triplet exciton lifetime (τ_T). When τ_T is short, exciton annihilation processes such as triplet-triplet (T–T) and singlet-triplet (S–T) annihilations are expected to be suppressed. Conversely, when ΔE_{ST} is large, these exciton annihilations have time to actively occur because of the long τ_T, resulting in a large roll-off of external electroluminescence (EL) quantum efficiencies (η_{ext}).[4] For phosphorescent OLEDs, it is well known that T–T annihilation is a major factor of their roll-off behavior.[5] By using a TADF compound with a small ΔE_{ST} as an emitter, highly efficient OLEDs with small roll-off can be developed. In fact, OLEDs containing PXZ-TRZ, bis-PXZ-TRZ, or tri-PXZ-TRZ as an emitter exhibit small roll-off, indicating a close relationship between ΔE_{ST} and efficiency roll-off.[2,3]

In this chapter, novel TADF materials by combining a dihydrophenazine donor with various electron acceptor moieties have been developed. Dihydrophenazine has two NH groups and one or two electron acceptors can be introduced into it, so donor (D)–acceptor (A)-type and A–D–A-type structures are possible. In a previous study (chapter 5), the author reported that TADF compounds with D–A–D-type structure showed higher photoluminescence (PL) quantum efficiency (Φ_{PL}) than those with just D–A,[6] indicating that an A–D–A type structure is a promising candidate for TADF emitters. In this work, emitters with A–D–A-type structure rather than D–A have been prepared. By using dihydrophenazine as an electron donor, TADF compounds exhibited various photophysical properties such as emission colors (green to orange), ΔE_{ST} (~0 to 0.19 eV) and τ_{DF} (0.14 to 53 μs) by changing the acceptor moieties.

6. 2 Molecular Design and Quantum Chemical Calculations

Benzimidazole, benzonitrile, benzothiazole, and triazine are well-known electron-accepting units. Benzimidazole is one of the most widely used acceptors in OLEDs because of its good electron-accepting ability.[7] For example, 1,3,5-tris(*N*-phenylbenzimidazole-2-yl)benzene (TPBi) containing three benzimidazole moieties has been used as an effective electron-transporting and host material in OLEDs.[7a] Compounds containing benzonitrile acceptor groups can form twisted intramolecular charge transfer (TICT) excited states. Derivatives of 4-dimethylaminobenzonitrile exhibit unique photophysical properties such as dual fluorescence, and have attracted a great deal of interest in photochemistry.[8] Benzothiazole also has a good electron-accepting ability and has been used to develop EL and electron-transporting materials.[9] Green fluorescent compounds containing benzothiazole and coumarin moieties have been used as EL materials for OLEDs.[9a,9b] Triazine-based compounds have been used as electron-transporting materials[10] and electron transport-type host materials[11] because of their good electron-accepting ability. Various triazine-based TADF compounds have been developed as an effective electron acceptor in TADF compounds.[1–3,12,13]

In this study, a new series of A–D–A molecules consisting of 1,2-diphenylbenzimidazole (BI), benzonitrile (BN), 2-phenylbenzothiazole (BTZ) or 2,4,6-triphenyl-1,3,5-triazine (TRZ) as an acceptor and 5,10-dihydrophenazine (DHPZ) as a donor was designed (Figure 6-1).
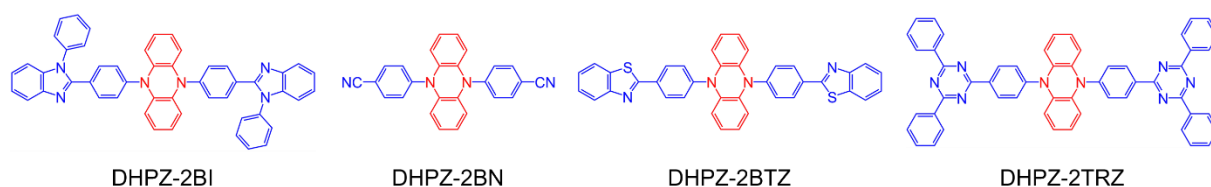
Figure 6-1. Chemical structures for DHPZ-2BI, DHPZ-2BN, DHPZ-2BTZ, and DHPZ-2TRZ.

To explain the reason why S$_1$ of DHPZ-2BI, DHPZ-2BN, DHPZ-2BTZ, and DHPZ-2TRZ has charge transfer (CT) character, Quantum chemical calculations were performed. Figure 6-2 shows the highest occupied and lowest unoccupied natural transition orbitals[14] (NTOs) for S$_1$ state of the compounds. By taking solvent effects into account within the polarizable continuum model,[15] this method reasonably reproduces absorption and emission wavelengths of the compounds in toluene solution (Table 6-1). The highest occupied NTOs are largely localized on the dihydrophenazine moieties, while the lowest unoccupied NTOs are localized on the acceptor moieties, resulting in good spatial separation of the two NTOs. This separation

results from the strong electron-donating and -accepting abilities of the donor and acceptor moieties, respectively. In addition, large twist angles of nearly 90° between the units also induce the separation of the NTOs. Because the HOMO–LUMO transition dominates ground (S_0) state–S_1 excitation for these compounds, the distribution patterns of the highest occupied and lowest unoccupied NTOs reflect those of the HOMO and LUMO, respectively. The theoretical calculations suggest that in S_0–S_1 excitation, an electron transfers from donor to acceptor moieties. The S_1 states thus have CT characteristics.

Highest occupied NTO   Lowest unoccupied NTO
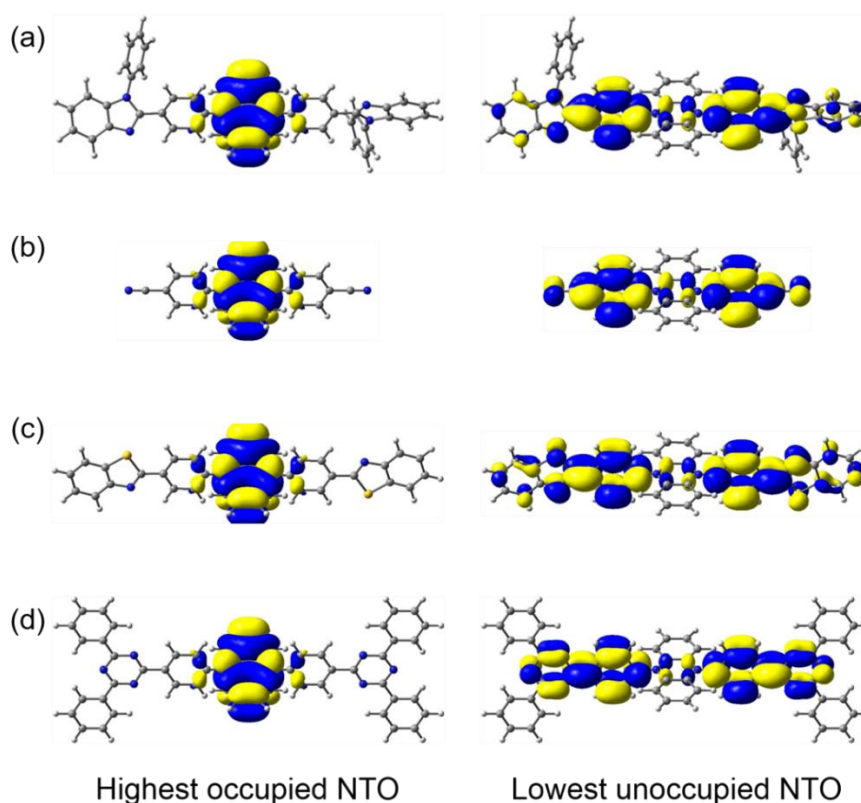
Figure 6-2. Highest occupied and lowest unoccupied natural transition orbitals for S_1 of (a) DHPZ-2BI, (b) DHPZ-2BN, (c) DHPZ-2BTZ, and (d) DHPZ-2TRZ calculated at the TD-CAM-B3LYP/cc-pVDZ//CAM-B3LYP/cc-pVDZ level of theory.

Table 6-1. Calculated and experimental absorption and emission wavelengths for DHPZ-2BI, DHPZ-2BN, DHPZ-2BTZ, and DHPZ-2TRZ

Compound	λ_{abs} (nm)		λ_{em} (nm)	
	Calc.	Exp.	Calc.	Exp.
DHPZ-2BI	421	428	566	550
DHPZ-2BN	473	420	562	545
DHPZ-2BTZ	495	450	609	605
DHPZ-2TRZ	513	479	627	648

Absorption (λ_{abs}) and emission wavelengths (λ_{em}) were computed using time-dependent density functional theory (TD-DFT) at the CAM-B3LYP/cc-pVDZ level of theory. Solvent effects were taken into account by means of the polarizable continuum model.

6. 3 Photophysical and TADF Properties

The photophysical properties of DHPZ-2BI, DHPZ-2BN, DHPZ-2BTZ, and DHPZ-2TRZ in toluene solution suggest that they exhibit TADF. Figure 6-3 shows PL spectra for the four compounds in toluene solution measured at room temperature. DHPZ-2BI and DHPZ-2BN showed green emission, while DHPZ-2BTZ and DHPZ-2TRZ exhibited yellow and orange emission, respectively. The broad emission bands originate from the CT character of S1 of the four compounds, as discussed below. It was previously reported that PXZ-TRZ containing a phenoxazine donor and triazine acceptor shows green emission.[2] Comparing DHPZ-2TRZ with PXZ-TRZ suggests that replacing the phenoxazine moiety in a TADF compound with dihydrophenazine causes upward shift of HOMO level and red shift of emission color. Interestingly, in addition to the CT emission peak at 650 nm, DHPZ-2TRZ shows a weak emission peak at around 450 nm. Such dual emission has been observed for molecules with excited states of TICT characteristics.[8] This additional peak was assigned to a locally excited (LE) state of the dihydrophenazine moiety, because dihydrophenazine derivatives show emission peaks at 430–460 nm.[16] For the compounds other than DHPZ-2TRZ, since the intensity of the emission from the CT excited state is strong compared with that from the LE state, the emission peak at around 450 nm does not clearly appear in the PL spectra. The low Φ_{PL} of DHPZ-2TRZ can be explained by the energy-gap law, which states that non-radiative decay rate increases with decreasing the energy difference between the S_1 and S_0 states.
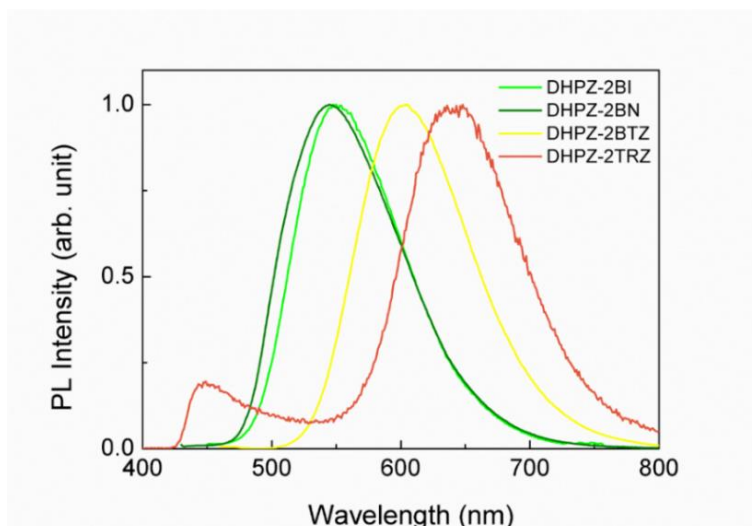

Figure 6-3. PL spectra recorded for DHPZ-2BI, DHPZ-2BN, DHPZ-2BTZ, and DHPZ-2TRZ in toluene solution.

DHPZ-2BI, DHPZ-2BN, and DHPZ-2BTZ were confirmed to emit delayed fluorescence in toluene solution after excluding oxygen (which quenches triplet states) by bubbling nitrogen through the solution for 10 min. For the above three compounds, after deoxygenation, delayed components with long lifetimes were observed in their time-resolved PL decays. Although a delayed component for DHPZ-2TRZ was not observed clearly in toluene solution, as stated below, DHPZ-2TRZ was confirmed to emit TADF in a solid-state host matrix. Prompt fluorescence lifetime (τ_{PF}), τ_{DF}, and Φ_{PL} for the compounds in toluene solution are listed in Table 6-2. Φ_{PL} were higher in the absence of oxygen than in air, suggesting that in air, triplet states were quenched by oxygen, and RISC from triplet to singlet states was suppressed. Of the four compounds, DHPZ-2BI showed the highest Φ_{PL} of 24.1%.

Table 6-2. PL properties of DHPZ-2BI, DHPZ-2BN, DHPZ-2BTZ, and DHPZ-2TRZ in toluene solution

Compound	In air			After nitrogen bubbling		
	Φ_{PL} (%)	τ_{PF} (ns)	τ_{DF} (μs)	Φ_{PL} (%)	τ_{PF} (ns)	τ_{DF} (μs)
DHPZ-2BI	5.7	4.96	n.d.	24.1	6.75	5.71
DHPZ-2BN	3.3	5.02	n.d.	8.4	6.28	1.88
DHPZ-2BTZ	4.7	4.18	n.d.	9.7	6.85	0.24
DHPZ-2TRZ	0.7	1.01	n.d.	2.2	1.08	n.d.

τ_{PF} and τ_{DF} are lifetimes of prompt and delayed components, respectively. The delayed components were not observed in air.

The difference in the emission wavelengths of our compounds originates from the variation of their LUMO energy levels. Figure 6-4 shows the energy levels of the HOMO and LUMO of neat films of DHPZ-2BI, DHPZ-2BN, DHPZ-2BTZ, and DHPZ-2TRZ fabricated by vacuum deposition. The HOMO energy levels are almost the same, while the LUMO energy levels vary depending on the acceptor moieties. The HOMO energy levels do not depend on the acceptor moieties, suggesting that the HOMOs originate predominantly from the dihydrophenazine moiety. The LUMO energy level of the DHPZ-2BN neat film was lower than that expected from its emission spectrum in toluene solution. In toluene solution, because DHPZ-2BN and DHPZ-2BI exhibit similar emission wavelengths, their neat films are expected to have comparable LUMO energy levels. However, the LUMO energy level of the neat DHPZ-2BN film is 0.17 eV lower than that of the neat DHPZ-2BI film. This indicates that interaction between the LUMOs of neighboring molecules is stronger for DHPZ-2BN than for DHPZ-2BI in their neat films.
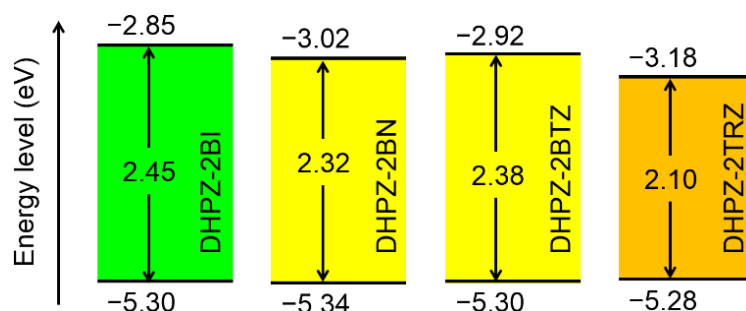
Figure 6-4. Experimental HOMO and LUMO energy levels of neat DHPZ-2BI, DHPZ-2BN, DHPZ-2BTZ, and DHPZ-2TRZ films.

To investigate the PL characteristics of DHPZ-2BI, DHPZ-2BN, DHPZ-2BTZ, and DHPZ-2TRZ in a host layer, 6 wt% DHPZ-2BI-, DHPZ-2BN-, DHPZ-2BTZ-, and DHPZ-2TRZ-doped 9,9′-biphenyl-3,3′-diyl-bis-9*H*-carbazole (*m*-CBP) films were prepared by vacuum codeposition. Figure 6-5 shows PL spectra of the doped films measured at 300 K. The DHPZ-2BI- and DHPZ-2BN-doped films showed green emission with peak maxima at 537 nm (2.31 eV) and 541 nm (2.29 eV), respectively, while the DHPZ-2BTZ- and DHPZ-2TRZ-doped films showed yellow and orange emissions with peak maxima at 577 nm (2.15 eV) and 598 nm (2.07 eV), respectively. Because the T_1 energy level of m-CBP is 2.84 eV, T_1 and S_1 excitons of the TADF compounds are well confined in the *m*-CBP layers.[17]
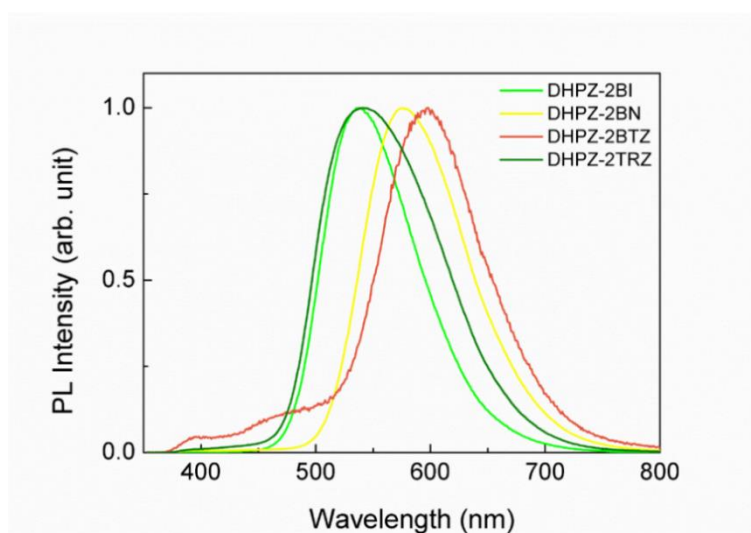

Figure 6-5. PL spectra of DHPZ-2BI, DHPZ-2CN, DHPZ-2BTZ, and DHPZ-2TRZ in 6 wt%-emitter:*m*-CBP doped thin films.

Transient PL decays of the 6 wt% emitter:*m*-CBP doped films show that DHPZ-2BI, DHPZ-2BN, DHPZ-2BTZ, and DHPZ-2TRZ emit TADF in the doped films. The transient PL decays were measured using a streak camera. As shown in Figure 6-6, the transient PL decay curves

display a similar temperature dependence. The intense emission and long tail are attributed to prompt and delayed components, respectively. The intensity of the delayed component increases with temperature from 50 to 200 K, suggesting that the delayed component originates from TADF. In contrast, the intensity of the delayed component slightly decreases with increasing temperature over 200 K, suggesting that over 200 K, a slight increase of $T_1 \rightarrow S_0$ nonradiative decay becomes a competitive process for $T_1 \rightarrow S_1$ RISC. τ_{DF} of DHPZ-2BI, DHPZ-2BN, DHPZ-2BTZ, and DHPZ-2TRZ at 300 K were approximately 50 μs, 7 μs, 1 μs, and 0.1 μs, respectively. From the onsets of the fluorescence and phosphorescence (4K) spectra in the doped films, ΔE_{ST} values of DHPZ-2BI, DHPZ-2BN, and DHPZ-2BTZ were experimentally determined to be 0.19 eV, 0.10, eV and ~0 eV, respectively (Figure 6-7).
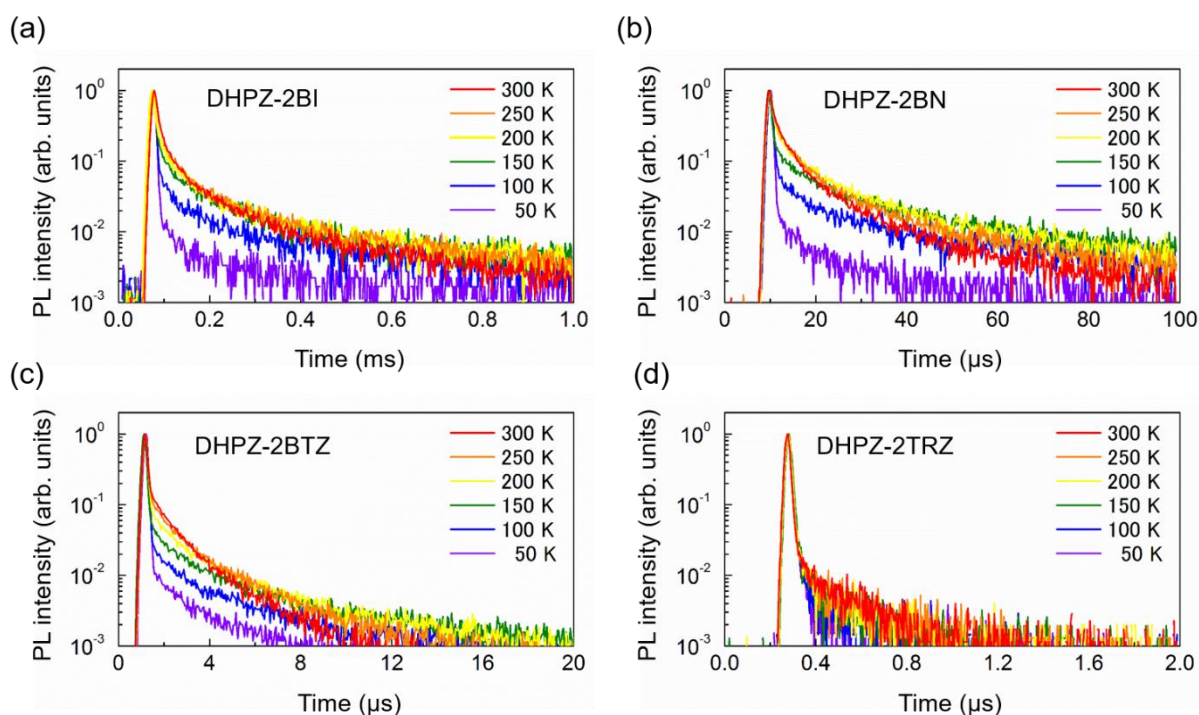
Figure 6-6. Temperature dependence of transient PL decay curves ranging from 50 to 300 K for (a) 6 wt%-DHPZ-2BI:*m*-CBP, (b) 6 wt%-DHPZ-2BN:*m*-CBP, (c) 6 wt%-DHPZ-2BTZ:*m*-CBP, and (d) 6 wt%-DHPZ-2TRZ:*m*-CBP doped films.

ΔE_{ST} decreases in the following order: DHPZ-2BI>DHPZ-2BN>DHPZ-2BTZ, which is consistent with the calculated results (Table 6-3). For DHPZ-2BTZ, ΔE_{ST} is nearly 0 eV. ΔE_{ST} value of DHPZ-2TRZ could not be determined because the phosphorescence spectrum of the 6 wt% DHPZ-2TRZ:*m*-CBP doped film was not clearly observed. τ_{DF} decreases with ΔE_{ST},

suggesting that small ΔE_{ST} leads to a higher rate of $T_1 \rightarrow S_1$ RISC and shorter τ_{DF}. In contrast, τ_{PF} is unrelated to ΔE_{ST}.
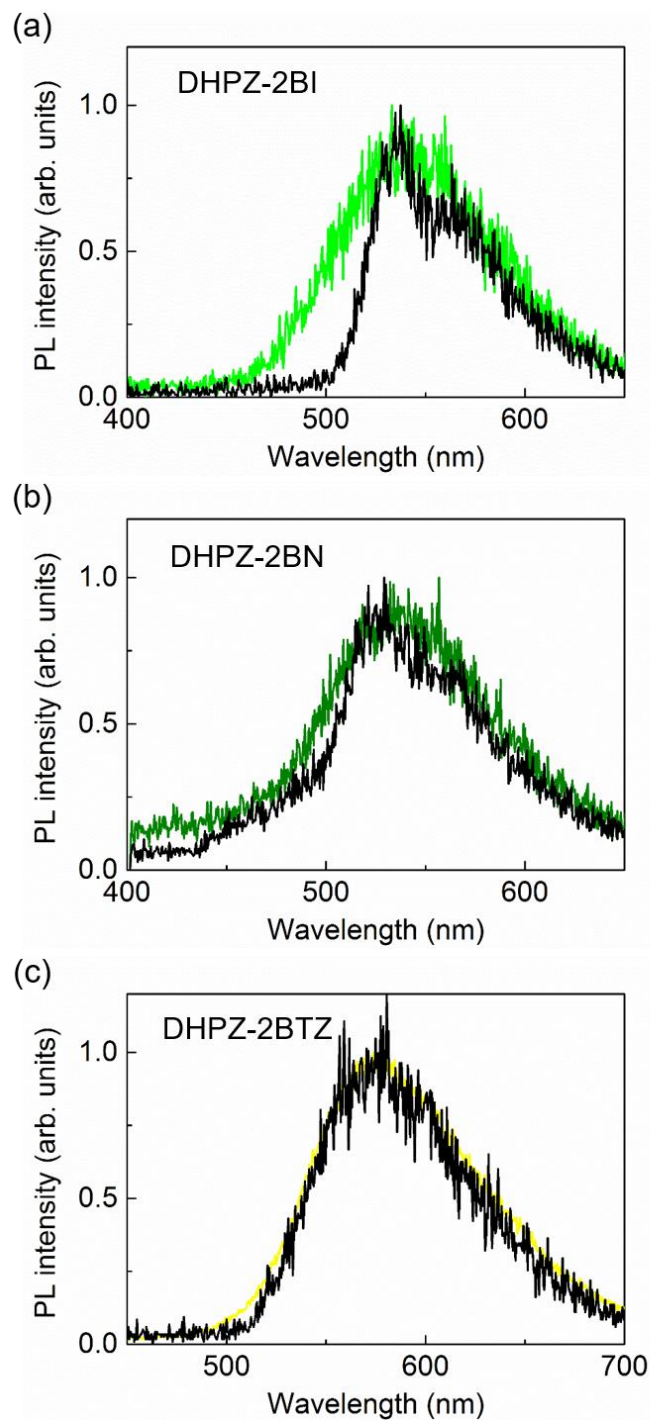
Figure 6-7. Fluorescence spectra (light-green, green, and yellow lines) and phosphorescence spectra at 4 K (black lines) for (a) 6 wt%-DHPZ-2BI:*m*-CBP, (b) 6 wt%-DHPZ-2BN:*m*-CBP, and (c) 6 wt%-DHPZ-2BTZ:*m*-CBP doped films.

DHPZ-2BI exhibited the highest Φ_{PL} of 67.6%, and contributions from the prompt fluorescence (Φ_{PF}) and delayed fluorescence (Φ_{DF}) to Φ_{PL} are almost equal ($\Phi_{PF} \approx \Phi_{DF}$) (Table 6-4). Φ_{DF} decreases with increasing emission wavelength (decreasing S_0–S_1 energy gap), suggesting that when the S_0–S_1 energy is small, $T_1 \rightarrow S_0$ nonradiative decay is fast, leading to poor RISC efficiency. For DHPZ-2TRZ, Φ_{DF} is quite low even though ΔE_{ST} is sufficiently small to allow RISC. In addition to the low Φ_{DF}, Φ_{PF} for DHPZ-2TRZ is much lower than those for the other compounds. These observations indicate that for orange to red TADF compounds, excessive separation of the spatial overlap between HOMO and LUMO suppresses $S_1 \rightarrow S_0$ radiative decay (decreasing Φ_{PF}), leading to low Φ_{PL}. Increasing the spatial overlap and promoting $S_1 \rightarrow S_0$ radiative decay is necessary to realize TADF compounds that exhibit high Φ_{PL} and orange to red emission.

Table 6-3. Calculated ΔE_{ST} values of DHPZ-2BI, DHPZ-2BN, DHPZ-2BTZ, and DHPZ-2TRZ

Compound	ΔE_{ST} (eV)
DHPZ-2BI	0.83
DHPZ-2BN	0.60
DHPZ-2BTZ	0.52
DHPZ-2TRZ	0.42

ΔE_{ST} calculated using the TD-CAM-B3LYP/cc-pVDZ//CAM-B3LYP/cc-pVDZ method.

Table 6-4. PL properties of TADF emitters and device performances of TADF OLEDs

Compound	ΔE_{ST} (eV)	τ_{PF} (ns)	τ_{DF} (μs)	Φ_{PL} (%)	Φ_{PF} (%)	Φ_{DF} (%)	η_{PF} (%)	η_{DF} (%)	η_{ext} (%) Calc.	η_{ext} (%) Exp.
DHPZ-2BI	0.19	4	50	67.6	34.0	33.6	1.86	10.20	11-17	12
DHPZ-2BN	0.10	7	7	35.2	16.8	18.4	0.99	4.98	5-8	6
DHPZ-2BTZ	~0	12	1	33.0	20.6	12.4	1.25	3.60	4-6	5
DHPZ-2TRZ	−	6	0.1	6.6	5.7	0.9	0.43	0.27	0.5-0.7	1

Subscripts PF and DF denote prompt and delayed components, respectively. τ, Φ, and η are PL lifetime, PL quantum efficiency, and theoretical maximum EL quantum efficiency, respectively. $\Phi_{PL}=\Phi_{PF}+\Phi_{DF}$; $\eta_{ext}=\eta_{PF}+\eta_{DF}$. η_{out} is assumed to be 0.2−0.3.

6. 4 Electroluminescence Performance

OLEDs containing DHPZ-2BI, DHPZ-2BN, DHPZ-2BTZ, and DHPZ-2TRZ as an emitter showed green to orange emission. OLEDs were fabricated with the following device structure: indium tin oxide (ITO)/4,4′-bis[*N*-(1-naphthyl)-*N*-phenyl]biphenyl diamine (α-NPD) (35 nm)/6 wt% emitter:*m*-CBP (15 nm)/TPBi (65 nm)/LiF (0.8 nm)/Al (100 nm), where α-NPD (4,4'-bis-[*N*-(1-naphthyl)-*N*-phenylamino]-1,1'-biphenyl) and TPBi (1,3,5-tris(*N*-phenylbenzimidazol-

2-yl)benzene) were used as a hole-transporting layer and electron-transporting layer, respectively. The DHPZ-2BI- and DHPZ-2BN-based OLEDs showed green emission with EL peak maxima at 542 and 546 nm, respectively, while the DHPZ-2BTZ- and DHPZ-2TRZ-based ones exhibited yellow and orange emission with peak maxima at 601 and 617 nm, respectively (Figure 6-8a). The respective Commission Internationale de l'Éclairage (CIE) color coordinates of the DHPZ-2BI, DHPZ-2BN, DHPZ-2BTZ and DHPZ-2TRZ-based devices were (0.40, 0.55), (0.41, 0.55), (0.55, 0.45), and (0.58, 0.39) at 10 mA cm^{-2}, respectively (Figure 6-8b).

Figure 6-8c and 6-8d depict the current density–voltage–luminance (J–V–L) and η_{ext} vs. J characteristics of the DHPZ-2BI-, DHPZ-2BN-, DHPZ-2BTZ-, and DHPZ-2TRZ-based OLEDs. The maximum η_{ext} of the DHPZ-2BI-, DHPZ-2BN-, DHPZ-2BTZ-, and DHPZ-2TRZ-based devices were 12%, 6%, 5%, and 1%, respectively. The η_{ext} of DHPZ-2BI-based device is much higher than those of conventional fluorescent OLEDs.
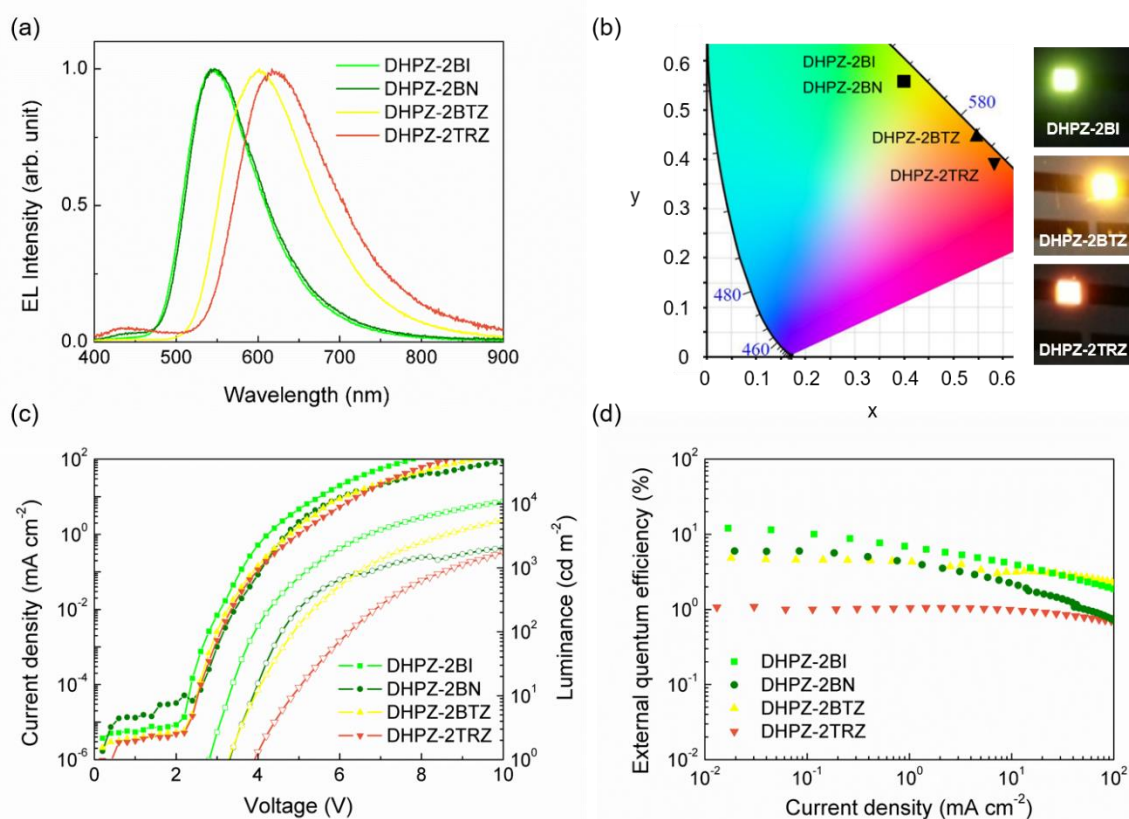
Figure 6-8. (a) EL spectra measured at 10 mA cm^{-2}. (b) EL color coordinates on the Commission Internationale de l'Éclairage (CIE) 1931 chromaticity diagram and photographs displaying EL emissions from the green, yellow and orange TADF-OLEDs. (c) Current-density–voltage–luminance (J–V–L) characteristics. (d) external-quantum-efficiency–current density (η_{ext}–J) characteristics for the DHPZ-2BI, DHPZ-2BN, DHPZ-2BTZ and DHPZ-2TRZ-based TADF OLEDs.

TADF makes a substantial contribution to the EL efficiency of the OLEDs. The theoretical maximum η_{ext} was calculated using the following equation:

$$\eta_{ext} = \left[0.25\Phi_{PF} + \{0.75 + 0.25(1 - \Phi_{PF})\} \frac{\Phi_{DF}}{1 - \Phi_{PF}} \right] \gamma\eta_{out} \tag{6-1}$$

where γ is the charge recombination factor and η_{out} is the out-coupling constant.[16] Assuming that $\gamma\eta_{out}$ is 0.2–0.3, for the DHPZ-2BI-, DHPZ-2BN-, and DHPZ-2BTZ-based OLEDs, the experimental η_{ext} values are within the range predicted by Eq. (1). Prompt and delayed components of η_{ext} are defined as:

$$\eta_{PF} = 0.25\Phi_{PF}\gamma\eta_{out} \tag{6-2}$$

$$\eta_{DF} = \{0.75 + 0.25(1 - \Phi_{PF})\} \frac{\Phi_{DF}}{1 - \Phi_{PF}} \gamma\eta_{out} \tag{6-3}$$

For a conventional fluorescent molecule with $\Phi_{DF}=0$, η_{ext} is equal to η_{PF} because η_{DF} is zero. For the DHPZ-2BI-, DHPZ-2BN-, and DHPZ-2BTZ-based OLEDs, η_{DF} is larger than η_{PF}, indicating that TADF contributes considerably to η_{ext}. η_{DF} is especially large for the DHPZ-2BI-based device: it is higher than 10%, suggesting that the contribution from TADF alone exceeds the η_{ext} of fluorescent OLEDs. For the DHPZ-2BN- and DHPZ-2BTZ-based OLEDs, although Φ_{PL} is small, because η_{DF} is large, η_{ext} is comparable to those obtained with conventional fluorescent emitters with $\Phi_{PL}\approx100\%$. For the DHPZ-2TRZ-based OLED, because $T_1 \rightarrow S_0$ nonradiative decay is large and η_{DF} is small, η_{ext} is less than 1%. However, η_{DF} still makes a non-negligible contribution to η_{ext}.

6. 5 Conclusion

TADF compounds containing a dihydrophenazine donor and various acceptors have been developed. By changing the acceptor, the emission color from green to orange, singlet-triplet energy gap, and lifetime of TADF from the compounds were controlled. An OLED using DHPZ-2BI as a green dopant exhibited a maximum η_{ext} of 12%, which is higher than those obtained with conventional fluorescent emitters.

6. 6 Experimental Section

6. 6. 1 Materials and Synthesis

Commercially available reagents and solvents were used without further purification unless otherwise noted. All of the reactions were performed under a nitrogen atmosphere in dry solvents using standard Schlenk techniques. NMR spectra were recorded on an Avance III 500 or III 400 spectrometer (Bruker). Chemical shifts of ^{1}H and signals were determined relative to the signals of tetramethylsilane ($\delta = 0.00$), CDCl$_3$ ($\delta = 77.0$) as internal standards. Matrix-assisted laser desorption ionization time-of-flight (MALDI-TOF) mass spectra were collected on an Autoflex III spectrometer (Bruker Daltonics) using dithranol as a matrix. Elemental analysis was carried out with a MT-5 CHN Corder (Yanaco).

Scheme 6-1. Synthetic routes for 5,10-dihydrophenazine, DHPZ-2BI, DHPZ-2BN, DHPZ-2BTZ and DHPZ-2TRZ.

Sythesis of 5,10-dihydrophenazine[18]: To a mixture of phenazine (5.00 g, 27.7 mmol) in ethanol (126 mL) was added, with stirring, a solution of sodium dithionate (48.2 g, 277 mmol) in water (504 mL). The mixture was stirred and heated under reflux for 3 h. A white precipitate was collected and washed with water. The collected solids were dried under reduced pressure to afford 5,10-dihydrophenazine (5.02 g, 27.5 mmol). This material was used in the next step without further purification. MS (MALDI-TOF): m/z [M+H]$^+$ calcd 182; found, 182.

Synthesis of DHPZ-2BI: To a mixture of 2-(4-bromophenyl)-1-phenyl-1H-benzimidazole (4.22 g, 12.1 mmol) that was synthesized by a reported method,[19] dihydrophenazine (1.00 g, 5.49 mmol) and potassium carbonate (4.55 g, 32.9 mmol) in toluene (20 mL) was added, with stirring, a solution of palladium(II) acetate (74.1 mg, 0.33 mmol) and tri-*tert*-butylphosphine (244.8 mg, 1.21 mmol) in toluene (20 mL). The mixture was stirred and heated under reflux for 1 day. The cooled mixture was filtered and washed with toluene, ethanol, water, and ethanol sequentially. The resulting yellow solid was dried under reduced pressure to afford DHPZ-2BI (3.83 g, 5.33 mmol). The yield was over 97.0%. The compound was further purified by sublimation under reduced pressure for OLED fabrication. ^{1}H NMR (400 MHz, CDCl$_3$): δ 7.28 (d, 8H), 7.36 (m, 10H), 7.39 (d, 4H), 7.52 (m, 8H), 7.89 (d, 4H). MS (MALDI-TOF): m/z [M+H]$^+$ calcd 719; found, 719. Anal. Calcd (%) for C$_{50}$H$_{34}$N$_6$: C, 83.54; H, 4.77; N, 11.69; found: C, 83.62; H, 4.72; N, 11.68. Thermal properties: T$_c$: 197 °C; T$_m$: 336 °C; T$_d$: 484 °C (temperature at 5% weight loss from TGA).

Synthesis of DHPZ-2BN: To a mixture of 4-bromobenzonitrile (2.20 g, 12.1 mmol), dihydrophenazine (1.00 g, 5.49 mmol) and potassium carbonate (4.55 g, 32.9 mmol) in toluene (20 mL) was added, with stirring, a solution of palladium(II) acetate (74.1 mg, 0.33 mmol) and tri-*tert*-butylphosphine (244.8 mg, 1.21 mmol) in toluene (20 mL). The mixture was stirred and heated under reflux for 1 day. The cooled mixture was partitioned between chloroform and water. The organic layer was separated, and the aqueous layer was extracted with large amounts of chloroform. The combined organic layers were washed with brine, dried over MgSO$_4$, and concentrated *in vacuo*. Hexane (20 mL) was added and an orange insoluble solid was separated by filtration. Then, the collected solid was washed with a mixture of hexane and chloroform (2:1) and dried under reduced pressure to give DHPZ-2BN (1.98 g, 5.16 mmol). The yield was over 94%. DHPZ-2BN was further purified by sublimation under reduced pressure for OLED fabrication. ^{1}H NMR (500 MHz, CDCl$_3$): δ 5.91 (m, 4H), 6.52 (m, 4H), 7.50 (d, 4H, J = 8.3

Hz), 7.88 (d, 4H, J = 8.3 Hz). MS (MALDI-TOF): m/z [M+H]$^+$ calcd 384; found, 384. Anal. Calcd (%) for $C_{26}H_{16}N_4$: C, 81.23; H, 4.20; N, 14.57; found: C, 81.27; H, 4.11; N, 14.49. Thermal properties: T_d: 351 °C (temperature at 5% weight loss from TGA).

Synthesis of DHPZ-2BTZ: To a mixture of 2-(4-bromophenyl)benzothiazole (3.51 g, 12.1 mmol), dihydrophenazine (1.00 g, 5.49 mmol) and potassium carbonate (4.55 g, 32.9 mmol) in toluene (20 mL) was added, with stirring, a solution of palladium(II) acetate (74.1 mg, 0.33 mmol) and tri-*tert*-butylphosphine (244.8 mg, 1.21 mmol) in toluene (20 mL). The mixture was stirred and heated under reflux for 1 day. The cooled mixture was filtered and washed with toluene, ethanol, water, and ethanol sequentially. The resulting reddish orange solid was dried under reduced pressure to afford DHPZ-2BTZ (2.77 g, 4.61 mmol). The yield was over 84%. DHPZ-2BTZ was further purified by sublimation under reduced pressure for OLED fabrication. ^{1}H NMR (400 MHz, CDCl$_3$): δ 5.78 (m, 4H), 6.34 (m, 4H), 7.44 (t, 2H), 7.54 (t, 2H), 7.55 (d, 4H), 7.95 (d, 2H), 8.11 (d, 2H), 8.35 (d, 4H). MS (MALDI-TOF): m/z [M+H]$^+$ calcd 601; found, 600. Anal. Calcd (%) for $C_{38}H_{24}N_4S_2$: C, 75.97; H, 4.03; N, 9.33; found: C, 75.91; H, 4.10; N, 9.28. Thermal properties: T_c: 335 °C; T_m: 387 °C; T_d: 461 °C (temperature at 5% weight loss from TGA)

Synthesis of DHPZ-2TRZ: To a mixture of 2-(4-bromophenyl)-4,6-diphenyl-1,3,5-triazine (4.69 g, 12.1 mmol) that was synthesized by a reported method,[20] dihydrophenazine (1.00 g, 5.49 mmol) and potassium carbonate (4.55 g, 32.9 mmol) in toluene (20 mL) was added, with stirring, a solution of palladium(II) acetate (74.1 mg, 0.33 mmol) and tri-*tert*-butylphosphine (244.8 mg, 1.21 mmol) in toluene (20 mL). The mixture was stirred and heated under reflux for 1 day. The cooled mixture was partitioned between chloroform and water. The organic layer was separated, and the aqueous layer was extracted with large amounts of chloroform. The combined organic layers were washed with brine, dried over MgSO$_4$, and concentrated *in vacuo*. Hexane (20 mL) was added and the resulting red insoluble solid was separated by filtration. Then, the collected solid was washed with a mixture of hexane and chloroform (2:1) and dried under reduced pressure to afford DHPZ-2TRZ (3.72 g, 4.67 mmol). The yield was over 85%. DHPZ-2TRZ was further purified by sublimation under reduced pressure for OLED fabrication. ^{1}H NMR (500 MHz, CDCl$_3$): δ 7.64 (m, 22H), 8.82 (m, 14H). MS (MALDI-TOF): m/z [M+H]$^+$ calcd 797; found, 797. Anal. Calcd (%) for $C_{54}H_{36}N_8$: C, 81.39; H, 4.55; N, 14.06; found: C,

81.53; H, 4.49; N, 14.05. Thermal properties: T_d: 496 °C (temperature at 5% weight loss from TGA).

6. 6. 2 Quantum Chemical Calculations

All quantum chemical calculations were performed using the Gaussian 09 program package.[21] S_0 geometries were optimized at the CAM-B3LYP/cc-pVDZ level of theory.[22] S_1 and NTOs were calculated with a time-dependent density functional theory (TD-DFT) method[23] using the optimized S_0 geometries (denoted as TD-CAM-B3LYP/cc-pVDZ//CAM-B3LYP/cc-pVDZ). Solvent effects were taken into account within the polarizable continuum model.

6. 6. 3 Photophysical Measurement

UV–vis absorption and PL spectra were measured with a UV-2550 spectrometer (Shimadzu) and a Fluoromax-4 spectrophotometer (Horiba Scientific), respectively, using spectral grade solvents. The PL quantum efficiencies were measured using an integration sphere system C9920-02 coupled with a PMA-11 photonic multichannel analyser (Hamamatsu Photonics) by photoexcitation (DHPZ-2BI = 430 nm, DHPZ-2BN = 420 nm, DHPZ-2BTZ = 450 nm, and DHPZ-2TRZ = 480 nm). The temperature dependence of transient PL decays was measured using a C4334 Streak camera (Hamamatsu Photonics) with a N_2 gas laser (λ = 337 nm, pulse width = 500 ps and repetition rate = 20 Hz) under vacuum ($<4 \times 10^{-1}$ Pa). Room-temperature transient PL decay measurements were carried out using a C11367 Quantaurus-tau fluorescence lifetime spectrometer (Hamamatsu Photonics).

6. 6. 4 OLED Fabrication and Characterization

ITO-coated glass substrates were cleaned with detergent, deionized water, acetone, and isopropanol. The substrates were then subjected to UV–ozone treatment for 15 min before they were loaded into a vacuum evaporation system. The organic layers were thermally evaporated on the substrates under vacuum ($<3 \times 10^{-4}$ Pa) at an evaporation rate of <0.3 nm s^{-1}. LiF and Al layers were then deposited through a shadow mask. The layer thickness and the deposition rate were monitored *in situ* during deposition by an oscillating quartz thickness monitor. The current density–voltage–luminance characteristics of the devices were measured using a source meter (Keithley 2400, Keithley Instruments Inc.) and an absolute external quantum efficiency measurement system (C9920-12, Hamamatsu Photonics). The OLEDs were mounted to the

entrance port of the measurement system's integrating sphere to collect the photons emitted from the front face of the devices. EL spectra were collected by an optical fiber connected to a spectrometer (PMA-12, Hamamatsu Photonics).

References

[1]   K. Sato, K. Shizu, K. Yoshimura, A. Kawada, H. Miyazaki, C. Adachi, *Phys. Rev. Lett.* **2013**, *110*, 247401.

[2]   H. Tanaka, K. Shizu, H. Miyazaki, C. Adachi, *Chem. Commun.* **2012**, *48*, 11392.

[3]   H. Tanaka, K. Shizu, H. Nakanotani, C. Adachi, *Chem. Mater.* **2013**, *25*, 3766.

[4]   K. Masui, H. Nakanotani, C. Adachi, *Org. Electron.* **2013**, *14*, 2721.

[5]   M. A. Baldo, C. Adachi, S. R. Forrest, *Phys. Rev. B* **2000**, *62*, 10967.

[6]   J. Lee, K. Shizu, H. Tanaka, H. Nomura, T. Yasuda, C. Adachi, *J. Mater. Chem. C* **2013**, *1*, 4599.

[7]   a) Z. Gao, C. S. Lee, I. Bello, S. T. Lee, R.-M. Chen, T.-Y. Luh, J. Shi, C. W. Tang, *Appl. Phys. Lett.* **1999**, *74*, 865; b) M.-Y. Lai, C.-H. Chen, W.-S. Huang, J. T. Lin, T.-H. Ke, L.-Y. Chen, M.-H. Tsai, C.-C. Wu, *Angew. Chem. Int. Ed.* **2008**, *47*, 581; c) C.-H. Chen, W.-S. Huang, M.-Y. Lai, W.-C. Tsao, J. T. Lin, Y.-H. Wu, T.-H. Ke, L.-Y. Chen, C.-C. Wu, *Adv. Func. Mater.* **2009**, *19*, 2661.

[8]   Z. R. Grabowski, K. Rotkiewicz, W. Rettig, *Chem. Rev.* **2003**, *103*, 3899.

[9]   a) C. H. Chen, C. W. Tang, *Appl. Phys. Lett.* **2001**, *79*, 3711; b) K. Okumoto, H. Kanno, Y. Hamaa, H. Takahashi, K. Shibata, *Appl. Phys. Lett.* **2006**, *89*, 063504; c) K. Okumoto, H. Kanno, Y. Hamada, H. Takahashi, K. Shibata, *Appl. Phys. Lett.* **2006**, *89*, 013502.

[10]   H. Inomata, K. Goushi, T. Masuko, T. Konno, T. Imai, H. Sasabe, J. J. Brown, C. Adachi, *Chem. Mater.* **2004**, *16*, 1285.

[11]   H.-F. Chen, S.-J. Yang, Z.-H. Tsai, W.-Y. Hung, T.-C. Wang, K.-T. Wong, *J. Mater. Chem.* **2009**, *19*, 8112.

[12]   A. Endo, K. Sato, K. Yoshimura, T. Kai, A. Kawada, H. Miyazaki, C. Adachi, *Appl. Phys. Lett.* **2011**, *98*, 083302.

[13]   S. Y. Lee, T. Yasuda, H. Nomura, C. Adachi, *Appl. Phys. Lett.* **2012**, *101*, 093306.

[14]   R. Martin, *J. Chem. Phys.* **2003**, *118*, 4775.

[15]   a) J. Tomasi, B. Mennucci, R. Cammi, *Chem. Rev.* **2005**, *105*, 2999; b) R. Improta, V. Barone, G. Scalmani, M. J. Frisch, *J. Chem. Phys.* **2006**, *125*, 054103; c) R.Improta, G. Scalmani, M. J. Frisch, V. Barone, *J. Chem. Phys.* **2007**, *127*, 074504.

[16]   J. V. Morris, U. Brühlmann, O. Serafimov, J. R. Huber, *Ber. Buns. Gesell.* **1974**, *78*, 1348.

[17]   S. Gong, X. He, Y. Chen, Z. Jiang, C. Zhong, D. Ma, J. Qin, C. Yang, *J. Mater. Chem.* **2012**, *22*, 2894.

[18]   X.-Q. Zhu, Z. Dai, A. Yu, S. Wu, J.-P. Cheng, *J. Phys. Chem. B.* **2008**, *112*, 11694.

[19]   M. Debeaux, M. W. Thesen, D. Schneidenbach, H. Hopf, S. Janietz, H. Krüger, A. Wedel, W. Kowalsky, H.-H. Johannes, *Adv. Funct. Mater.* **2010**, *20*, 399.

[20]   H. Tanaka, K. Shizu, H. Miyazaki, C. Adachi, *Chem. Commun.* **2012**, *48*, 11392.

[21]   M. J. Frisch, G. W. Trucks, H. B. Schlegel, G. E. Scuseria, M. A. Robb, J. R. Cheeseman, G. Scalmani, V. Barone, B. Mennucci, G. A. Petersson, H. Nakatsuji, M. Caricato, X. Li, H. P. Hratchian, A. F. Izmaylov, J. Bloino, G. Zheng, J. L.Sonnenberg, M. Hada, M. Ehara, K. Toyota, R. Fukuda, J. Hasegawa, M. Ishida, T. Nakajima, Y. Honda, O. Kitao, H. Nakai, T. Vreven, J. A. Montgomery, J. E. Peralta, F. Ogliaro, M. Bearpark, J. J. Heyd, E. Brothers, K. N. Kudin, V. N. Staroverov, R. Kobayashi, J. Normand, K. Raghavachari, A. Rendell, J. C. Burant, S. S. Iyengar, J. Tomasi, M. Cossi, N. Rega, J. M. Millam, M. Klene, J. E. Knox, J. B. Cross, V. Bakken, C. Adamo, J. Jaramillo, R. Gomperts, R. E. Stratmann, O. Yazyev, A. J. Austin, R. Cammi, C. Pomelli, J. W. Ochterski, R. L. Martin, K. Morokuma, V. G. Zakrzewski, G. A. Voth, P. Salvador, J. J. Dannenberg, S. Dapprich, A. D. Daniels, Ö. Farkas, J. B. Foresman, J. V. Ortiz, J. Cioslowski, D. J. Fox, *GAUSSIAN 09, Revision C.01*, Gaussian, Inc., Wallingford, CT, **2009**.

[22]   a) T. Yanai, D. P. Tew, N. C. Handy, Chem. Phys. Lett. 2004, 393, 51; b) J. T. H. Dunning, *J. Chem. Phys.* **1989**, *90*, 1007.

[23]   a) R. Bauernschmitt, R. Ahlrichs, *Chem. Phys. Lett.* **1996**, *256*, 454; b) M. E. Casida, C. Jamorski, K. C. Casida, D. R. Salahub, *J. Chem. Phys.* **1998**, *108*, 4439.

Chapter 7

Summary and Perspective

In this dissertation, molecular design, synthesis, and properties of highly efficient thermally activated delayed fluorescence (TADF) materials were studied for organic light-emitting diodes (OLEDs) application.

In chapter 2, a new series of donor–acceptor (D–A) molecules consisting of a xanthone acceptor unit coupled with different donor units was designed and synthesized. OLEDs employing a heavily doped emitting layer consisting of 75 wt%-TADF emitter doped in a host material exhibited considerably high external EL quantum efficiencies of up to 18% with suppressed concentration quenching characteristics. Concentration quenching of TADF molecules was found to be dominated by electron-exchange interactions for triplet excitons, as described by the Dexter energy-transfer model. This result is in marked contrast to conventional fluorescent and phosphorescent molecules, which involve the Förster energy-transfer mechanism. Owing to the short-range nature of electron-exchange interactions, even a small modulation in molecular geometric structures drastically affected the concentration-quenching behavior, leading to enhanced photoluminescence (PL) and EL properties.

In chapter 3, regioisomeric D–A molecules consisting of a xanthone acceptor unit and a para- or meta-linked tercarbazole donor unit were designed and synthesized as TADF emitters. These luminophores exhibited obvious twisted intramolecular charge transfer characteristics, as revealed by solvatochromism and transient PL analyses. Blue OLEDs employing these TADF emitters showed high external EL quantum efficiencies of up to 14.4% with suppressed roll-off characteristics.

In chapter 4, new D–A molecules comprised of isobenzofuranone or chromone as an acceptor unit and spiroacridan as a donor unit, were designed and synthesized as blue TADF emitters. Their small ΔE_{ST} values in the range of 0.08–0.11 eV could contribute to the fast RISC, leading to short triplet exciton lifetimes of less than 4 μs. The OLEDs based on these TADF emitters exhibited high external EL quantum efficiencies of up to 16.2% with extremely suppressed efficiency roll-off characteristics even in their heavily doped and non-doped devices. From the detailed analysis of efficiency roll-off characteristics, the fast RISC for isobenzofuranone and chromone-based TADF emitters significantly suppressed singlet–triplet annihilation and triplet–triplet annihilation processes.

In chapter 5, donor–acceptor–donor (D–A–D) and D–A molecular systems containing oxadiazole or triazole as an acceptor unit and phenoxazine as a donor unit were developed. In toluene solution, the D–A–D molecules showed more efficient TADF and higher PL quantum

efficiencies than D–A molecules. OLEDs utilizing D–A–D molecules displayed green and blue EL emission with external EL quantum efficiency of 14.9% and 6.4%, respectively.

In chapter 6, a series of acceptor–donor–acceptor molecules, comprising a dihydrophenazine donor unit coupled with various acceptor units was designed and synthesized. The emission color from green to orange, ΔE_{ST} values (~0–0.19 eV), and triplet exciton lifetimes (0.14–0.53 μs) of these TADF materials could be controlled by changing the acceptor units. A green-emitting OLED based on the benzimidazole-based TADF emitter exhibited a external EL quantum efficiency of 12%, which is much higher than the theoritical limit of external EL quantum efficiencies in conventional fluorescent OLEDs.

At the beginning of the development of oxadizaole- and triazole-based TADF materials for efficient blue and green OLEDs, controlled emission color and singlet–triplet energy gaps of TADF emitters and regioiomeric effect on TADF properties have been studied for realizing highly efficient TADF. Moreover, molecular design strategies have been successfully applied to TADF materials for improving the device performance: for example, by inhibiting concentration quanching and reducing efficiency roll-off characteristics.

Three primary color (red, green, and blue) emitters are required for full-color displays and solid-state lighting. Promising red and green phosphorescent organometallic iridium complexes have been reported with high quantum efficiency, high color purity, and long-term stability, whereas devices containing blue phosphorescent emitters exhibited lower operational stability than their counterparts owing to the limit to molecular design of pure blue emitters. Furthermore, the use of expensive rare metal elements is indispensable to improve the exciton generation in phosphorescent OLEDs. To realize cost-effective and high-performance devices, pure-organic TADF luminophores are essential prerequisites for next-generation OLEDs.

Owing to their long-lasting excited states, TADF molecules generally have a strong tendency to undergo concentration quenching in condensed states or solid thin films, which causes significat energy loss through nonradiative decativation processes. To circumvent this fundamental problem, host–guest systems have been adopted for the fabrication of TADF-OLEDs by dispersing the emissive TADF molecules as a guest in a wide bandgap solid host matrix. However, this approach requires complex manufacturing techniques and involes a high cost associated with precise co-evaporation processes.

So far, although blue TADF materials have been developed to achieve efficient blue EL with high quantum efficiencies, their color purity and efficiency roll-off are main abstacles in devices. TADF-based OLEDs suffer from the the exciton annihilation processes (efficiency roll-off)

such as triplet–triplet and singlet–triplet annihilations (TTA and STA) at high current density which are caused by their relatively long excited state lifetimes. Blue-emitting materials with Commission Internationale de l'Eclairage (CIE) color coordinates (0.10, < 0.10) are a prerequisite for OLED commercialization. To offer pure blue emission, blue TADF materials are expected to require a S_1 energy level higher than 2.9 eV. Additionally, wide full width at half maximum (FWHM) resulting from intramolecular charge trasnfer transition between the donor and acceptor of a TADF emitter should be decreased for realizing high-quality blue EL.

By the combination of suitable donor and acceptor groups, a novel pure blue TADF molecule possessing minimal concentration quenching, short TADF lifetime, and sharp FWHM should induce high-performance TADF-OLEDs with high EL efficiencies, reduced efficiency roll-off characteristics, and high color purity. Herein, the author proposed a novel approach for high-performance pure blue TADF materials. TADF molecules in both chapters 2 and 4 exhibited low concentration quenching behavior as well as remarkably short emission lifetimes. As a result, OLEDs utilizing these materials achieved the high maximum external EL quantum efficiencies, which retained high values even at high current density. The devices using these materials containing the acridan donor unit at low doping concentration (< 10 wt%) tend to exhibit relatively low external EL quantum efficiencies because of its poor hole transporting properties, whereas the devices utilizing the materials in chapter 3 achieved high external EL quantum efficiencies even at low doping concentration owing to good hole transporting properties of carbazole groups. From these aspects, a new molecule was designed, comprising an isobenzofuranone with spiro-structured fluorene as an acceptor unit coupled with a tercarbazole containing methyl groups on *peri*-position as a donor unit (Figure 7-1). This newly designed molecule expected to exhibit the following properties: i) pure blue and sharped emission owing to weak donor and acceptor units and a rigid structure by *peri*-position methyl groups, respectively, ii) good hole transporting properties due to carbazole groups, iii) low concentration quenching behavior because spiro-fused fluorene could leads to suppress the intermolecular electron-exchange interaction, and iv) reduced efficiency roll-off characteristics in its OLED owing to its short emission lifetime.
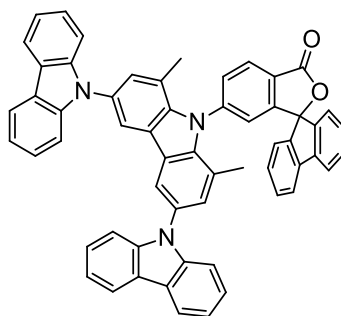
Figure 7-1. A structure of a candidate molecule for efficient pure blue TADF.

List of Publications

♦ Original Papers

[1] Versatile Molecular Functionalization for Inhibiting Concentration Quenching of Thermally Activated Delayed Fluorescence
<u>Jiyoung Lee</u>, Naoya Aizawa, Masaki Numata, Chihaya Adachi, and Takuma Yasuda, *Advanced Materials* **2017**, *29*, 1604856.

[2] Thermally Activated Delayed Fluorescence Properties of Regioisomeric Xanthone-Based Twisted Intramolecular Charge-Transfer Luminophores
<u>Jiyoung Lee</u>, In Seob Park, and Takuma Yasuda, *Bulletin of the Chemical Society of Japan* **2017**, *90*, 231–236.

[3] Isobenzofuranone- and Chromone-Based Thermally Activated Delayed Fluorescence Materials for Reduced Efficiency Roll-Off in Blue Organic Light-Emitting Diodes
<u>Jiyoung Lee</u>, Naoya Aizawa, Yu Seok Yang, In Seob Park, and Takuma Yasuda, in preparation.

[4] Oxadiazole- and Triazole-Based Highly-Efficient Thermally Activated Delayed Fluorescence Emitters for Organic Light-Emitting Diodes
<u>Jiyoung Lee</u>, Katsuyuki Shizu, Hiroyuki Tanaka, Hiroko Nomura, Takuma Yasuda, and Chihaya Adachi, *Journal of Materials Chemistry C* **2013**, *1*, 4599–4604.

[5] Controlled Emission Colors and Singlet–Triplet Energy Gaps of Dihydrophenazine-Based Thermally Activated Delayed Fluorescence Emitters
<u>Jiyoung Lee</u>, Katsuyuki Shizu, Hiroyuki Tanaka, Hajime Nakanotani, Takuma Yasuda, Hironori Kaji, and Chihaya Adachi, *Journal of Materials Chemistry C* **2015**, *3*, 2175–2181.

♦ Joint Papers

[1] High-Performance Blue Organic Light-Emitting Diodes with 20% External Quantum Efficiency Based on Pyrimidine-Containing Thermally Activated Delayed Fluorescence Emitters
In Seob Park, <u>Jiyoung Lee</u>, and Takuma Yasuda, *Journal of Materials Chemistry C* **2016**, *4*, 7911–7916.

[2]   Aggregation-Induced Delayed Fluorescence Based on Donor/Acceptor-Tethered Janus Carborane Triads: Unique Photophysical Properties for Non-Doped OLEDs
Ryuhei Furue, Takuro Nishimoto, In Seob Park, <u>Jiyoung Lee</u>, and Takuma Yasuda, *Angewandte Chemie International Edition* **2016**, *55*, 7171–7175.

[3]   Thermally Activated Delayed Fluorescence Polymers for Efficient Solution Processed Organic Light-Emitting Diodes
Sae Youn Lee, Takuma Yasuda, Hideaki Komiyama, <u>Jiyoung Lee</u>, and Chihaya Adachi, *Advanced Materials* **2016**, *28*, 4626–4631.

[4]   Organic Light-Emitting Diodes Based on Donor-Substituted Phthalimide and Maleimide Fluorophores
Myung Eun Jang, Takuma Yasuda, <u>Jiyoung Lee</u>, Sae Youn Lee, and Chihaya Adachi, *Chemistry Letters* **2015**, *44*, 1248–1250.

[5]   Highly Efficient Electroluminescence from Purely Organic Donor–Acceptor Systems
Katsuyuki Shizu, <u>Jiyoung Lee</u>, Hiroyuki Tanaka, Hiroko Nomura, Takuma Yasuda, Hironori Kaji, and Chihaya Adachi, *Pure and Applied Chemistry* **2015**, *87*, 627–638.

[6]   Effect of Atom Substitution in Chalcogenodiazole-Containing Thermally Activated Delayed Fluorescence Emitters on Radiationless Transition
Hiroyuki Tanaka, Katsuyuki Shizu, <u>Jiyoung Lee</u>, and Chihaya Adachi, *Journal of Physical Chemistry C* **2015**, *119*, 2948–2955.

List of Symposium

♦ **International Conferences**

[1]　High-Efficiency Blue Thermally Activated Delayed Fluorescence Materials and Devices with Suppressed Concentration Quenching Characteristics
Jiyoung Lee, Naoya Aizawa, Masaki Numata, Chihaya Adachi, and Takuma Yasuda, *International Union of Materials Research Societies-International Conference on Electronic Materials (IUMRS-ICEM2016)*, Suntec, Singapore (July 04–08, 2016), Oral presentation.

[2]　Development of Efficient Blue Thermally Activated Delayed Fluorescence Emitters and Clarification of Concentration Quenching Mechanism
Jiyoung Lee, Masaki Numata, Woong Shin, Yu Seok Yang, Takuma Yasuda, and Chihaya Adachi, *The International Chemical Congress of Pacific Basin Societies 2015*, Honolulu, Hawaii, USA (December 15–20, 2015), Poster presentation.

[3]　Development of Thermally Activated Delayed Fluorescence Emitters and Clarification of Concentration Quenching Mechanism
Jiyoung Lee, Takuma Yasuda, Masaki Numata, Woong Shin, Yu Seok Yang, and Chihaya Adachi, *16th International Symposium on Novel Aromatic Compounds (ISNA16)*, Madrid, Spain (July 5–10, 2015), Poster presentation.

[4]　Emission Color Tuning and Controlling Singlet–Triplet Energy Gap of Dihydrophenazine-Based Thermally Activated Delayed Fluorescence emitters
Jiyoung Lee, Katsuyuki Shizu, Hiroyuki Tanaka, Hajime Nakanotani, Takuma Yasuda, Hironori Kaji, and Chihaya Adachi, *6th Asian Conference on Organics Electronics (A-COE)*, Tainan, Taiwan (November 12–14, 2014), Poster presentation.

[5]　Oxadiazole- and Triazole-Based Highly-Efficient Thermally Activated Delayed Fluorescence Emitters for Organic Light-Emitting Diodes
Jiyoung Lee, Katsuyuki Shizu, Hiroyuki Tanaka, Hiroko Nomura, Takuma Yasuda, and Chihaya Adachi, *SPIE Photonics Europe 2014*, Brussels, Belgium, (April 14–17, 2014), Poster presentation.

[6] Highly-Efficient Donor-Acceptor-Donor Structured Thermally-Activated Delayed-Fluorescence (TADF) Emitters for Organic Light-Emitting Diodes

Jiyoung Lee, Katsuyuki Shizu, Hiroyuki Tanaka, Hiroko Nomura, Takuma Yasuda, and Chihaya Adachi, *The 21th Joint Seminar of the Kyushu Branch of the Chemical Society of Japan and the Pusan Branch of the Korean Chemical Society*, Busan, Korea, (June 13, 2013), Poster presentation.

♦ **Domestic Conferences**

[1] ジヒドロフェナジン骨格を有する TADF 材料の開発：発光波長ならびに一重項−三重項エネルギーギャプの制御

Jiyoung Lee, Katsuyuki Shizu, Hiroyuki Tanaka, Hajime Nakanotani, Takuma Yasuda, and Chihaya Adachi, 日本化学会第 94 春季年会, 名古屋, （2014 年 3 月 27–30 日）, Oral presentation.

[2] Oxadiazole- and Triazole-Based Highly-Efficient Thermally-Activated Delayed-Fluorescence (TADF) Emitters for Organic Light-Emitting Diodes

Jiyoung Lee, Katsuyuki Shizu, Hiroyuki Tanaka, Hiroko Nomura, Takuma Yasuda, and Chihaya Adachi, 第 60 回応用物理学会春季学術講演会, 神奈川, （2013 年 3 月 27–30 日）, Poster presentation.

Acknowledgments

First and foremost, I would like to dedicate my gratitude to Prof. Takuma Yasuda at Kyushu University for helpful advice to progress advanced research and a lot of opportunity to have invaluable experience during the doctoral course.

It is my great pleasure to thank Prof. Tatsumi Ishihara and Prof. Keiji Tanaka for helful advice and discussions regarding this dissertation as committee.

I would like to acknowledge the continuing counseling and encouragement of Prof. Chihaya Adachi during the doctoral course.

I would like to thank the Yasuda laboratory members, Keiko Urakawa, Assistant Prof. Hideaki Komiyama, Assistant Prof. Naoya Aizawa, Dr. Kyohei Matsuo, In Seob Park, Seiichi Furukawa, Ryuhei Furue, Tatsuya Ohyama, Hiroki Tachibana, Takahiro To, Kohei Isayama, Tatsuya Mori, Satoshi Uwagawa, and So Shikita, as well as alumni and past members of Yasuda laboratory, Dr. Yu Seok Yang, Dr. Woong Shin, Dr. Sae Youn Lee, Keiro Nasu, Takuro Nishimto, Keisuke Asahi, Yuta Fukutomi, Yu Hidaka, Chao-Jen Tsou, and Myung Eun Jang, who have been very helpful, collaborative, and friendly inside and outside the laboratory during the doctoral course.

I would like to appreciate Assistant Prof. Katsuyuki Shizu, Dr. Hiroyuki Tanaka, Masaki Numata, and Hiroko Nomura for helping with experiements and valuable discussion.

I also would like to thank to Assistant Prof. Sunnam Kim, Assistant Prof. Ju-Hyung Kim, and Dr. Myungkwan Song, who gave me invaluable advice.

Finally, I am deeply indebted to Prof. Bong Lee at Pukyong National University for invaluable advice and the great opportunity to study in Kyushu University, Japan, and also would like to give my deepest appreciation to my family members: my grandparents, my parents Ingab Lee and Kyoungouk Jang, my brother Jonghun Lee, and my sister-in-law Soyoung Kim. Their emotional support, love, and encouragement have inspired me to complete the doctoral course.

Jiyoung Lee   January, 2017